LBL-34889
UC-410

Laser-Material Interactions:

A Study of Laser Energy Coupling with Solids

Mark A. Shannon

Ph. D. Thesis

Department of Mechanical Engineering
University of California at Berkeley
Berkeley, CA 94720 USA
and
Energy and Environment Division
Lawrence Berkeley Laboratory
University of California
Berkeley, CA 94720 USA

November 1993

This work was supported by the Director, Office of Energy Research, Office of Basic Energy Sciences, Division of Chemical Sciences, of the U.S. Department of energy under Contract No. DE-AC03-76SF00098.

Abstract

Laser-Material Interactions:
A Study of Laser Energy Coupling with Solids

by

Mark Alan Shannon

Doctor of Philosophy in Engineering
University of California at Berkeley

Professor Boris Rubinsky, Chair

This study of laser-light interactions with solid materials ranges from low-temperature heating to explosive, plasma-forming reactions. Contained are four works concerning laser-energy coupling: laser i) heating and ii) melting monitored using a mirage effect technique, iii) the mechanical stress-power generated during high-powered laser ablation, and iv) plasma-shielding.

First, a photothermal deflection (PTD) technique is presented for monitoring heat transfer during modulated laser heating of opaque solids that have not undergone phase-change. Of main interest is the physical significance of the shape, magnitude, and phase for the temporal profile of the deflection signal. Considered are the effects that thermophysical properties, boundary conditions, and geometry of the target and optical probe-beam have on the deflection response. PTD is shown to monitor spatial and temporal changes in heat flux leaving the surface due to changes in laser energy coupling.

The PTD technique is then extended to detect phase-change at the surface of a solid target. Experimental data shows the onset of melt for indium and tin targets. The conditions for which melt can be detected by PTD is analyzed in terms of geometry, incident power and pulse length, and thermophysical properties of the target and surroundings.

Next, monitoring high-powered laser ablation of materials with stress-power is introduced. The motivation for considering stress-power is given, followed by a theoretical discussion of stress-power and how it is determined experimentally. Experiments are presented for the ablation of aluminum targets as a function of energy and intensity. The stress-power response is analyzed for its physical significance.

Lastly, the influence of plasma-shielding during high-powered pulsed laser-material interactions is considered. Crater size, emission, and stress-power are measured to determine the role that the gas medium and laser pulse length have on plasma shielding. By using all three techniques, plasma-shielding is established to occur in pico-second time periods with copper targets. Possible mechanisms are explored and the existence of fast photo-electrons is postulated to initiate shielding. A model using fast electrons agrees qualitatively with the experimental results.

Chair, dissertation committee

to my loving wife Mona

who is always there for me

and to my boys

Davis, Robert, and Neal

who give me such joy

Contents

Contents

Contents

Contents

List of Figures

Chapter 2

Chapter 3

Chapter 4

Chapter 5

List of Tables

Acknowledgments

No acknowledgments of gratitude for the mentally and physically exhausting process of birthing a thesis could begin without thanking my wife, Mona, from the bottom of my heart. The seemingly endless days and nights spent caring for our children, working to support us, and running the household is the most help that anyone could give me. I would also like to thank my boys, Davy, Robby, and Neal, for putting up with my absence. I know it has been hard on them too. Davy hasn't liked me missing his soccer games, Robby tells me "miss you Dad", and Neal squeals "Hi Daddy, Hi Daddy" non-stop when he does see me. Also, my parents and sisters have not gotten to see me much, and I have enjoyed all the support my parents have given me. I am indebted to my family.

The first time I heard of *Team Destructo*, I knew I was in for a great time. I am grateful to Dr. Richard E. Russo, informally known as Rick, for giving me a job and helping me as a graduate student researcher in his laser lab at Lawrence Berkeley Laboratory. Before joining his group four years ago, Rick ask me what I knew about lasers. I told him "nothing, squat, nada"...but I could learn, and he hired me anyway. I have enjoyed collaborating with Rick and my fellow lab mates on all the different research topics concerning lasers, of which only a few have made it into this dissertation. I am most thankful for all the help.

I would like to single out a few *Team Destructo* members and laboratory mates on campus for special thanks. Marvin M. Kilgo III has given me innumerable hours of good talk and feedback. I appreciated Marvin being there to sound out ideas and for his opinions. I would like

to thank James Rudnicki for two things. One was his help in setting up and teaching me the program *Displa* used for graphing the great 3-D figures in chapter 3. The other was his uncompromising push to keep me on tract. I would also like to thank Xianglei Mao and Wing-Tat Chan for their work and collaboration with chapter 5, and for their good conversations and insights throughout this work. I thank Ali A. Rostami for his collaboration with the numerical modeling in chapter 2. Last but not least, I appreciate all the help Russell Keanini gave me early on.

I would also like to thank the department of Mechanical Engineering at Berkeley for their initial scholarship support, and IBM for awarding me their fellowship grant to research laser-material interactions. My work at LBL was supported by the U.S. Department of Energy, Office of Basic Energy Sciences, Division of Chemical Sciences, under Contract No. DE-AC03-76SF00098.

Finally, I want to thank the person who is the most responsible for me staying at Berkeley for graduate work, who gave me the opportunity to work up at LBL, and who helped me obtain the scholarship and fellowship support...my research advisor and mentor, Professor Boris Rubinsky. I met Boris when I was an undergraduate at Berkeley. I had an idea concerning bioengineering I wanted to pursue, and I was told Professor Rubinsky was the person to talk to. The only problem was that he was very busy, and we couldn't find a time to talk. So one day I waited outside his office until he said we could talk for a few minutes. A couple of hours later, he had given me a desk in his laboratory and signed me up for undergraduate research with him. I have greatly benefited from his help and insight in our collaborations, and I am indebted to him.

Chapter 1
Laser-Material Interactions: Introduction

1.1 Topical Overview

The study of laser light interactions with solid materials began shortly after the development of the laser itself when Maiman (1960) demonstrated the first "optical maser". When high-power ruby lasers were developed shortly thereafter, focused laser beams heated, melted, vaporized, and ionized material in solid targets. A flurry of experimental and theoretical work in the 1960's laid most of the foundations for research into laser-material interactions. The classic book by Ready (1971) reviews and presents most of the developments of that decade. Applications employing the interaction between laser light and materials were to come later in the 1970's and 1980's. Typical applications include laser machining and welding, chemical separation and analysis, material structure and property evaluation, and vaporization and ablation of solids for uses ranging from thin-film deposition to microfabrication to medical surgery.

To help organize this discussion, laser-material interactions which cover the work in this thesis will be divided into three regimes using laser

intensity as the guide. The value for the intensities chosen is somewhat arbitrary, and many of the comments for one range may apply to another.

The first regime is low-intensity interactions, where the power of the laser beam per unit area is up to the order of 10^4 W/cm^2. In this regime, thermal processes dominate. Depending on the material's thermal and optical properties, the geometry and spatial profile of the laser beam, the geometry of the target and its boundary conditions, and the coherence, wavelength, and pulse length of the laser, the response of the material to laser light ranges from gentle heating to vaporization. For modulated or pulsed laser light in the upper reaches of this regime, significant interactions of the vapor plume with the incident light can occur, coupling the laser energy with the vapor in a radiatively participating medium. For low intensity continuous wave (CW) light, the laser will heat the solid volumetrically or if the optical density of the material is very high, the laser beam will behave as a surface heat source.

The next regime is mid-range interactions, where the intensity of the laser is in the range of 10^5 to 10^8 W/cm^2. The interactions in this range are difficult to characterize in broad strokes...everything from simple heating to plasma formation can occur. The hallmark of mid-range interactions is that each mode of energy transfer must be considered, and that the interaction is often threshold dependent. For example, vigorous evaporation of a material caused by powerful CW lasers may require diffusion, convection, and radiation heat transfer to adequately describe the energy balance. For short pulsed lasers, virtually no material dislocation may occur during irradiation of a dielectric

material, yet for the same conditions a plasma may form above a metallic material. The plasma forms due to emission of charged particles from the surface when the material's work function is exceeded for the conditions at the time, causing an avalanche ionization process to occur in the adjacent gas medium. The point of this example is that whether or not a medium is radiatively participating is threshold dependent, and cannot always be predicted a priori.

In the final high-range regime, the intensity exceeds 10^9 W/cm^2. Ultra high intensities over 10^{15} W/cm^2 discussed in the fusion literature are not considered here. With high intensities, there is almost always material removed from a target, often explosively, and plasma formation is common. Dissociation of molecules, ionization, and chemical reactions can become significant during the interaction. The interaction of the intense electromagnetic field of the laser light with both the target and the surrounding medium determine the response of the material, and non-linear optical effects and plasma dynamics can occur. An important consideration for energy coupling to the surface is that the plasma may shield the target from the incident laser light. Plasma shielding not only can alter the amount of laser intensity reaching the surface, but can change the way that mass and energy is transferred from the target. Another hallmark of the high intensity regime is that very high pressures due to momentum recoil and shock wave generation can occur during pulsed-laser irradiation. Significant stresses and rates of deformation can occur, leading to energy transfer through mechanical means. Therefore, at high intensities the effect of chemical, electromagnetic, and mechanical

transfer of energy must be added to thermal transport for consideration.

A tremendous amount of research on the interaction between laser light and materials has occurred since 1960, too much to even begin to cover here. Yet the explosive growth in the 1980's in the number and types of lasers available has spawned more applications, and consequently the need to better understand and measure the processes that are occurring. A common thread to many of the problems is how much laser energy is coupled to the target. Questions as to how the coupled energy changes during a laser pulse, and how those changes can be monitored are central to many diagnostic uses of lasers. Fundamental questions of changes to energy transport mechanisms are still open for certain laser processing of materials, particularly in the mid to high intensity ranges.

The original goal for this work was to develop techniques to monitor the transfer of laser energy into solid targets, and to gain a better fundamental understanding of the energy coupling mechanisms. One of my desires was to explore laser-material interactions in each of the three intensity regimes. Lucky enough to be associated with a laboratory which had both CW lasers and high-power pulsed lasers, I also had the means to do so.

Two topics of interest to me are laser-induced phase-change phenomena at a surface, and mechanical energy transfer during high-power laser ablation of solids. The first topic is in the low-intensity regime, and the second covers both the mid and high regimes. Two different monitoring techniques were developed in response to the physics of each situation. For the first topic, a non-invasive probe was needed to

determine how the heat flux leaving a surface changed upon a solid to liquid phase change. This requirement led to the use of an optical probe described below. For the second topic, a method was needed to monitor the power carried by stress waves. This requirement led to using a series of piezoelectric transducers on the target and in the atmosphere.

1.2 Scope of Dissertation

This dissertation contains four separate works, which cover two different physical phenomena and methods for monitoring them. The first phenomenon is low-temperature laser heating of solids, including phase-change at the surface. The method for monitoring the heating process employs the fact that light bends in the presence of an index of refraction gradient, often called the mirage effect. First developed in the early 1980's by Murphy and Aamodt (1980) and Boccara et al (1980) as a spectroscopy method, the mirage effect technique is extended to monitoring heat flux changes at a surface. The second phenomenon is the high-power ablation of solids. The method for monitoring the ablation process records the signal from stress transducers in time and calculates the mechanical stress power generated. This work follows from the general thermomechanical theory presented by Green and Naghdi (1991).

Chapters 2 and 3 cover the low-temperature laser heating work, and chapters 4 and 5 cover the high-power pulsed-laser ablation of material. Although each chapter is a complete work, a brief preview of what is contained in each and how the respective chapters relate to each other is given below.

- Chapter 2 presents and analyzes the use of a mirage effect

technique, called photothermal deflection, for monitoring heat transfer during modulated laser heating of solids. Of main interest is the temporal profile of the deflection signal, and the physical significance of the shape, magnitude, and phase of the signal. The scope of this work is low temperature heating of opaque solids without any phase change. It lays the ground work for the following chapter by looking at the effects that thermophysical properties, boundary conditions, geometry of the target and optical beam, and the laser beam have on the deflection response.

- Chapter 3 extends the photothermal defection work to cover the onset of melt at the surface of a target. Experimental data is presented which shows that the onset of melting can be detected using this technique. Analysis follows to explore under what conditions melt can be detected in terms of geometry, incident power and pulse length, and thermophysical properties of the target and surroundings. The chapter closes with a discussion of further work that needs to be done to extend the analysis to additional cases of phase-change not covered here.

- Chapter 4 explores the measurement of mechanical energy transport through stress as a tool for monitoring high-power laser ablation of materials. The motivation for looking at mechanical stress power is given, followed by a theoretical discussion of stress power and how it is measured and calculated in the experiments. Experimental work is presented for the ablation of aluminum targets as a function of energy and intensity ranging from 10^6 to 10^{10} W/cm^2. The stress power response is analyzed for its physical significance. This introductory work provides much of the ground work for the use of stress power in monitoring plasma shielding in chapter 5.

- Chapter 5 looks at the influence of plasma shielding during high-power pulsed laser-material interactions. What the effect that the gas medium has on the coupling of laser energy into the target is explored using three different physical measurements. Crater size, an emission spectrum, and stress power are all measured to determine the role that the gas medium and laser pulse length have on plasma shielding. By using all three techniques, plasma shielding is established to occur in pico-second time periods, which is an interesting finding. To explain this finding, the possible mechanisms are explored and the existence of fast photo-electrons is postulated to initiate the shielding. A simplified physical model is developed using fast electrons that agrees qualitatively with the experimental results. The chapter closes with a discussion on the need to verify the proposed shielding mechanism with further study.

References

A.C. Boccara, D. Fournier, W. Jackson, and N.M. Amer, (1980) Opt. Lett. **5**, p. 377.

A.E. Green and P.M. Naghdi, (1991) Proc. Royal Soc. Lond. A **432**, p. 171.

T.H. Maiman, (1960) Nature **187**, p. 493.

J.C. Murphy and L.C. Aamodt, (1980) J. Appl. Phys. **51**, p. 4580.

J.F. Ready, (1971) *Effects of High-Power Laser Radiation*, Academic Press, New York.

Chapter 2

Photothermal Deflection Measurements for Monitoring Heat Transfer During Modulated Laser-Heating of Solids

In this chapter, laser heating of solid targets is monitored in the air adjacent to the surface using a photothermal deflection (PTD) technique. The temporal profile of the PTD response is studied here for the case of linear heating without phase change as the necessary foundation for detecting transient phase-change at a surface that is considered in the next chapter. Numerical and experimental work is presented to show the effect on the shape, magnitude, and phase of a PTD signal due to changes in 1) the thermophysical properties of the target material and deflecting medium, 2) the dimensions and boundary conditions of the target, 3) the distance of the probe-beam from the surface of the target, and 4) the modulation frequency of the heating source. An unusual phenomenon was found when heating with a finite-sized heating source. When the thermal diffusivity of the target and deflecting medium are different and the probe-beam is close to the surface, a local maximum is observed in the time-response profile of the PTD signal during the heating cycle. The maximum occurs due to changing heat flux directions leaving the surface over time. The shape of the PTD signal, therefore, also provides information about the laser heating process at a surface in real time.

2.1 Introduction

The deflection of a probe laser beam by thermal and concentration gradients has been demonstrated for a number of applications including absorption spectroscopy [1-7], thermal diffusivity measurements [8], and imaging [9,10]. The magnitude, phase, and temporal profile of the photothermal beam deflection (PTD) signal response may be affected not only by thermal gradients but also by the presence of atoms, ions, electrons, particles in the probed region. Therefore, PTD has also been introduced as a diagnostic technique for studying the mechanisms of phase change during high-power laser irradiation of solids [11-17]. The deflection magnitude and signal shape are dramatically changed in the region of ablation, a complex non-linear explosion-type interaction. Efforts have been made to describe these PTD responses. A change in shape of the beam deflection signal was observed to occur near the ablation threshold [16,17]. A shock wave is generated by ablation of a target in air, and a PTD technique was used to detect a shock wave due to laser ablation and the cooling wave after the shock, based on the direction of the probe beam deflection [12]. PTD was used to determine the laser fluence threshold for ablation in both a vacuum and in air, and the velocity of the ablation products in a vacuum [14,17]. Moreover, the spatial and temporal distribution of the electron density within a laser-induced plasma was deduced by the deflection angle [13]. From these studies, it is apparent that the PTD signal response can provide fundamental information related to complex laser-heating mechanisms.

In this chapter, laser-heating mechanisms at the surface of a solid are investigated in real time using a PTD technique by analyzing the

transient response of the beam deflection signal during a heating cycle. When melt or vaporization occurs, the deflection response of the probe-beam changes due to variations in thermal properties, reflectance, evolution of vapor, among other factors which may greatly affect the temporal shape of the signal. However, even without phase change the shape of the deflection signal may change if the optical beam is deflecting purely from normal thermal gradients caused from heating of the surface with a finite-sized source.

In order to deconvolve complex signal responses which often occur with laser heating, the transient PTD response of a probe-beam needs to be fully characterized for a target under linear heating conditions. The shape of the signal and its amplitude can change dramatically even in this simple heating case depending on the boundary conditions, the material properties, the deflecting medium, the modulation frequency of the probe-beam, and the position of the probe-beam with respect to the target surface. If, as is customary for low-intensity heating, a lock-in amplifier is used to report the amplitude and phase of the PTD signal, important temporal information describing the thermal behavior of heating will be lost. Yet, this shape information can be used to monitor heat conduction into the material and into the adjacent deflecting medium.

This investigation consists of numerical and experimental work to study the effect on the shape, magnitude, and phase of a PTD signal due to changes in

- The thermophysical properties of the target and deflecting medium,
- The dimensions and boundary conditions of the target,

- The distance of the probe beam from the surface of the target, and
- The modulation frequency of the heating source.

For both studies, the effects of thermophysical properties on the temporal PTD response are illustrated by using two different target materials: copper whose thermal diffusivity α_{Cu} is much greater than air α_{air} ($\alpha_{Cu}/\alpha_{air} = 5.286$ @ 293 K), and lead whose diffusivity α_{Pb} is approximately the same as air ($\alpha_{Pb}/\alpha_{air} = 1.102$ @ 293 K) [18].

2.2 Numerical

2.2.1 Model

Figure 2.1 shows a slab of target material, $0 \leq z \leq L$, that is bounded by two semi-infinite media $z \leq 0$ and $z > L$. The target material is a radiatively absorbing medium while the adjoining semi-infinite media are transparent. The target material is irradiated over a circular area of radius w at $z = 0$ by a laser beam of known spatial distribution and temporal behavior. The intensity of the beam is at a maximum at the optical axis ($r = 0$), and decreases both radially and axially. The slab is considered thermally infinite in the radial direction.

An explicit finite-difference method is used to predict transient conduction in the target and the bounding regions. The spatial and the temporal variation of the beam intensity, the temperature dependence of the optical and the thermophysical properties of the materials, and radiative losses from the surfaces are included in the calculations. The absorbed laser radiation is treated as a variable heat source within the material having any value for the optical penetration depth. For laser

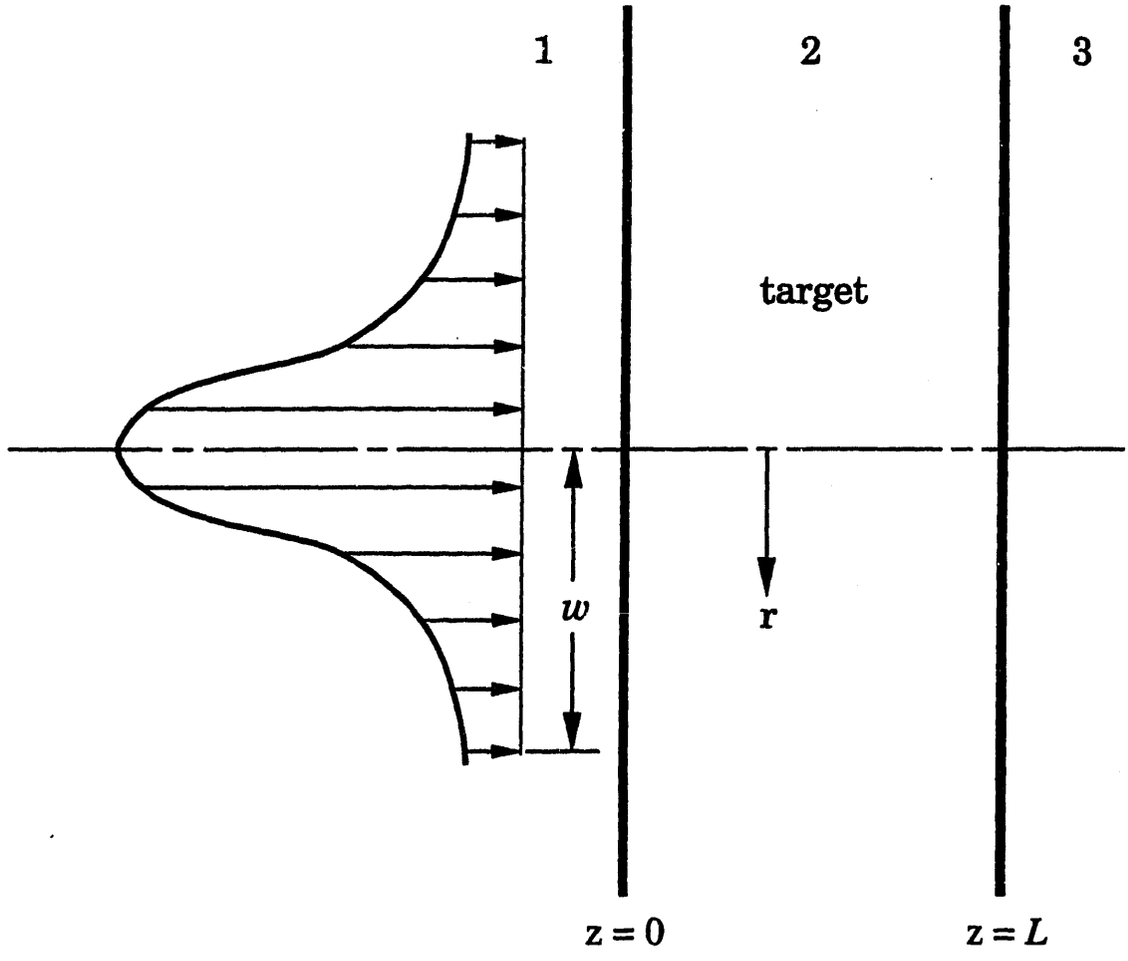

Figure 2.1 Physical model showing beam irradiation on a target with dimensions $0 \le z \le L$.

beams, a commonly used radial distribution of intensity at the surface I_s is the cylindrically symmetric Gaussian profile [19]:

$$I_s(r, t) = I_o\, h(t)\, e^{-r^2/w^2}\,, \qquad (2.1)$$

where h(t) describes the temporal variation of the incident beam with $|h| \le 1$, and I_o is the maximum beam intensity. For a continuous wave laser beam, h(t) = 1. For a modulated beam, h(t) is approximated by triangular, sinusoidal, unit step, or exponential functions. A portion of the incident energy is reflected; the remainder penetrates into the target

material and is partially or completely absorbed. The intensity within the target I_a decreases exponentially as a result of volumetric absorption and its distribution is

$$I_a = I_s (1 - R) e^{-a z}, \qquad (2.2)$$

where R is the reflectivity, and a $\{cm^{-1}\}$ is the optical absorption coefficient. It has been shown by Bonch-Bruevich et al [20], Chun [21] and others [22,23] that the reflectivity R of metals and alloys decreases sharply with time during a laser pulse. The reduction in R is believed to result from increased temperature and from possible chemical reactions at the surface. In this work, R is constant due to small temperature variations.

The energy absorbed may be represented as a heat source within the material having a rate of heat generation per unit volume g given by:

$$g = - \frac{dI_a}{dz} = a I_s (1 - R) e^{-a z}. \qquad (2.3)$$

The two-dimensional diffusion equation for the temperature T in cylindrical coordinates is

$$\frac{1}{r} \frac{\partial}{\partial r} \left(k_j r \frac{\partial T_j}{\partial r} \right) + \frac{\partial}{\partial z} \left(k_j r \frac{\partial T_j}{\partial z} \right) + g_j = (\rho c_p)_j \frac{\partial T_j}{\partial t} \qquad (2.4)$$

where k is the thermal conductivity, ρ is the density, c_p is the heat capacity, and j = 1, 2, 3 corresponds to the regions shown in figure 2.1. Note that g is zero in regions 1 and 3 and is given by equation (2.3) in region 2. The temperature of the target may increase from the initial room temperature up to the fusion temperature of the material. The changes in the thermophysical properties are included in the calculations, though when the temperature rise is small the results reduce to the case of constant properties.

The initial condition is a uniform temperature, $T = T_i$, everywhere. The boundary conditions at the surface $z = 0$ ($r > 0$) are

$$T_1 = T_2 , \tag{2.5a}$$

$$k_1 \frac{\partial T_1}{\partial z} = k_2 \frac{\partial T_2}{\partial z} - \varepsilon \sigma \left(T_2^4 - T_i^4 \right) . \tag{2.5b}$$

It is pointed out that the emissivity ε is not necessarily equal to $(1 - R)$ because the emitted and the reflected energies are not at the same wavelength. Also from symmetry we have

$$r = 0 , \quad \frac{\partial T}{\partial r} = 0 . \tag{2.6a}$$

The other boundary conditions depend on the size of the target and the properties of the material. Generally the lateral dimensions of the target are larger than the radius of the heated spot. Therefore for any value of z:

$$r \rightarrow \infty , \quad T = T_i . \tag{2.6b}$$

The temperature at axial distances far from the surface ($z = 0$) depend on the magnitudes of the thermal diffusion length $\delta_{th} = 2\sqrt{\alpha\, t_p}$, where α is diffusivity and t_p is the heating period, and the absorption length $\delta_o = 1/a$ with respect to the target thickness, L. When both δ_o and δ_{th} are much smaller than the thickness, the boundary condition at the back surface $z = L$ is:

$$z = L , \quad r \geq 0 , \quad T_2 = T_i . \tag{2.7a}$$

On the other hand, if either δ_o or δ_{th} are greater than, or are on the order of the thickness L, the following boundary conditions are used

$$z = L\,, \quad r \geq 0\,, \quad T_2 = T_3\,, \tag{2.7b}$$

$$k_3 \frac{\partial T_3}{\partial z} = k_2 \frac{\partial T_2}{\partial z} + \varepsilon\,\sigma\left(T_2^4 - T_i^4\right). \tag{2.7c}$$

At the two extreme boundaries in regions 1 and 3, the conditions are:

$$z = -\infty\,, \quad T_1 = T_i\,, \tag{2.8a}$$

$$z = +\infty\,, \quad T_2 = T_i\,. \tag{2.8b}$$

It is not necessary to solve for the temperature distribution in region 3 when equation (2.7a) is used as a boundary condition because the heating does not reach that region; i.e. $T = T_i$.

Equation (2.4) is written in an explicit finite-difference form and is solved numerically [24]. The calculations are begun with the temperatures at all the nodal points equal to the initial temperature. The values of the thermal conductivity at the central location between two grid points m and n are needed for calculations and are evaluated according to

$$k_{mn} = \frac{2\,k_m\,k_n}{k_m + k_n}\,, \tag{2.9}$$

which is the geometric average of the conductivities at the nodes. The Fortran computer code was written by Ali A. Rostami.

2.2.2 Results

For the numerical calculations a modulation frequency of 500 Hz was used, which corresponds to a heating period t_p of 1 ms. The intensity of the laser beam was assumed to decrease exponentially in the radial direction and remain uniform during the heating period. A laser beam with an average power of 0.1 W and a $1/e^2$ beam waist of 430 μm was used for all numerical results given here. The back surface of the

target is assumed to be adiabatic. Material properties for copper, lead, and air were taken from Touloukian and Ho [18] recommended values near room temperature.

To examine the accuracy of the numerical calculations a semi-infinite solid having constant properties is first considered. The target is assumed to be insulated from the neighboring regions and irradiated on one of the surfaces by a beam having a Gaussian spatial distribution. The solution to this problem may be obtained using the method of Green's functions [25] and is given by:

$$T(r, z, t) = \frac{p_a}{k\,\pi^{3/2}} \int_0^{\delta_{th}} e^{-z^2/\beta^2}\, e^{-r^2/(\beta^2 + w^2)}\, \frac{d\beta}{\beta^2 + w^2} \quad (2.10)$$

where p_a is the average absorbed power during a pulse. The optical absorption depth for copper and lead is much less than δ_{th}; therefore surface heating is assumed in the targets and heating conditions in the model are similar to those assumed in equation (2.10). The results from the numerical model were compared with the analytical solution of equation (2.10), which was evaluated numerically. The difference between them was less than 1% for the case assumed.

The results of numerical calculations are shown in figures 2.2 to 2.5. Note from figure 2.4 that the temperature variations are ≤ 5°C for these calculations. Figure 2.2 shows the time variation of the temperature gradient in air normal to the surface, at $r = 0$ for three different initial distances z_o from the copper target surface. The copper target in this case is considered to be thermally semi-infinite, because its thickness of 10 mm is much larger than the thermal diffusion length

($\delta_{th} = 0.63$ mm for $t_p = 1$ ms). Three δ_{th}, as determined from a study of the results of the numerical calculations described above, approximates a semi-infinite body in the planar r direction shown in figure 2.1. Note that the vertical axis is actually showing a negative

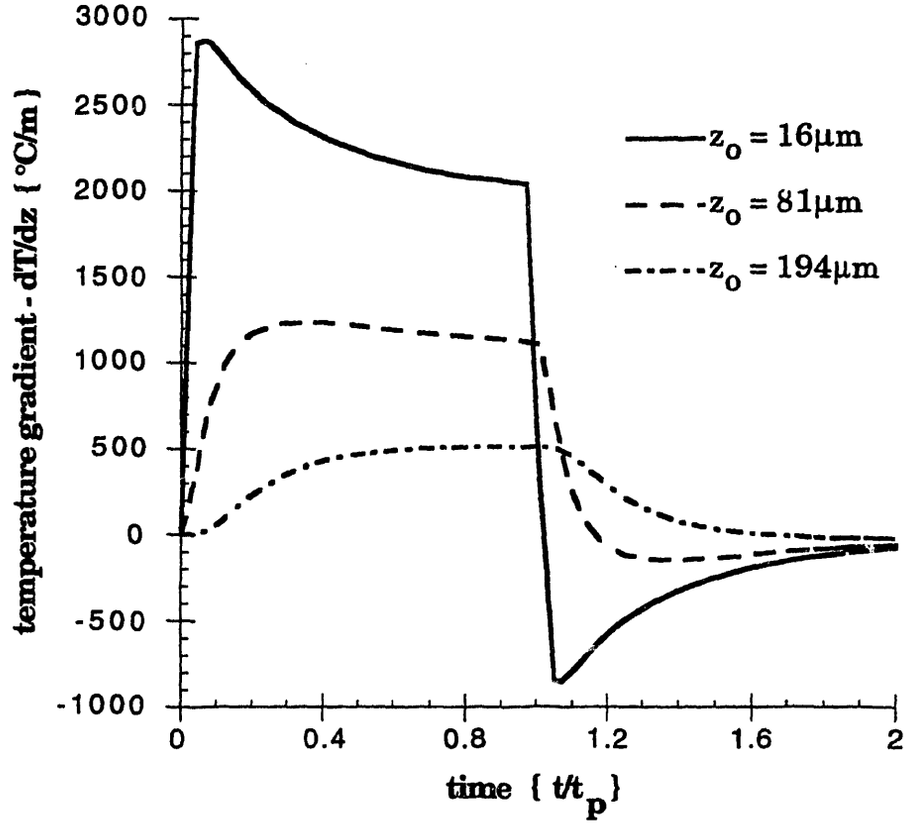

Figure 2.2 Temperature gradient in air at r = 0 for 10 mm thick copper target as a function of z_O.

temperature gradient with respect to z for allcases shown, since heat flows in the direction of negative gradient. Significant changes in the shape and the amplitude of the temperature gradient are seen as the distance from the surface z_o is increased. For $z_o = 16$ μm, the temperature gradient

reaches a local maximum during the heating period, then decreases and asymptotically approaches a steady state value at the end of the heating period. When the power is removed the temperature gradient drops sharply and a change of sign occurs which corresponds to a change in the direction of the heat-flux. The same behavior exists for $z_0 = 81$ μm, although the local maximum is less distinct and the changes are more gradual. For $z_0 = 194$ μm, neither a maximum nor a change of sign of the temperature gradient is seen. Also note that the phase lag of the temperature gradient increases as z_0 is increased.

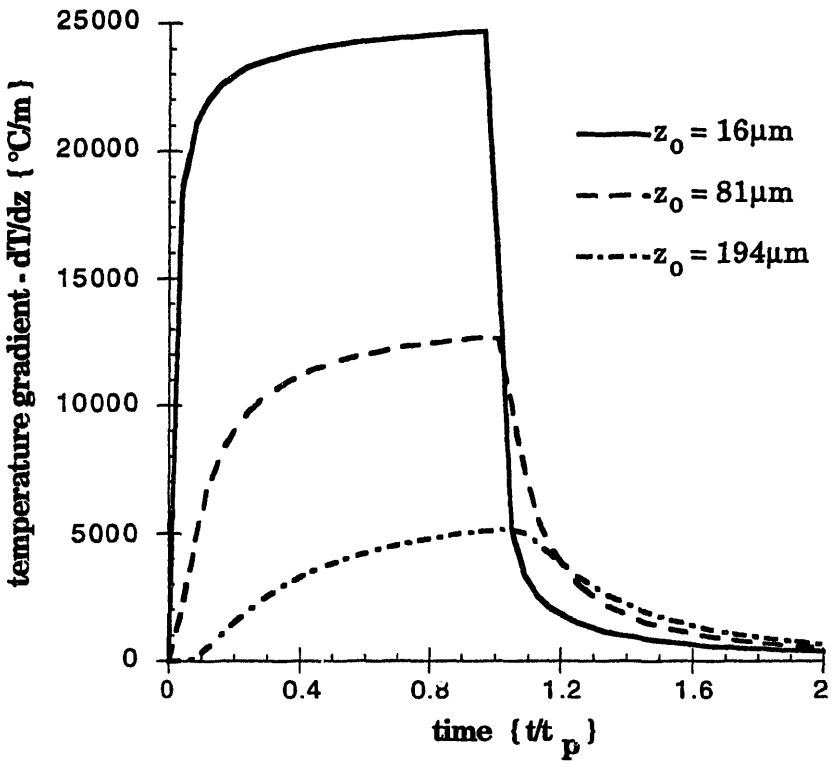

Figure 2.3 Temperature gradient in air at r = 0 for 10 mm thick lead target as a function of z_0.

Figure 2.3 shows the temperature gradients in air at r = 0 for

three z_o for a 10 mm thick lead target. Again as the distance z_o is increased, the peak to peak magnitude decreases and the phase shift of the temperature gradient increases. By comparing the results for copper in figure 2.2 with those for lead in figure 2.3, the effects of the thermophysical properties of the target material on the gradient are seen. For the lead/air combination, no local maxima with respect to time exists for any z_o. Also the temperature gradients show no change of sign after the removal of power. The peak to peak magnitude of the lead/air case is one order of magnitude larger than the copper/air case, due to the small value of the thermal diffusivity of the lead compared to copper.

The effect of material properties on temperature may also be seen in figure 2.4(a & b). Figure 2.4(a) shows the time variation of the temperatures at $r = 0$ inside the copper and in the air at equal distances ($z_o = 63$ μm) from the surface of the target. Figure 2.4(b) shows the same quantities for lead and air. For the copper/air case, at any time during the heating period the temperature inside the target is larger than in the air at the same distance from the surface. The situation is reversed during the cooling period, due to the larger velocity of heat diffusion in copper than in air. On the other hand, figure 2.4(b) shows no distinction between the temperatures inside the lead and in the air. This result is expected because of approximately equal thermal diffusivities of the two materials, which means that the propagation of heat in lead and in air occurs at the same speed. As before with the gradients, the peak to peak temperature for the lead in air case is an order of magnitude greater than for the copper in air case.

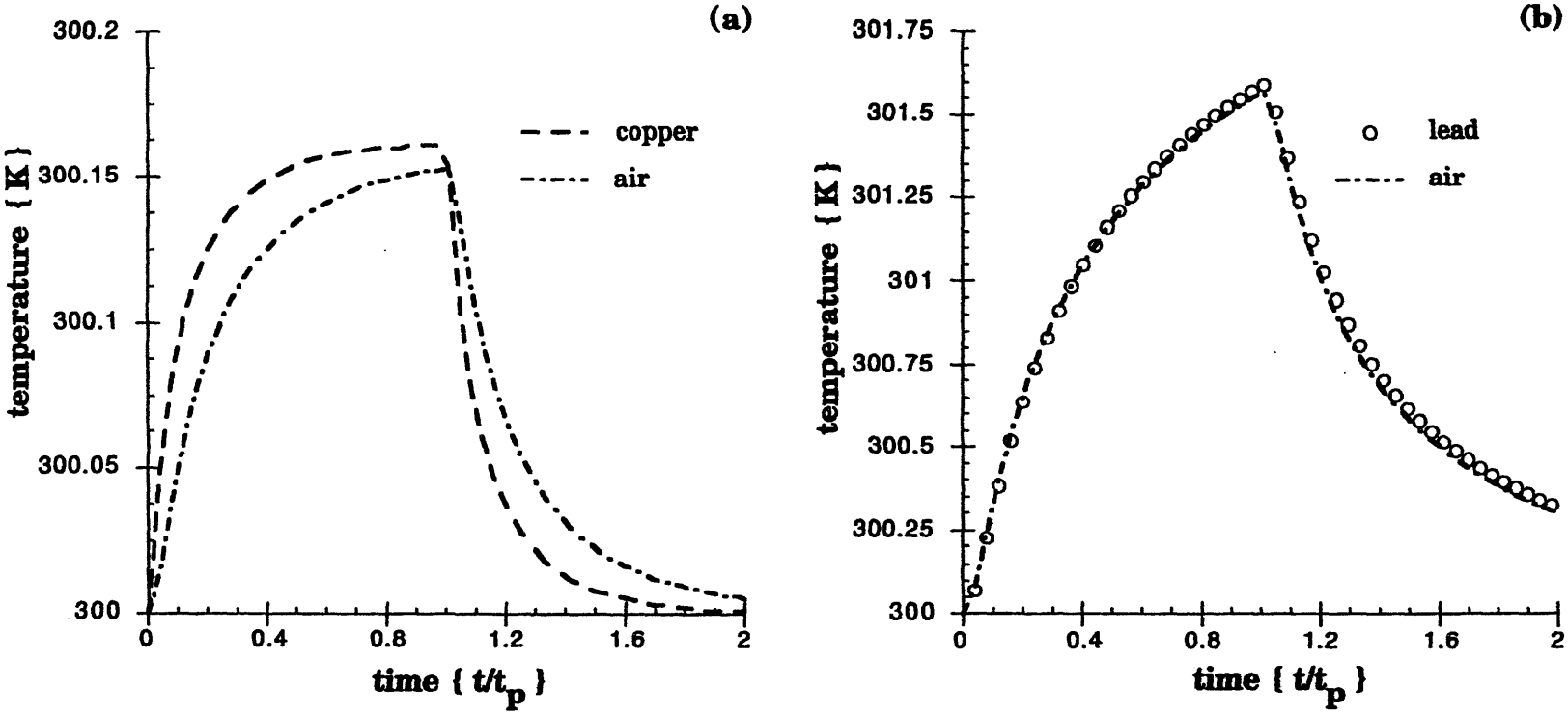

Figure 2.4 Temperature at r = 0 in (a) copper target and air, (b) lead target and air, at equal distance from the surface (z_o = 63 μm).

The effects of changing the thickness of the target on the temporal shape of the temperature gradient in air are shown in figure 2.5. All the parameters except the thickness of the targets are the same in both cases. The thermal diffusion length for copper at a modulation frequency of 500 Hz is 0.63 mm. Therefore, the ratio of L/δ_{th} for the two targets are 0.15 (for $L = 0.1$ mm) and 15 (for $L = 10$ mm), respectively. Figure 2.5 shows that decreasing the thickness of the target results in an increase in the peak to peak magnitude and a change in the temporal shape of the temperature gradient.

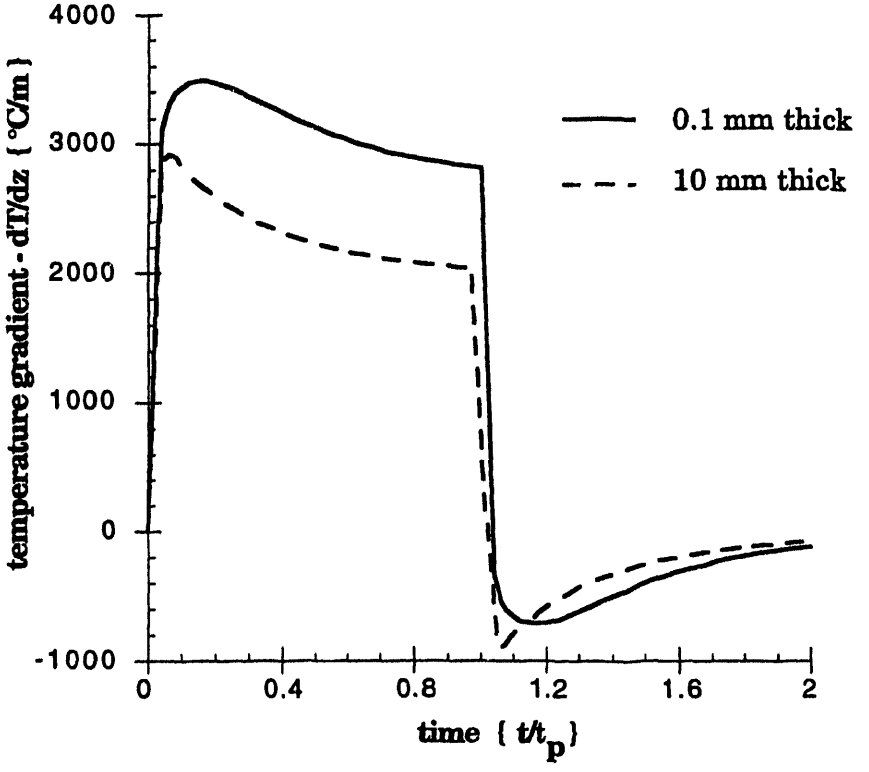

Figure 2.5 Temperature gradient in air for copper targets of thicknesses 0.1 mm and 10 mm ($z_o = 16\ \mu m$).

2.3 Experimental

To unambiguously study changes in the PTD signal requires that the boundary conditions in the experiments are the same for each target sample, that the probe-beam distance z_o is accurately maintained between different samples, and the incident power per unit area absorbed by each sample is constant. The experimental apparatus and procedures were designed with these issues in mind.

2.3.1 Apparatus

The diagram of the apparatus used for the experimental work is shown in figure 2.6. The solid target samples are heated in air and a Uniphase model 1103P He-Ne laser beam adjacent to the surface photothermally deflects due to temperature gradients. The He-Ne probe beam passes through a single 160 mm focal length planoconvex lens L_1. The $1/e^2$ beam waist measured 220 +/- 10 μm, collimated over a length of one cm with the middle of the waist over the center of the target. The waist is measured using a photodiode mounted behind a movable 10 μm pinhole. The deflection of the centroid of the probe beam is measured with a United Detector Technology model LSC-5D continuous, single axis, dual cathode photodetector located 48 cm from the center of the target, and connected to a UDT model 301-DIV amplifier. A Spectra-Physics 3000 Series Nd:YAG laser with a 1064 nm wavelength modulated by a mechanical chopper is used as the heating source. For experiments that correspond with numerical simulations, a 16.7% duty cycle chopper is used to approximate single shot pulses. Otherwise a 50% duty cycle chopper is employed to study the effect of the boundary conditions and frequency on the PTD signals. The pump-beam passes

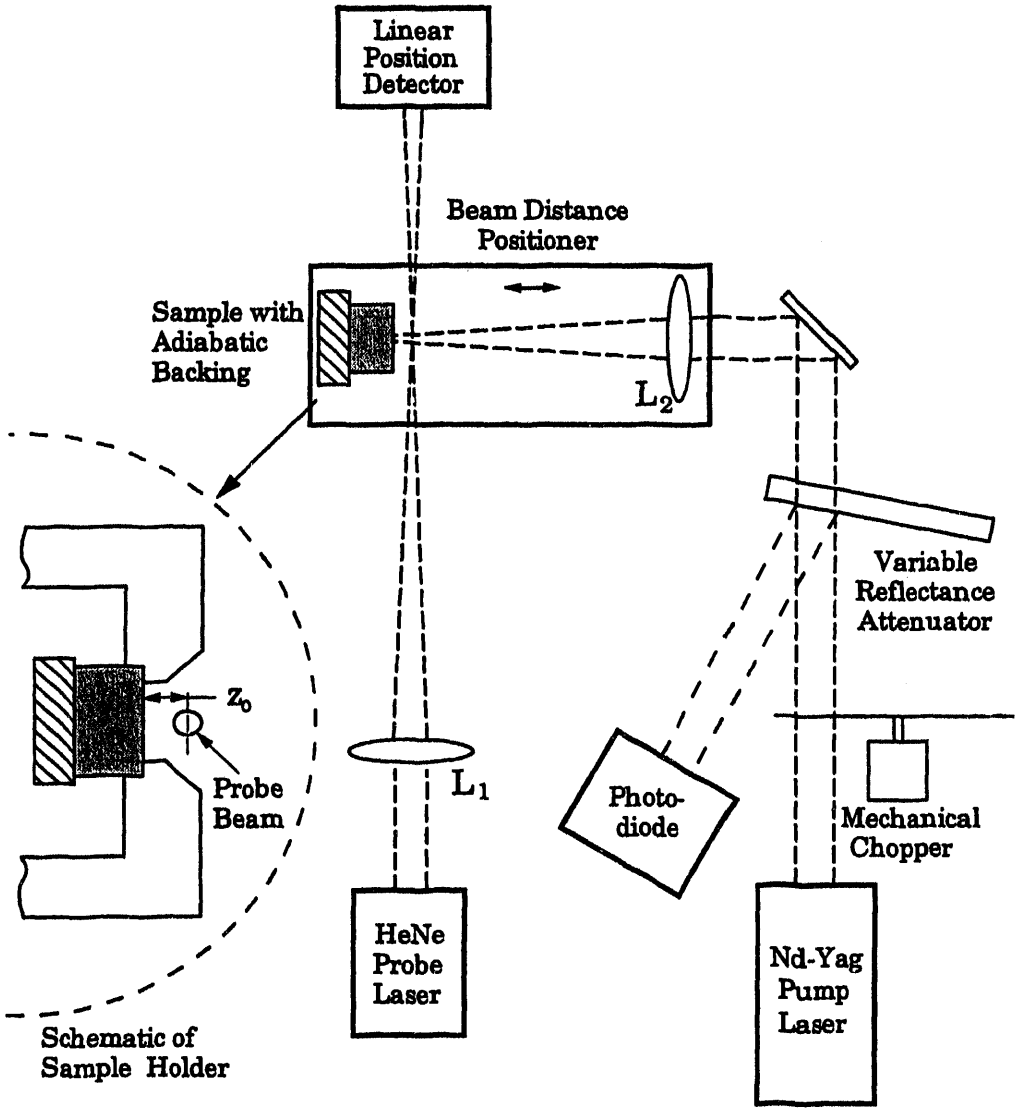

Figure 2.6 Experimental apparatus. L_1 and L_2 are lenses and z_o is the probe-beam centroid distance from target surface.

through a 120 mm focal length lens L_2 with a $1/e^2$ beam waist that measured 430 +/- 10 μm. The pump-beam is focused at the center of the one cm square target, and the diameter remains unchanged during translations of the fixture. In all cases, the probe-beam is aligned so that its centerline orthogonally intersects the centerline of the pump-beam. The incident power on the target sample is adjusted with a variable

reflectance attenuator, and the average power is measured after the chopper. The incident average power in the experiments is 100 mW, which is chosen to ensure that the temperature increase in the target and air is small (less than 5 K), so that thermal convection and radiation from the surface is negligibly small compared to thermal diffusion. The pump-beam's power temporal profile is measured with a fast photodiode. Both the PTD and photodiode signal are recorded using a Tektronix model 7854 digital storage oscilloscope, averaging data over 100 cycles.

2.3.2 Procedures

To mitigate changes to the PTD signal due to deviations of the probe-beam distance z_o, the holding fixture is constructed to repeatedly position each sample along the z axis to within 3 μm. Also, the probe-beam is aligned parallel to the holder to within 10 μ radian. The z_o distances are adjusted by moving the fixture on a translation stage with micron adjustments. The initial centroid distance z_o is measured by cutting off the probe-beam by the target and then moving the translation stage until the probe laser light begins grazing the surface. The first obtainable PTD signal is assumed to occur at a z_o distance of 10 μm. This initial distance is approximately confirmed by using single-ray theory at z_o distances far from the surface.

The incident power per unit area absorbed by the target is dependent on the surface finish of the sample, as well as its reflectivity, for a given wavelength of the excitation laser light. To ensure that the absorbed power is the same for each sample, the targets were machined, lapped smooth and flat to the same surface finish, and then sputtered with

a 25 nm thick coating of stainless steel to give a measured reflectivity of 20.5 +/- 1% at a wavelength of 1064 nm.

To meet the experimental requirements for the boundary conditions, the target dimensions are chosen to be parallelepiped bodies, one cm squares with different thicknesses L. The one cm square dimension ensures at least three thermal diffusion lengths δ_{th} from the pump-beam radius to the side boundaries (for the lowest modulation frequency and the highest diffusivity material). The effects of the side boundary conditions on the temperature field in the target are then assumed to be negligible when the results are compared between samples. The back of the targets are insulated to approximate an adiabatic boundary condition for each sample.

To study the effect of the target composition on the PTD signal, one cm cubes of copper and lead are used. For a one ms pulse, the dimensions of the target are much greater than the δ_{th} of copper and lead so that the samples are essentially thermally semi-infinite in extent. With the samples thermally semi-infinite, the transverse probe-beam centered with the pump-beam, and the modulation frequency of the pump-beam held constant, the changes in shape, magnitude, and phase of the PTD signal are only a function of the thermal diffusion properties of the sample and air, and the z_o distance of the probe-beam from the surface.

To study the effect of the back boundary condition on the shape and magnitude of the PTD signal, the thickness of the samples are varied, keeping the same modulation frequency and z_o distance. Copper is used due to its relatively high α, so that the effect of the adiabatic boundary condition is readily observed when the sample is thermally finite in its

thickness. The main parameter of interest here is the ratio of the thickness of the sample to the thermal diffusion length, L/δ_{th}. With the z_o approximately 80 μm and the frequency at 86.4 Hz, three targets are used with thicknesses of 5, 1, and 1/2 mm, which corresponds to L/δ_{th} of 3, 0.6, and 0.3 respectively. Each sample, then, meets the semi-infinite condition of $L/\delta_{th} \geq 3$ for the sides, but changes from being thermally semi-infinite to finite in thickness.

To study the effect of frequency on the PTD signal, two series of measurements are obtained. First, the ratio of L/δ_{th} is held constant at one for the different sample thicknesses above, so that the boundary conditions are the same for each sample. For the second case, L/δ_{th} is varied by changing the frequency and using a 10 mm copper target which behaves thermally semi-infinite. These two cases show the effect of thickness and frequency on the shape and magnitude of the PTD signal.

2.3.3 Results

In this section, the PTD signal response for various conditions described above is presented. Comparisons of these results to the numerical analysis will be presented in the following discussion section.

For the semi-infinite 10 mm thick copper sample, the PTD signals for different z_o distances are shown in figure 2.7. The photodiode signal is included in the figures as a reference of magnitude and phase for each of the PTD signals. The input power is held constant for all the experiments and the photodiode signal is normalized to one. Note that the temporal profile for the power is not a true square wave, but has a finite rise-time because the modulation is from a mechanical chopper. The

rounding-off of the corners is due in part to the finite size of the pump beam and its Gaussian spatial profile. The deviation of the input power waveform from a true square wave causes the PTD signal to have longer rise and fall times and greater rounding at the corners of the signal than that predicted by the numerical model.

Of main importance in figure 2.7 is that the shape of the PTD signal changes as z_o increases from approximately 15 μm to 190 μm. In figure 2.7(a) for z_o at 15 μm, a distinct local maximum is observed in the PTD signal with respect to time during the period of heating. Furthermore, when the

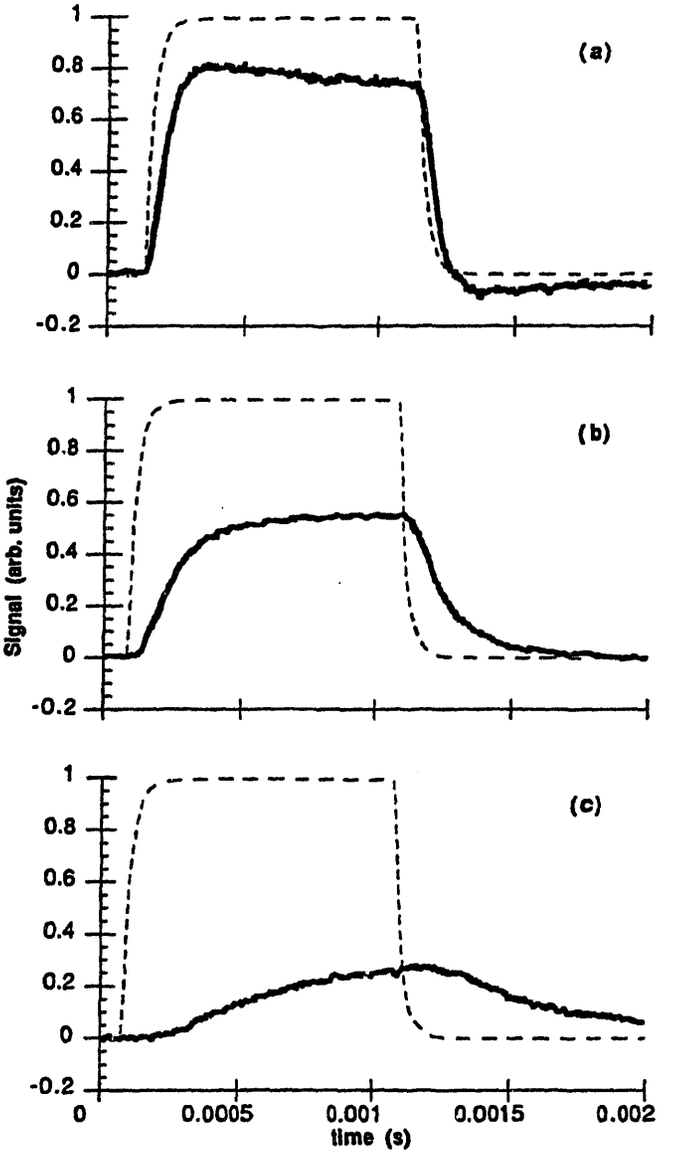

Figure 2.7 PTD signals for 10 mm thick copper target. The probe-beam centroid distances are (a) z_o = 15 μm, (b) z_o = 80 μm, and (c) z_o = 190 μm. Dashed line is the normalized pump-beam photodiode signal.

power is removed, the PTD magnitude becomes negative with respect to the start of the pulse, corresponding to a reversal in the direction of the deflection of the probe beam. In figure 2.7(b & c), for z_o at 80 μm and 190 μm, neither local maxima nor negative deflections are observed. The PTD signals follow a follow a classic exponential rise and decay following the power input. The magnitude the PTD is also seen to decay and the phase is observed to lag the power input as z_o increases.

For the thermally semi-infinite 10 mm thick lead sample, the PTD signals for z_o at 15 μm, 80 μm, and 190 μm are shown in

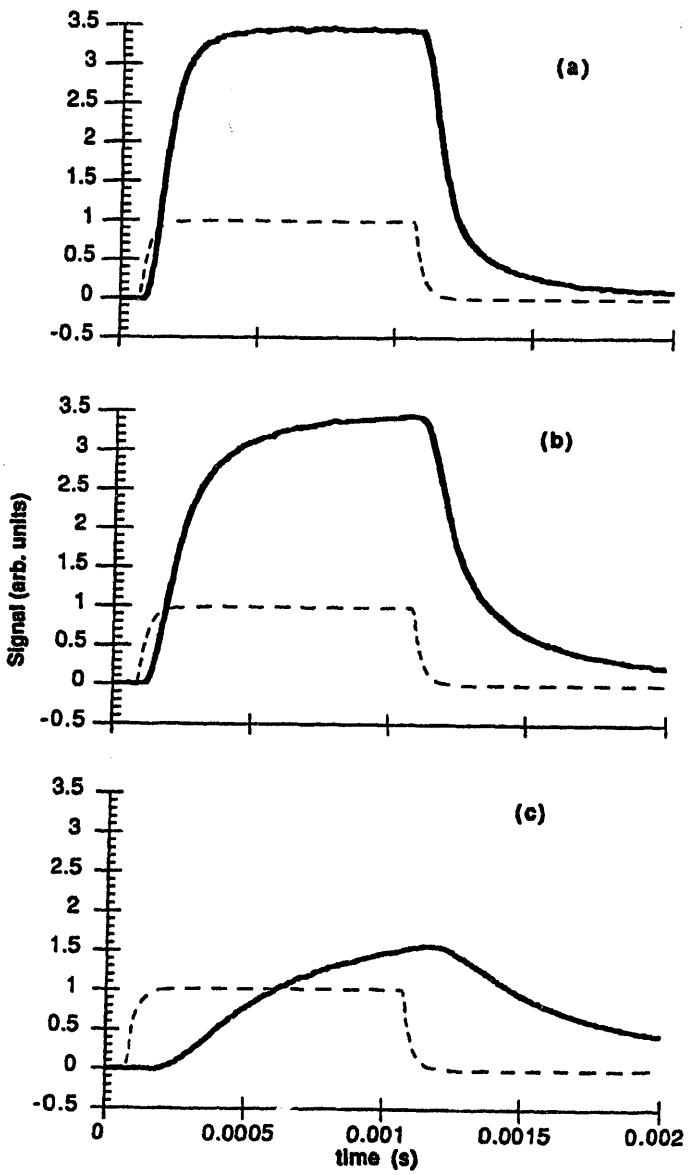

Figure 2.8 PTD signals for 10 mm thick lead target. The probe-beam centroid distances are (a) z_o = 15 μm, (b) z_o = 80 μm, and (c) z_o = 190 μm. Dashed line is the normalized pump-beam photodiode signal.

figure 2.8. For the lead sample, no local maxima with respect to time are observed, although for z_o at 15 μm shown in figure 2.8(a) the magnitude reaches a steady-state level. Also, the PTD signal never shows a reversal in direction; just a classic signal decay.

The effect of the sample thickness L on the shape of the PTD signal is shown in figure 2.9 for a constant modulation frequency of 86.4 Hz. As the L/δ_{th} ratio changes from 3.0 in figure 2.9(a) to 0.3 in figure 2.9(c), the PTD signal changes shape from showing a distinct local maximum and direction reversal, to not having a local maximum or a reversal.

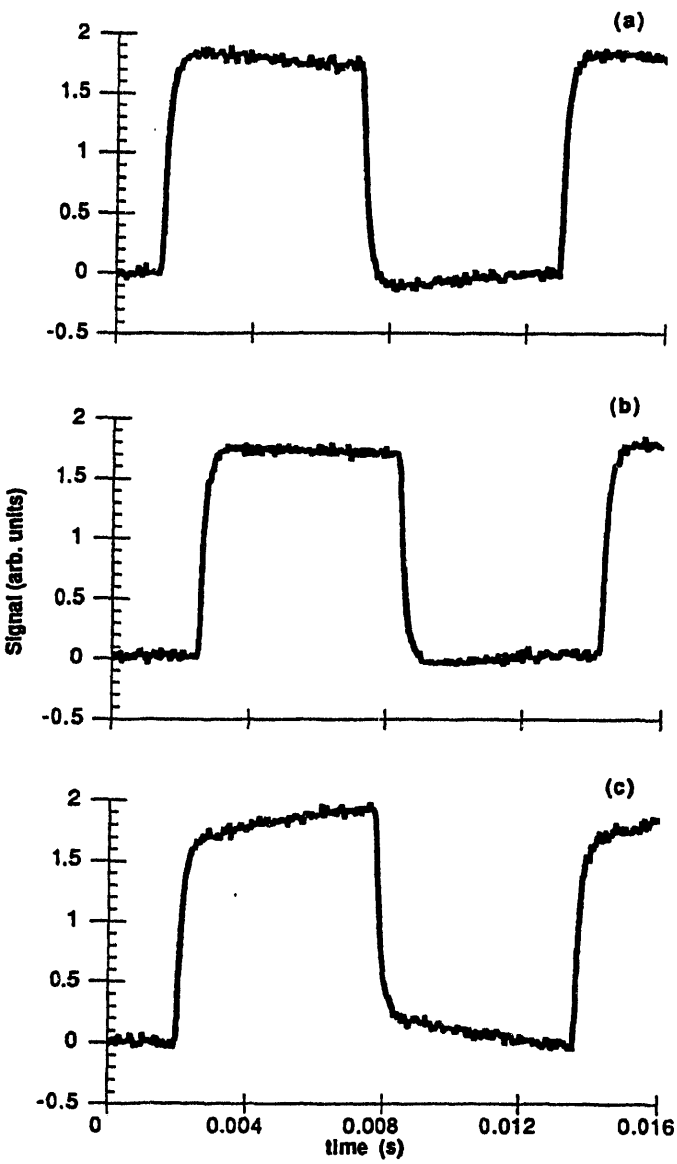

Figure 2.9 Effect of target thickness on PTD signal at constant modulation frequency of 86.4 Hz. L/δ_{th} are (a) 3, (b), 0.6, (c) 0.3. Targets are copper and z_o = 50 μm.

The effect of modulation frequency on the PTD signal shape is shown in figure 2.10, where the L/δ_{th} ratio is held constant at one so that each sample has the same thermal thickness. A sharp maximum and reversal is observed in figure 2.10(a) at a modulation frequency of 9.6 Hz, with no local maximum and reversal at 240 Hz and 960 Hz in figures 2.10(b & c). At 9.6 Hz, the side boundaries cannot be considered semi-infinite, and at the later portion of the pulse heat transfer occurs along the sides of the target. This side boundary effect results in the steady-state value observed near the end of the PTD signal.

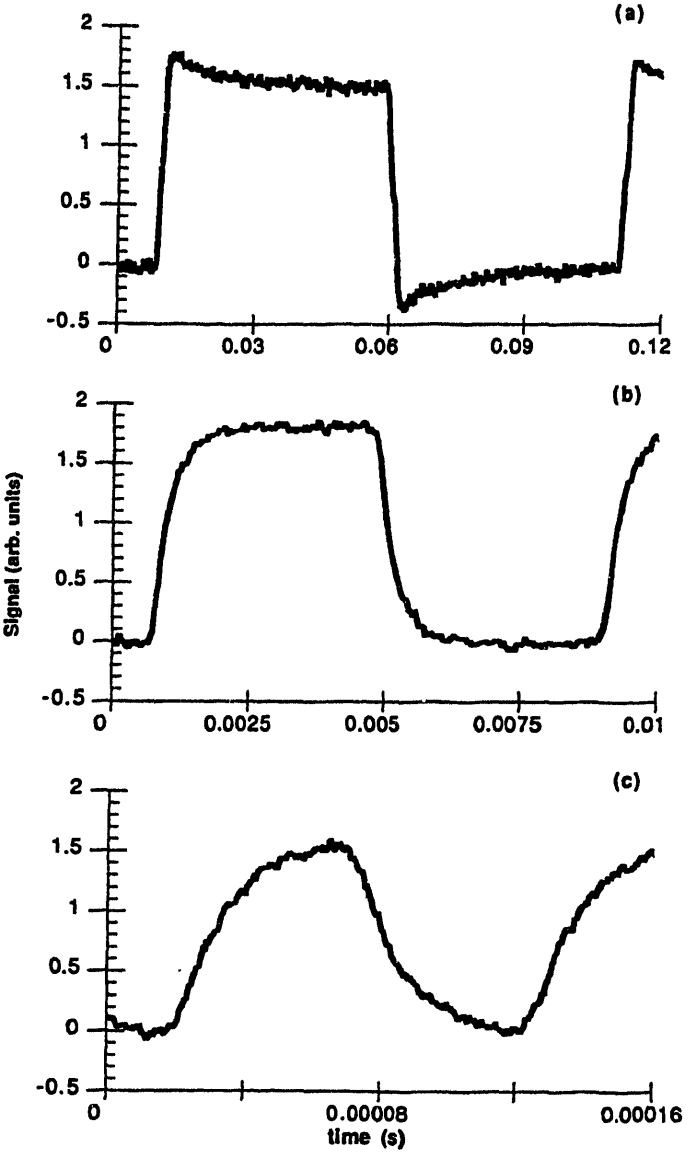

Figure 2.10 Effect of modulation frequency on PTD signal at constant L/δ_{th} of 1. Frequencies are (a) 9.6 Hz, (b) 240 Hz, (c) 960 Hz. Targets are copper and $z_o = 50$ μm

The effect of frequency on the PTD signals is also seen in figure 2.11 for the 10 mm copper sample at 1500 Hz, 540 Hz, and 86.4 Hz. In all these cases the sample is thermally semi-infinite. With z_o at approximately 50 μm, the peak to peak magnitudes are about 0.1 for all three cases. However, the shape of the signal changes from a sawtooth pattern in figure 2.11(a) to that which exhibits a local maximum in figure 2.11(c).

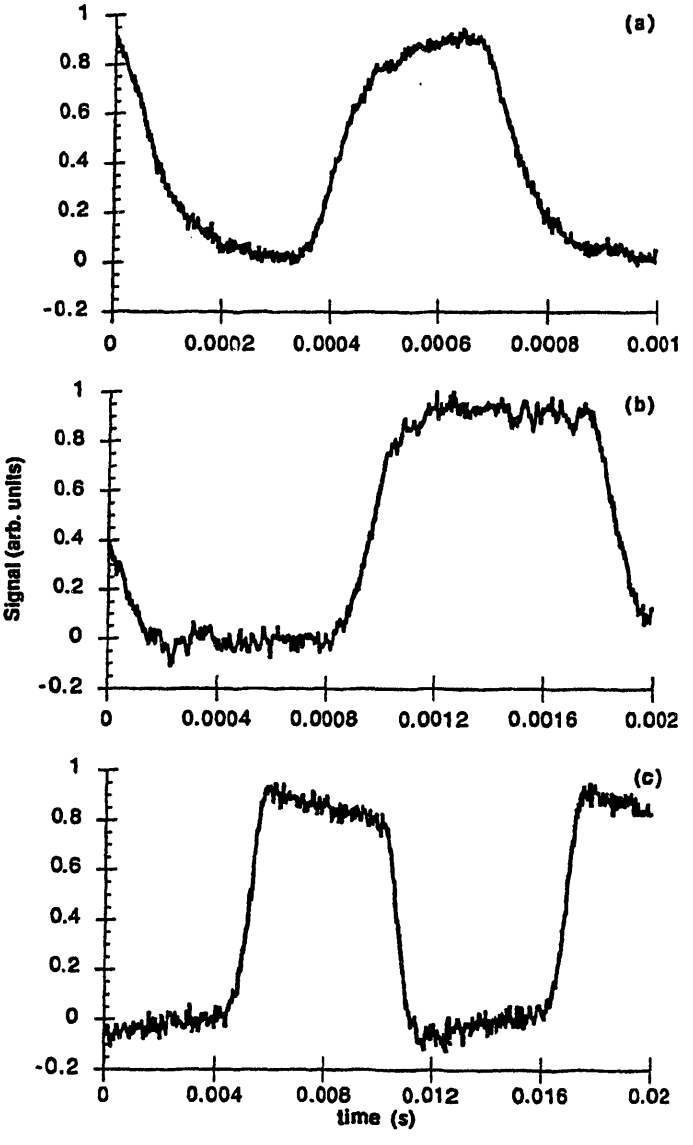

Figure 2.11 Effect of modulation frequency on PTD signal with thermally semi-infinite 10 mm thick copper target. Frequencies are (a) 1500 Hz, (b) 540 Hz, (c) 86.4 Hz. z_o = 50 μm.

2.4 Discussion

Since the probe-beam deflects due to perpendicular temperature gradients in the air adjacent to the samples, the PTD signal gives a measure of the heat-flux normal to the surface of the target. Before qualitatively comparing the numerical simulations of $\partial T/\partial z(r = 0)$ in air for different z_o with the PTD signals whose probe-beam centroid corresponds with those z_o distances, the effects on the PTD signal of a traversing probe-beam with finite dimensions must first be considered. As the probe-beam traverses the target, it is integrating the effects of $\partial T/\partial z$ across the width of the sample to produce the PTD signal. Due to the radial symmetry of the temperature field in the experiments, the total angular deflection θ from the traverse integration of an infinitely thin beam can be expressed as some function of $\partial T/\partial z(r, z)$, or

$$\theta = \int f\left(\frac{\partial T}{\partial z}(r, z), r, \ldots\right) dr \,, \qquad (2.11)$$

for a given z and time t. A more complete discussion of the calculation of the probe beam deflection is given in chapter 3. The effect of the finite size of the probe-beam, however, should change the shape of the PTD signal because $\partial T/\partial z$ changes across the z direction of the beam. The portion of the beam closest to the surface will experience greater deflections than the regions farthest from the surface. The resulting PTD signal will be an integration of θ over z as well as r and should appear qualitatively as a convolution of single-ray deflections corresponding to $\partial T/\partial z(r, z)$ at different z_o. Therefore, variations in both r and z will

alter the shape of the PTD signal from that of the shape of the central gradient $\partial T/\partial z(r = 0)$ over time for a given z_o.

The comparisons of the numerical simulations with the experimental PTD data are as follows. For the case of the copper where the ratio of diffusivities is about 5.3, both the numerical simulation of $\partial T/\partial z$ in figure 2.2 and the experimental PTD data in figure 2.7(a) show a local maximum for z_o at approximately 15 μm. While the maximum is sharp for the numerical simulation compared to the PTD data, recall that the probe-beam is finite in size and the input power is not an ideal square wave. The PTD signal will not follow $\partial T/\partial z(r = 0)$ precisely, but will show rounding and truncation compared to the numerical result. Indeed, in figure 2.7(a) the shape appears as a convolution of $\partial T/\partial z(r = 0)$ for z_o at 16 and 81 μm from figure 2. However, both model and experiment show a local maximum during the heating pulse and a reversal in the sign of the temperature gradient with time for z_o close to the surface. For z_o at 80 μm, the numerical simulation shows a slight maximum whereas the PTD signal in figure 2.7(b) does not, which also can be explained as above. For z_o at 190 μm, neither the numerical nor experimental results show a maximum or reversal. Therefore, in both studies a point is reached at some distance z_m from the surface where a local maximum no longer occurs for the copper and air domain.

For the lead/air case in which the diffusivity ratio is 1.1, neither the numerical nor experimental studies show any local maxima or reversals in time. The PTD signal in figure 2.8(a) shows that a steady-state value is reached with z_o at 15 μm, whereas the numerical simulation in figure 2.4 does not. However, the finite-sized probe-beam has regions

grazing the surface which should distort the PTD signal as discussed above. A question arises because α_{pb}/α_{air} is not exactly one; is there some z_o distance or modulation frequency that will produce a local maximum for this case? As figure 2.12 shows for z_o at 15 μm, a maximum is observed when the pulse duration is about 8 times longer (modulation rate = 62 Hz) than for the case shown in figure 2.8(a). However, the side boundaries cannot be considered semi-infinite and will influence the shape of the signal later in the pulse. Comparing figures 2.7, 2.8, and 2.12 shows that the ratio of diffusivities between the sample and the deflecting medium determines the pulse length or modulation frequency necessary to produce a maximum in the PTD signal.

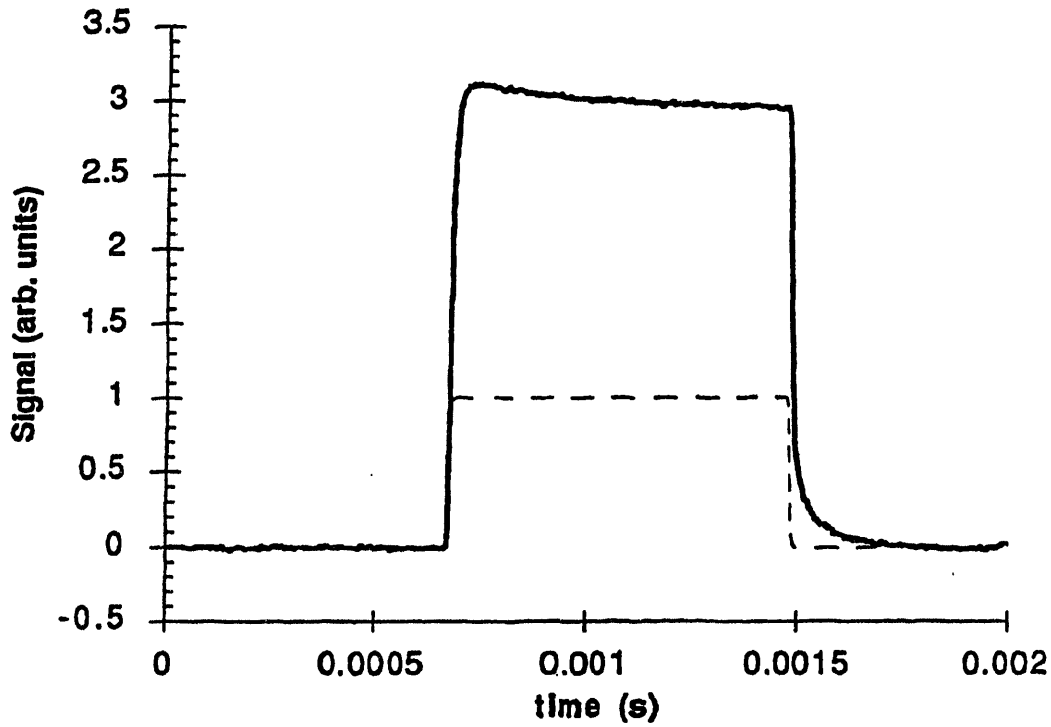

Figure 2.12 Observed maxima in $\partial T/\partial z$ for lead target. Modulation frequency is 62 Hz, and z_o = 15 μm.

A primary conclusion of the numerical and experimental studies is that the shape of the PTD signal can exhibit a local maximum in time during the heating period when there is a small finite heat source, the solid target has a different diffusivity than the deflecting medium, and the probe-beam centroid distance z_o is close to the surface. That a local maximum exists when z_o is small is particularly worrisome, since as figure 2.11 shows, the peak to peak magnitudes remain the same yet the shape changes dramatically. If a lock-in amplifier were used to record the PTD signal, the magnitude and phase might be altered due to the shape change depending on the type of reference signal used. Also, the occurrence of a loc l maximum in the PTD signal will not be directly observed by a lock-in and any change in signal shape will be difficult to predict using this detection method. The constant peak to peak magnitude is qualitatively explained using a simplified theory for probe-beam deflection assuming a single ray and uniform surface heating [4]. For this case the amplitude of the signal is derived as a function of the z_o distance, given by

$$A = A_0 \exp\left(z_o \sqrt{\pi f / \alpha}\right) \qquad (2.12)$$

and as $z_o \rightarrow 0$, then $A \rightarrow A_0$, which is assumed here to be a constant for low-temperature heating in air. Therefore, little change in peak to peak magnitudes should be observed as the frequency changes when z_o is small, as is seen in figure 2.11.

When a local maximum occurs at a z_o ($r = 0$), the temperature gradient normal to the surface declines after some point in time. This might suggest that the surface temperature declines with time or that the heat-flux entering the air declines in time. Yet the numerical solutions

for temperature shown in figure 2.4(a & b) indicate that the temperature increases until the power is removed. Also, energy balance considerations require that the total heat flux not decline with time. For two simple cases it can be shown that maxima in $\partial T/\partial z$ will not occur in time. Expressions for $\partial/\partial t(\partial T/\partial z)$ obtained from analytical solutions for temperature from Carslaw and Jaeger [25] for semi-infinite domains with different α heated by an infinite, planar heat source show that a maximum would never occur for any combination of z or α. A more general result demonstrating this case is given in chapter 3.3.3. Also, if the heat source was a point source, no maximum in time would occur if α were the same for each domain. For both these cases, the temperature field has a high degree of symmetry with time as shown by the isotherm in the left-hand-side of figure 2.13(a & b). Therefore, the heat flows only in one direction for all time, i.e. in the z direction for the planar source and in the radial direction for the point source, as depicted by the flux vector **q** in the right-hand side of figure 2.13(a & b) for increasing time increments.

However, when the heating source is finite in size, and when the domains have different α, the temperature field changes in time and does not maintain the same spatial symmetry. Shown conceptually in the left-hand side of figure 2.13(c) is the same isotherm in region 2 at different times t when α_1 is much greater than α_2, similar to the copper/air case. Note the lack of symmetry in the ϕ direction compared to the case in figure 2.13(b) where α_1 equals α_2. While the overall thermal energy balance is maintained, the direction of the heat-flux shifts in time depending on position r, as is seen in the right-hand side of

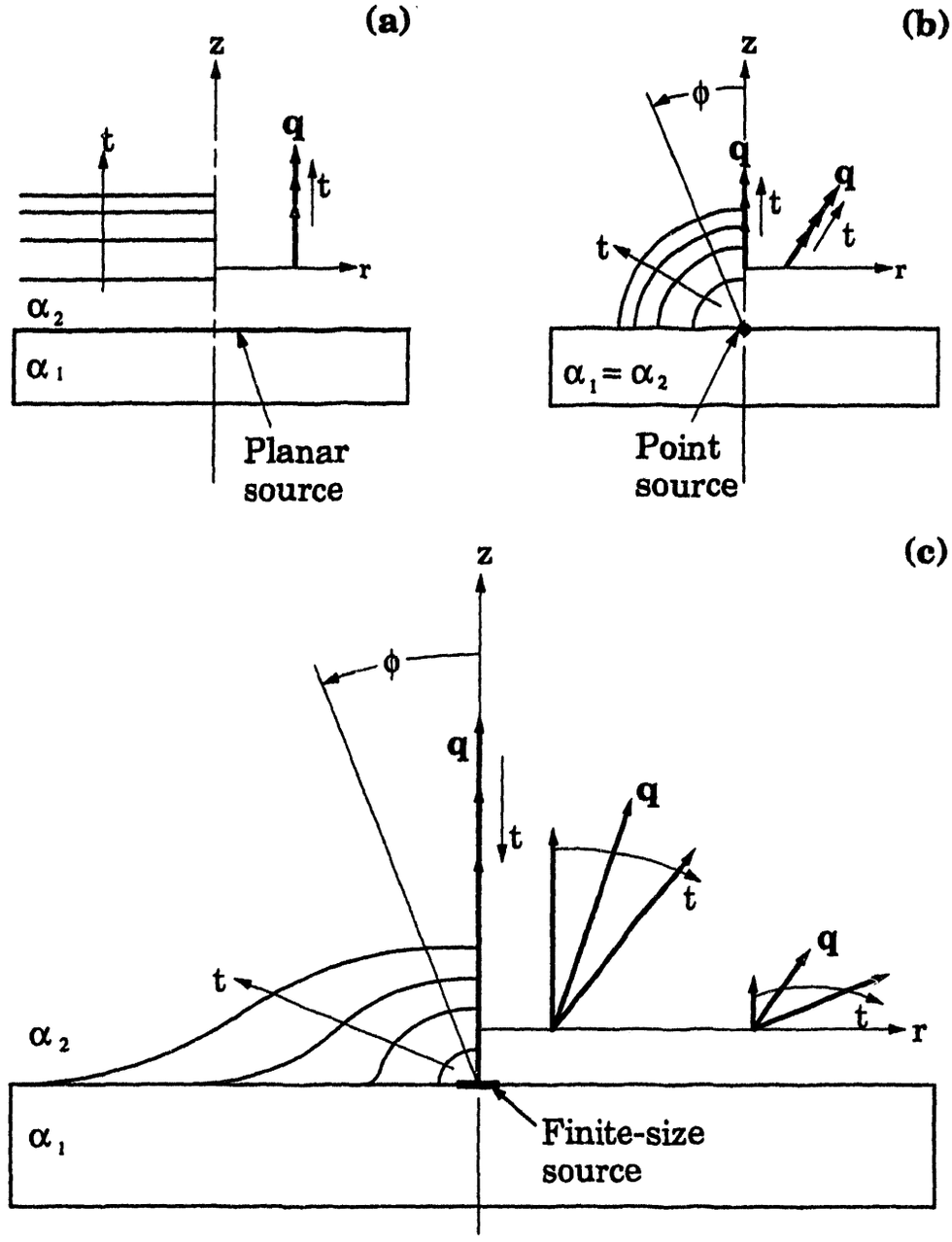

Figure 2.13 Concept drawings of temperature field and heat flux directions as a function of time for 3 cases; (a) $\alpha_1 > \alpha_2$ with a planar source, (b) $\alpha_1 = \alpha_2$ with a point source, (c) $\alpha_1 > \alpha_2$ with a finite-size source. The left-hand-side of each drawing shows the same isotherm at different times. The right-hand-side shows the magnitude and direction of the heat flux at different points. t indicates direction **q** changes with time.

figure 2.13(c). This shift in flux direction does not occur for the cases shown in figure 2.13(a & b). At small z_o distances for all $r > 0$ when $\alpha_1 > \alpha_2$, the flux direction shifts with time from the normal direction more to the radial direction. Therefore, the normal components of the flux vectors decrease in time after a maximum is reached. The resulting PTD magnitude, then, will also reach a maximum and decrease. As z_o is increased, the temperature field about a point begins to look more planar, analogous to the curvature of a sphere decreasing as the radius is increased, until at some point z_m the normal flux does not exhibit a maximum in time. While an analytical solution to this problem is not easily tractable, the numerical solutions of figures 2.2 & 2.3 show that a relationship exists between z_o, δ_{th}, α_1/α_2, and a maximum in $\partial T/\partial z$ with time.

The dimensions and boundary conditions of the target also play a role in the shape of the PTD signal. As seen in figure 2.9, when the frequency is held constant so that δ_{th} in the sample and deflecting medium remain constant, the signal shape can change by only changing the thickness of the target. As the thickness becomes small, the temperature field in the sample becomes more planar and the direction of the heat flow into the air becomes more normal to the surface. The numerical simulation shown in figure 2.5 also shows that the magnitude and shape change as the thickness is changed, both in the time it takes for the local maximum to occur and in the slope after the maximum. By changing the target dimensions, the boundary conditions cause the temperature field to change with time in a thermally finite domain, thereby changing the direction of the heat-flux in the air and therefore the PTD signal.

The effect that the modulation frequency has on the temperature field in air is seen in figure 2.10. With z_o and the ratio of L/δ_{th} for the sample held constant, the shape of the PTD signal changes with frequency since δ_{th} for the air is changing. When the modulation frequency is high (960 Hz in figure 2.10(c)), the distance that the thermal information travels during t_p is shorter than for lower frequencies. In this case, z_m required to observe a maximum in $\partial T/\partial z$ becomes shorter. However, as the frequency drops and δ_{th}(air) becomes larger, z_m increases until a local maximum is observed as in figure 2.10(a). Therefore, the modulation frequency influences whether a local maximum occurs at a given probe-beam distance z_o.

2.5 Conclusion

Numerical and experimental studies show that in addition to the magnitude and phase, the temporal profile of the PTD signal contains fundamental information on the transient heat flow in the target and deflecting medium. The factors that effect the shape of the PTD signal for simple heating are the thermophysical properties of the target and deflecting medium, the overall dimensions and boundary conditions of the target, the modulation frequency and size of the heat source, and the distance of the centroid of the probe-beam from the target surface. An unusual phenomenon can occur when heating with a laser or a finite-sized heating source. When the diffusivity of the target and deflecting medium are different and the probe-beam is close to the surface, a local maximum in time during the heating period can be observed in the PTD signal. From the numerical studies, local maxima in $\partial T/\partial z(r = 0)$ with time are

also predicted to occur when z_o is small with respect to δ_{th} for air. Correlating the numerical with the experimental studies shows that the maximum in the PTD signal results from the temperature field which changes asymmetrically over time. The direction of the heat-flux shifts from being normal to the surface to having radial components. Since a probe-beam in simple heating deflects due to temperature gradients perpendicular to the surface and the magnitude of the normal gradient declines due to the flux changing directions, the PTD signal exhibits a local maximum.

When heating, melting, vaporizing, or ablating a solid with a laser, the heating source is finite and generally small in size. If a PTD technique is used to monitor one of these processes, great care must be exercised when interpreting the results, particularly if using a lock-in amplifier. Perhaps more important is the information contained in the temporal shape of the PTD signal due in part to the temperature field of the target. The onset of phase change due to melt and vaporization should change the resulting temperature field over time, and thus the shape of the PTD signal. The work in this area in chapter 3 reveals that the onset of phase change at the surface of a laser target can be detected in real time.

References

[1] A.C. Boccara, D. Fournier, W. Jackson, and N.M. Amer, Opt. Lett. **5**, 377 (1980).

[2] A. Mandelis, J. Appl. Phys. **54**, 3404 (1983).

[3] W.B. Jackson, N.M. Amer, A.C. Boccara, D. Fournier, Appl. Opt. **20**, 1333 (1981).

[4] J.C. Murphy and L.C. Aamodt, J. Appl. Phys. **511**, 4580 (1980).

[5] L.C. Aamodt and J.C. Murphy, J. Appl. Phys. **52**, 4903 (1981).

[6] A.C. Tam, Rev. Modern Phys. **58** (2), 381 (1986).

[7] E.L. Lasalle, F. Lepourte, and J.P. Roger, J. Appl. Phys. **64**, 1 (1988).

[8] L. Fabbri, Mater. Chem. Physics **23**, 447 (1989).

[9] G.C. Wetsel, Jr. and F.A. McDonald, J. Appl. Phys. **56**, 3081 (1984).

[10] G. Busse, Optics Commun. **36** (6), 441 (1981).

[11] M. Dienstbier, R. Benes, P. Rejfir, and P. Sladky, Appl. Phys. B **51**, 137 (1990).

[12] G. Koren, Appl. Phys. Lett. **51**, 569 (1987).

[13] C.L. Enloe, R.M. Gilgenbach, and J.S. Meachum, Rev. Sci. Instrum. **58**, 1597 (1987).

[14] S. Petzoldt, A.P. Elg, M. Reichling, J. Reif, and E. Matthias, Appl. Phys. Lett. **53**, 2005 (1988).

[15] E. Heidecker, J.H. Schafer, J. Uhlenbusch, and W. Viol, J. Appl. Phys. **64**, 2291 (1988).

[16] J.A. Sell, D.M. Heffelfinger, P. Ventzek, and R.M. Gilgenbach, J. Appl. Phys. **69** (3), 1330 (1991).

[17] J.A. Sell, D.M. Heffelfinger, P. Ventzek, and R.M. Gilgenbach, Appl. Phys. Lett. **55**, 2435 (1989).

[18] Y.S. Touloukian and C.Y. Ho, Eds., *Thermophysical Properties of Matter*, (Plenum Press, New York 1972).

[19] M. Von Allmen, *Laser Interactions with Materials*, (Springer-Verlag, New York 1987) p49.

[20] A.M. Bonch-Bruevich, Ya Imas, G.S Romanov, M.M. Libenson, and L.N. Mal'tsev, Soviet Phys.-Tech. Phys. **13**, 640 (1968).

[21] M.K. Chun, IEEE J. Quantum Electron **QE-5**, 316 (1969).

[22] J.F. Ready, IEEE J. Quantum Electronics **QE-12**, 137 (1976).

[23] P.W. Chan, Y.W. Chan, and H.S. Ng, Phys. Lett. **61A**, 151 (1977).

[24] A.A. Rostami, R. Greif, and R.E. Russo, ASME Transp. Phen. Material Process. **HTD-146**, 61 (1990).

[25] H.S. Carslaw and J.C. Jaeger, *Conduction of Heat in Solids* 2nd ed, (Oxford University Press, Oxford 1959).

Chapter 3
Detecting Laser-Induced Phase-Change at the Surface of Solids via Latent Heat of Melting with a Photothermal Deflection Technique

In this chapter, the detection of laser-induced melt at the surface of a solid in real time is demonstrated using the photothermal deflection (PTD) technique developed in chapter 2. Experimental results are presented for indium and tin that show a local maximum and minimum pair can occur in the temporal profile of the PTD signal when melt occurs. Analytical work is presented which explicitly shows the effect of the latent heat of melting, thermal properties, and probe-beam size and offset on the shape of a PTD signal. Results are presented which demonstrate that the observed change in shape will not occur with planar heating, with or without phase transition. However, results derived for point-source heating show that it is possible for the maximum/minimum pair to occur when melting with a focused laser beam. The ratio of the sensible heat to the latent heat, and the ratio of the thermal diffusivities of the target and deflecting medium are the key factors which govern the deflection response. Computations for a general class of materials are given to show when the effect of latent heat can be observed at a surface. Results are also given which consider the probe-beam size and offset on the observations.

3.1 Introduction

With the advent of processes such as laser-sampling for chemical analysis, pulsed-laser annealing, laser-inscription of optical storage disks, and pulsed-laser deposition of thin-films [1,2], there has been a growing need to monitor laser-energy coupling to a solid during phase-change in real time. Yet whether the issue is detecting substrate damage thresholds in laser writing or measuring heat-flux transients in surface chemical analysis, monitoring changes during the process can be quite difficult. Detecting a solid to liquid phase transition by changes in reflectivity for a material such as aluminum which undergoes small changes in reflectivity (< 10%) at melt is troublesome at best; nearly impossible if the surface is coated. Similarly, detecting melt by measuring temperature changes at a surface can be challenging if the transients are fast (< 1 ms), and if the spatial resolution is small (< 1 mm). There are also basic issues concerning phase-change surface interactions which need study. Among these issues are the onset, location, and speed of propagation of a phase-front; the effect of material behavior due to anisotropy in structure and properties; and, the observation of the latent heat of melting at a surface. New monitoring methods can help answer these questions when it is difficult or impossible to do so with conventional techniques that use temperature, emissivity, and reflectivity.

The first purpose of this chapter is to demonstrate detecting the onset of melt at the surface of a solid in real time using a transient photothermal deflection (PTD) technique. The second purpose is to analyze when PTD can be used to detect solid to liquid phase transitions. While this is a novel use for this technique, PTD has been employed to monitor various surface phenomena, from analyzing specie concentrations near surfaces in electro-

chemistry [3] to measuring the velocity of components ejected from a surface during laser ablation [4]. Recently, PTD has been applied to detecting solid-solid phase transitions as a function of temperature [5-7], and for monitoring heat flux changes leaving a surface in real time, as described in chapter 2. What makes PTD attractive for monitoring events in real time is (i) the ability to detect fast transients ($\tau \approx 20$ ns) [8], (ii) high sensitivity to small changes in flux [8], and (iii) high spatial resolution. Depending on the curvature of the target, and the wavelength and focus of the probe-beam, the resolution can approach 10 μm. Also, unlike direct methods for measuring reflectivity, emissivity, or temperature, PTD gives a measure of gradients. If a fluid medium is heated by an adjacent surface, or has a flux of particles passing through it, gradients result in the temperature and density which create a gradient in the index of refraction of the medium, deflecting light that passes through it [9-12]. Since temperature gradients ∇T, can be directly related to heat flux $\mathbf{q}$, by a coefficient $\kappa(T)$, through Fourier's law ($\mathbf{q} = \kappa \nabla T$), PTD can be exploited to directly measure heat-flux leaving a surface. In practice, the temporal PTD signal can be quite complex due to variations in thermal and optical properties, evolution of vapor, chemical oxidation, geometry, etc., making it difficult to discern the physical processes occurring.

In this chapter, it is shown that phase transition at the surface of a laser-heated target can be detected by observing a local maximum/minimum pair in the temporal PTD signal. The major factors which determine when PTD can detect melt are the latent heat of melting, the thermal diffusivities of the target and the medium, the size of the laser

heating source, and the size and offset of the probe-beam. This chapter contains:

- A brief description of the experimental technique, apparatus, and procedure,
- Experimental observations showing the maximum/minimum pair in the PTD response for indium and tin targets which underwent phase-change, and a PTD response for indium which did not,
- Theoretical analysis of the deflection response by developing a physical model with solutions for (i) a planar heating source with melt, (ii) stepwise change in thermal properties without melt, and (iii) point-source heating with phase-change,
- The results for point-source melting showing the effect of latent heat of melting, thermal properties, probe-beam size and offset, comparisons of the integrated deflection with experimental observations, and an estimate of the onset of melt,
- A discussion of several factors that should affect the temporal PTD response for studying laser-induced phase-change phenomenon,
- Conclusions about the effect of latent heat of melting on the PTD response, and the class of materials for which the technique is applicable.

3.2 Experimental

The experimental work presented in this section uses the deflection of light to monitor the laser-material interactions in real time. In the conceptual diagram of the PTD technique shown in figure 3.1, a probe laser beam passes parallel to the surface of the target material in a optically

transmitting medium. The excitation laser, or pump-beam, strikes the target perpendicular to the surface, heating the solid target. The heat flux leaving the surface of the target changes the temperature and thereby the

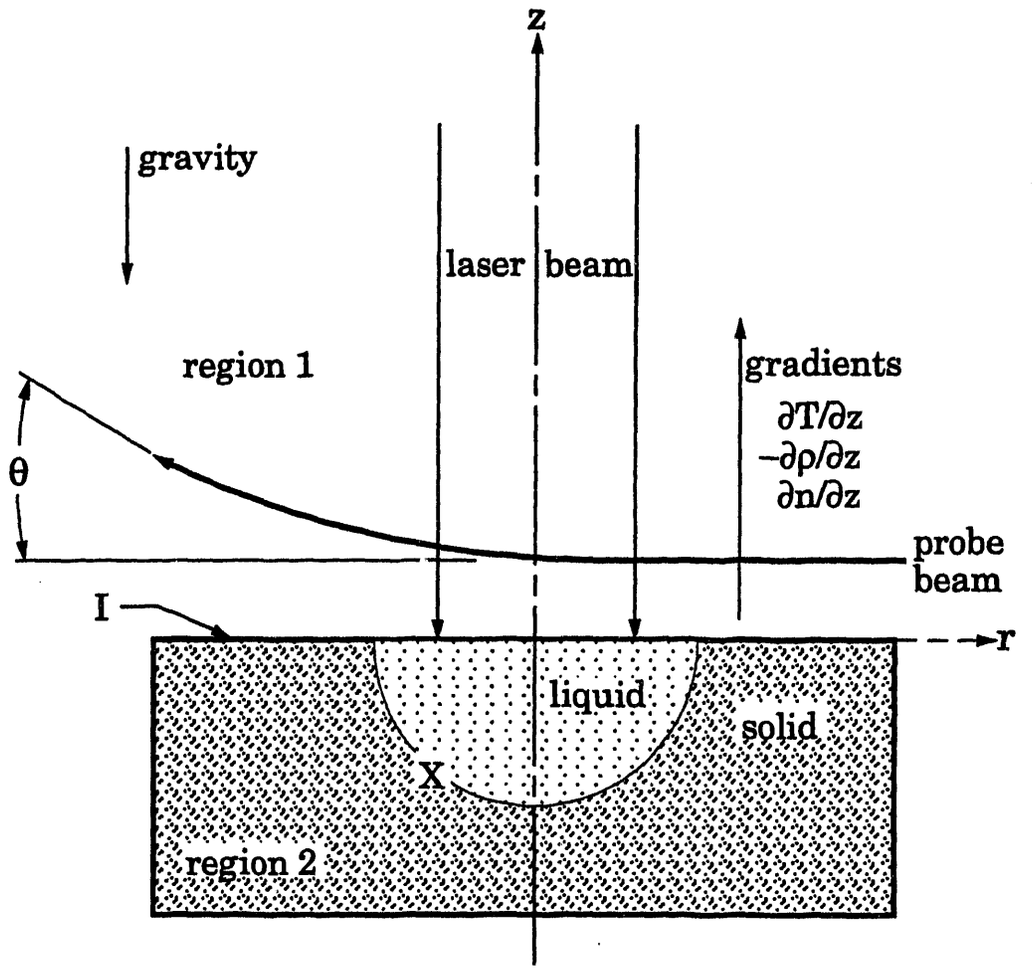

Figure 3.1 Physical model showing irradiation of interface, I, between regions 1 and 2. Region 1 may have solid and liquid phases separated by phase-front, X. Single ray of a probe-beam traversing across target deflects due to refractive index gradients.

density of the adjacent medium. The resulting density gradient creates a spatial gradient in the refractive index of the medium causing the probe-beam to bend. The magnitude that the probe-beam bends directly corresponds to the temperature gradient in the deflecting medium. The total deflection is an integration over the path of the beam as it traverses over the surface, as depicted in figure 3.1. The angle vector, $\boldsymbol{\theta}$, for a single ray undergoing small deflections [11,13] can be expressed as

$$\boldsymbol{\theta} = \int_{\text{path}} \frac{1}{n}\frac{\partial n}{\partial T}\, d\mathbf{s} \times \nabla T \tag{3.1}$$

where n is the index of refraction, $\mathbf{s}$ is the path of the ray, and T is the temperature of the deflecting medium. In these experiments, the angle, θ_c, that the centroid of a finite-sized beam deflects normal to the surface of the target is measured. For the case where the distance of the sensor from the target is large with respect to the path length, θ_c can be expressed as

$$\theta_c = \frac{\int_{\mathcal{A}} w(\mathbf{x})\,(\boldsymbol{\theta}\cdot\hat{\mathbf{n}})\, d\mathcal{A}}{\int_{\mathcal{A}} w(\mathbf{x})\, d\mathcal{A}} \tag{3.2}$$

where $w(\mathbf{x})$ is a spatial intensity weighting function, $\hat{\mathbf{n}}$ is the unit normal to the surface, and $\mathcal{A}$ is the cross-sectional area.

3.2.1 Apparatus

The apparatus used for the work is shown in figure 3.2. The solid target samples are heated in air and a He-Ne probe laser beam with a

632 nm wavelength passes above the surface. A Spectra-Physics 3000 series Nd:YAG continuous-wave laser with a 1064 nm wavelength modulated by a mechanical chopper is used as the heating source or pump-beam. The pump-beam is spatially Gaussian and is essentially temporally uniform during the heating period. The incident power heating the target is adjusted with a variable-reflectance attenuator and is measured after the chopper. The pump-beam had a $1/e^2$ beam-waist of approximately 160 μm. The probe-beam is aligned so that its centerline orthogonally intersects the centerline of the pump-beam, and has a beam-waist that measures approximately 200 μm. The deflection of the probe-beam was measured with a United Detector Technology model LSC-5D continuous single axis, dual cathode photodetector located 60 cm from the center of the target and was connected to a UDT model 301-DIV amplifier. The transient signal is captured with a Tektronix model 7854 digitizing oscilloscope. The targets are one cm cubes and can be considered thermally semi-infinite bodies for the pump-beam diameter and the pulsed heating period, t_p, used in the experiments.

The apparatus was designed and the target materials were chosen with the following issues in mind. The target surface was placed perpendicular to the direction of gravity in order to minimize the effect that the shape of the melt pool would have on the PTD signal. To minimize the convective and radiant heat losses from the surface, low melting temperature alloys, indium (429.76 °K) and tin (505.03 °K), were chosen. An added benefit of these materials is that their boiling temperatures are higher than 2000 °K. These high temperatures are not reached with the

laser power levels used in the experiments so the evolution of vapor is assumed negligible. An important consideration was to control the

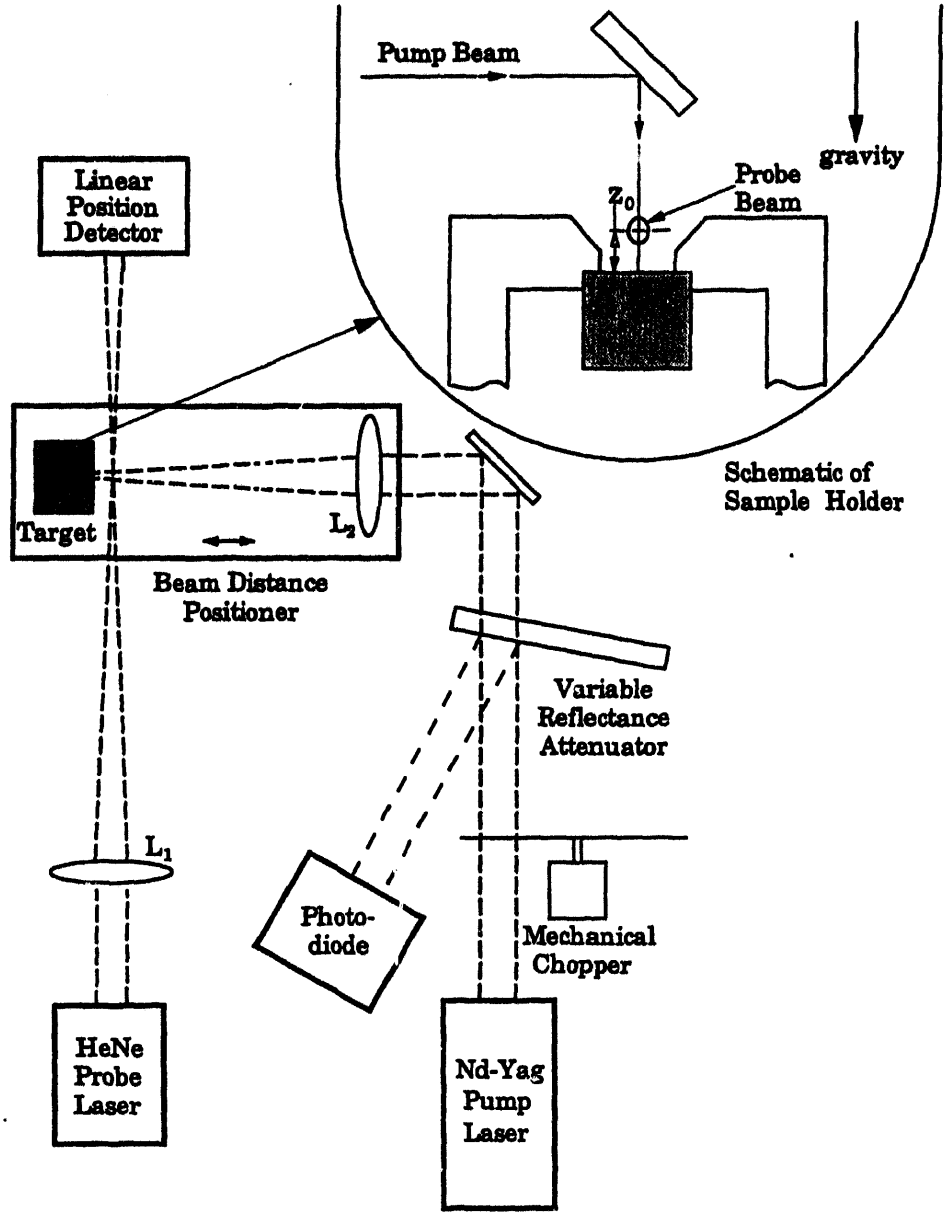

Figure 3.2 Schematic of experimental system. z_0 is the initial probe-beam centroid distance from horizontal target surface. Focal length of L_1 is 160 mm and L_2 is 120 mm.

reflectance variations of the target during heating and phase-change. To keep the absorbed laser energy constant, the surfaces of the materials were coated with approximately 10 nm thick films of stainless steel and carbon. These materials have small reflectance variations in the temperature range used, and their melting points are greater than 1000 °K over that of the target materials. In addition, these surface coatings suppressed oxidation of the target material during heating, and show if substrate damage can be detected beneath thin-films. These materials and surface treatments ensure that the changes observed in the PTD signal were due only to solid/liquid phase-change and not due to variations of reflectance with temperature or non-linear boundary conditions.

3.2.2 Observations

The temporal PTD responses for the first heating cycle for indium and tin targets are shown in figures 3.3(a & b), respectively. The incident power is 4.5 W and 4 W, t_p is 3.125 and 1.985 ms for the indium and tin, respectively. The distance, z_o, of the centroid of the probe-beam from the surface is approximately 100 μm. Phase-change was confirmed by microscopic examinations of the samples after irradiation. In these figures, the deflection initially increases at the start of the heating period, reaches a local maximum, decreases slightly to a local minimum, increases to a second local maximum, and then decreases monotonically before rapidly dropping off after the end of the laser pulse at time, $t = t_p$. To understand how these traces relate to laser melting, it is useful to consider a representative trace at a lower energy level where no phase-change was

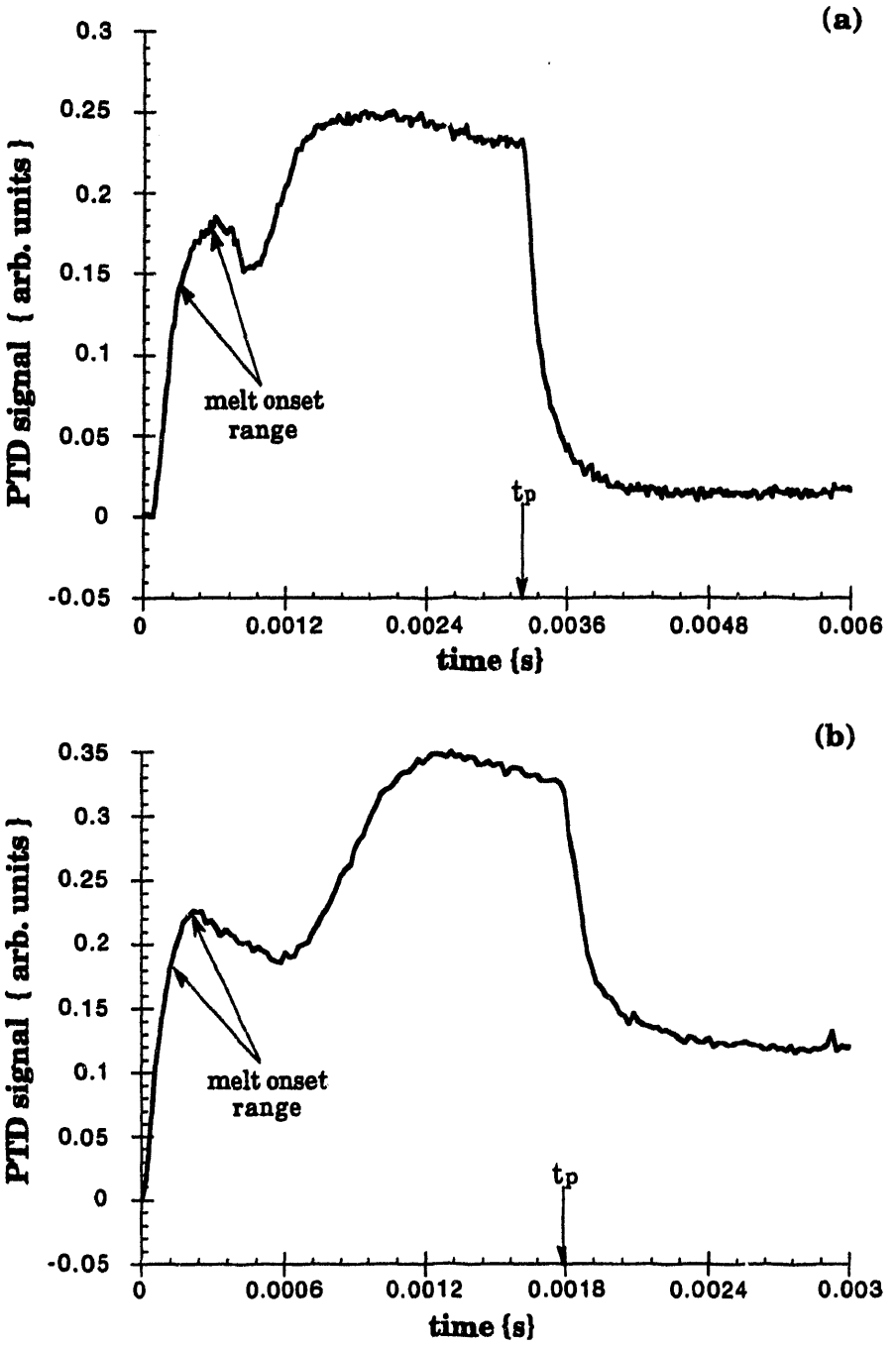

Figure 3.3 PTD response for indium (a) and tin (b) targets that show a local maximum and minimum pair after melt begins, followed by another maximum and decline. Average incident fluences are 2.25 (10^4) W/cm^2 (a) and 2.0 (10^4) W/cm^2 (b), and z_o is approximately 100 μm.

observed. In figure 3.4, the PTD signal for an indium target at a power level just below the melt threshold (3.75 W) shows that the trace increases monotonically to only one local maximum, and then decreases until t_p is reached. This trace is characteristic of simple heating without phase-change as described in chapter 2, in that no local minimum occurs during the heating cycle. The important observation for detecting the onset of melt with PTD is that the first local maximum/minimum pairs found in figures 3.3(a & b) occur only with phase-change, and not with simple heating.

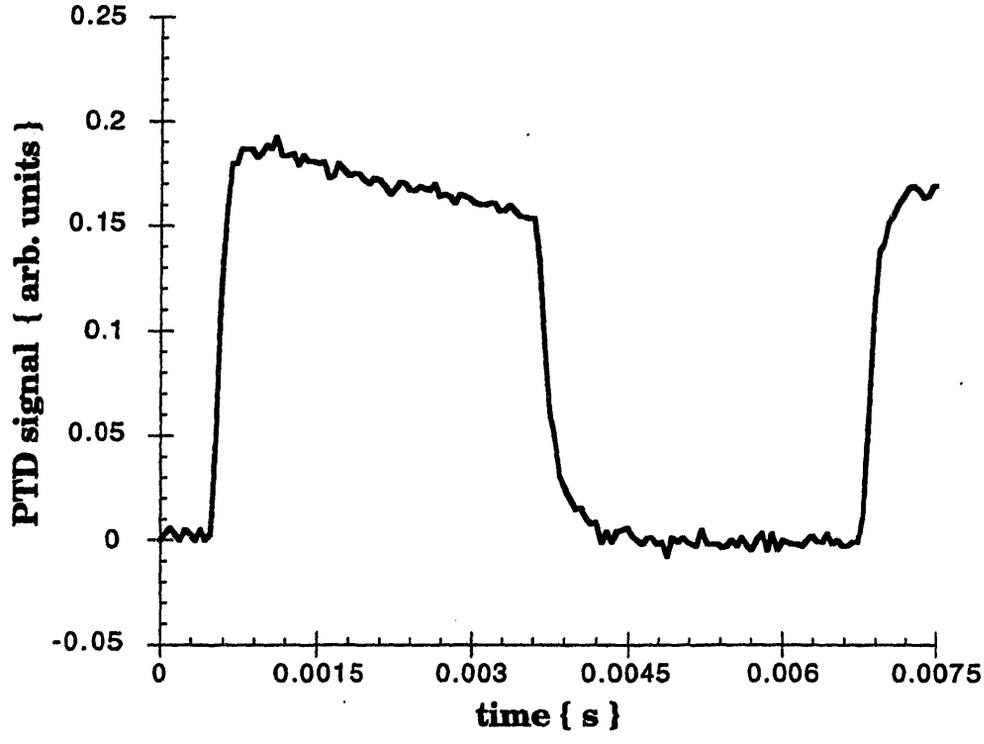

Figure 3.4 PTD response for indium target just below melt threshold. Only one local maximum and decline is seen. Average incident fluence is 1.85 (10^4) W/cm^2, and z_o is approximately 100 μm.

3.3 Theoretical Analysis

In this section the conditions for when a PTD signal signifies that melt has occurred is determined by analyzing the factors which cause a local maximum and minimum to occur in the PTD response. The key factors are (i) the latent heat of melting of the target material; (ii) the thermal properties of the material in the solid and liquid state, and those of the surrounding medium; (iii) the geometry, and the initial and boundary conditions of the target; and (iv) the size of the pump and probe-beam, and the probe-beam offset from the surface.

First the physical model used for analysis is presented, followed by planar and point-source solutions to illustrate how the geometry of the heat source, the latent heat of melting, and the thermal properties of the target and medium affect the PTD response. In the experiments, how the deflection of a probe-beam changes over time was recorded. The goal of this analysis is to find if a maximum or minimum can occur in the temporal deflection due to melt; that is, to see if the rate of change in the deflection response changes sign after melt has begun. For planar one-dimensional heating, closed-formed analytical solutions for the temperature gradient are examined to reveal that latent heat of melting and jumps in thermal properties at melt cannot by themselves explain the phenomenon. To model three-dimensional heating, a point-source solution is developed which explicitly considers the effect of latent heat and thermal properties on the defection response. The section closes with the method of solution for the deflection of the probe-beam for the point-source problem, and the restrictions that are imposed to ensure physically valid solutions.

3.3.1 Physical model

To construct a physical model for the deflection of the probe-beam in the gaseous medium, the temperature gradients arising from the laser energy transferred to the target and medium are found and are applied to equations (3.1) and (3.2). For the domain depicted in figure 3.1, the pump laser beam is assumed to pass through the deflecting medium and be completely absorbed at the interface, I. The laser energy is then transferred by diffusion into the deflecting medium (region 1) and the target (region 2). In region 2 there can be solid and liquid phases across the phase-front, X. The equations governing the heating of a material with a single phase-change temperature that is adjacent to a fluid medium, neglecting convective heat transfer, are

$$\nabla(k_j \nabla T) + q_j = \rho_j c_j \frac{\partial T}{\partial t} \qquad (j = 1,2)\,, \tag{3.3a}$$

where k_j is the thermal conductivity, ρ_j is the density, c_j is the heat capacity, and q_j is a volumetric heat source term. These equations are subject to the energy balance across the phase-front, X,

$$k_s \nabla T_s\big|_X - k_l \nabla T_l\big|_X = \rho L_m \frac{dX}{dt} \tag{3.3b}$$

for the temperature in the solid, T_s, and liquid, T_l. L_m is the latent heat of melting. The phase-front balance also satisfies the condition

$$T_s = T_l = T_m \quad @\ X\,, \tag{3.3c}$$

where T_m is the melting temperature. At the target/medium interface I, (3.3a) must also satisfy

$$T_1 = T_2 \quad @ \ I \tag{3.3d}$$

$$k_1 \nabla T_1\big|_I - k_2 \nabla T_2\big|_I = Q_{flux}, \tag{3.3e}$$

where Q_{flux} is the heat per unit area absorbed at the interface. Note that (3.3a) and (3.3b) form a non-linear set of equations for the target, which generally are complicated to solve. Therefore, solutions for planar and point sources in infinite media are considered in the following sections to determine which parameters are important for detecting the onset of melt with PTD.

3.3.2 Planar-source with phase-change

If the absorption of laser energy due to latent heat of melting was the only factor which caused the maximum/minimum pair in the experiments, then this change should occur during planar heating and melting of a target. To explicitly show the PTD response due to the latent heat of melting for a solid heated by a planar source, an isotropic half-space that is initially solid at its melting temperature is considered. The deflecting medium adjacent to the half-space is also initially at T_m. The medium is assumed to not participate radiatively and is not substantially convective, as with the experimental setup. When the target and surroundings are initially just below T_m, then the effects of arbitrary initial temperature distributions and thermal property changes upon melt are eliminated from the analysis.

When the thermal conductivity of the target material is much greater than the deflecting medium ($k_1 \gg k_2$), such as is the case for the metal targets and air medium in the experiments, the energy from the source transfers primarily into the target, which follows from (3.3e). The

governing equation for the deflecting medium, then, can be decoupled from the target by treating the target/medium interface as a variable temperature boundary condition. The solid target undergoing phase-change may be solved independent of the medium, simplifying the analysis. Near the onset of phase-change the temperatures are all close to T_m, so temperature dependence in the thermal properties is small and is neglected. For time $t > 0$, the surface at $z = 0$ receives a constant flux per unit area Q, which is completely absorbed at the surface. A series solution of equations (3.3a-c) obtained by Carslaw and Jaeger [14] for the planar half-space problem with the initial temperature at T_m shows that the temperature at the surface of the target T_{sur}, is

$$T_{sur} = T_m + \frac{Q^2 t}{k_l L_m \rho_l} - \frac{Q^4 t^2}{\alpha_l k_l L_m^3 \rho_l^3} + \ldots . \qquad (3.4)$$

where k_l is the thermal conductivity, α_l is the thermal diffusivity, and ρ_l is the density of the liquid target material. The temperature field in the deflecting medium may be found by the method of Green's function [14] as

$$\Theta(z,t) = \frac{T(z,t) - T_m}{T_{max} - T_m} \qquad (3.5)$$

$$= \frac{z}{2\sqrt{\pi\,\alpha_a}} \int_0^t \frac{T_{sur}(\tau) - T_m}{T_{max} - T_m} \frac{e^{-z^2/(4\alpha_a(t-\tau))}}{(t-\tau)^{3/2}} d\tau ,$$

where T_{max} is the highest temperature for which the analysis is valid, i.e. the boiling temperature or maximum temperature reached. Neglecting the higher order terms of (3.4) for small t gives the solution

$$\Theta(z,t) = \frac{t}{T_{max} - T_m}\left\{\left(1 + \frac{z^2}{2\alpha_a t}\right)\text{erfc}\ \frac{z}{2\sqrt{\alpha_a t}} - \frac{z}{\sqrt{\pi\alpha_a t}}\, e^{-z^2/(4\alpha_a t)}\right\}, \tag{3.6}$$

and the derivative of Θ with respect to z and t is

$$\frac{\partial}{\partial t}\left(\frac{\partial \Theta}{\partial z}\right) = \frac{-\sqrt{\pi\alpha_a t}}{T_{max} - T_m}\, e^{-z^2/(4\alpha_a t)}. \tag{3.7}$$

By setting (3.7) equal to zero, only at $t = 0$ or $z \rightarrow \infty$ does a maximum or minimum in the temperature gradient occur. A change in direction of the flux does not occur after T_m. Therefore, a maximum or minimum can not occur in a PTD signal due to latent heat alone when heating an isotropic crystalline semi-infinite solid with a planar source.

3.3.3 Planar-source considering jump in thermal properties at melt

The effect on the PTD response of the change in thermal properties due to melt and initial conditions which differ from T_m is now considered. For planar heating of a target which does not undergo phase-change, the heat flux direction remains constant in time and a local maximum in the PTD signal cannot occur, if both domains have the same initial temperature and there are not any discontinuous changes over time in the thermal properties. This result will be demonstrated analytically for the case of two joined half-spaces with different thermal properties being heated at their interface. Yet thermal properties for many materials exhibit discontinuous changes between the solid and liquid regions [15]. As seen in figure 3.5 for indium and tin versus air, the ratio of their thermal diffusivities decreases stepwise at T_m. Initially, the diffusivity of indium is greater than that of air, so that heat diffuses more rapidly into the target. By the melting

temperature, however, the diffusivities are approximately the same and the heat diffuses about equally. Immediately after phase-change, the diffusivity of indium drops to less than half that of air so that the heat flux at the surface is now diffusing more rapidly into the air. The plot for air and tin show similar results. Since the deflection of the probe-beam is related to the temperature gradient in the air as given in (3.1), and thus to the heat flux leaving the surface, the PTD signal reflects the changes in the thermal properties which occur during phase-change. Therefore, it is possible that the stepwise change in thermal properties at melt could create a maximum or minimum in the deflection response.

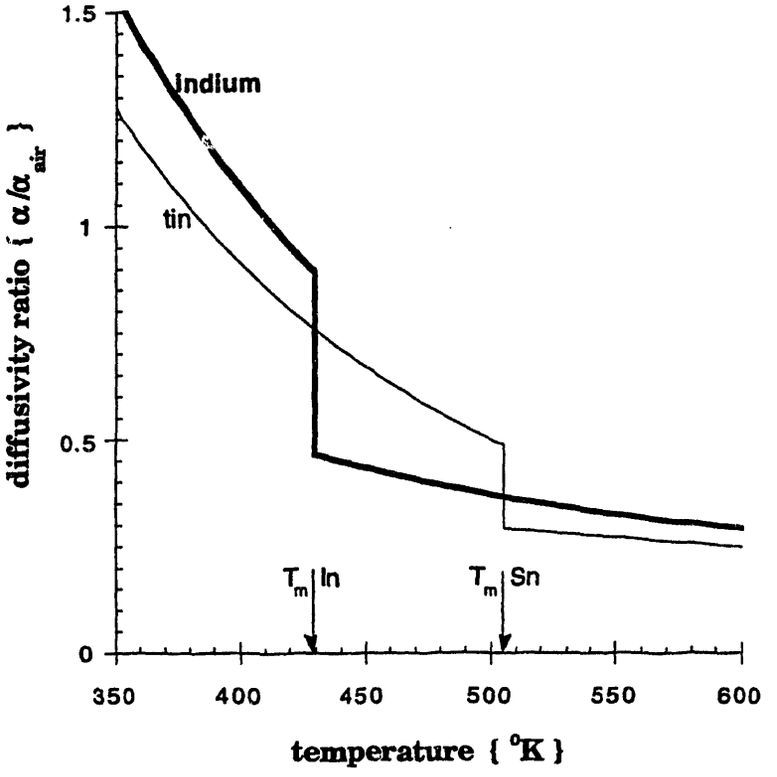

Figure 3.5 Thermal diffusivity ratios of indium and tin versus air. The jump in thermal properties is shown at the melt temperature, T_m.

Since the latent heat of melting does not cause a local maximum or minimum in the PTD signal for planar heating of a target, a target that has temperature dependent thermal properties which change stepwise in time is now considered. The solution in the deflecting medium, a, of (3.3a,d,e) for two joined half-spaces that each have constant thermal properties with Q supplied to the interface at $z = 0$ is found to be [14]

$$\Theta_a(z,t) = \frac{T_a(z,t) - T_i}{T_m - T_i}$$

$$= \frac{\bar{Q}}{k_t(\alpha_a/\alpha_t)^{1/2} + k_a}\left(\frac{2\sqrt{\alpha_a t}}{\sqrt{\pi}}\, e^{-z^2/(4\alpha_a t)} - z\ \mathrm{erfc}\,\frac{z}{2\sqrt{\alpha_a t}}\right) \tag{3.8}$$

where $\bar{Q} = Q/(T_m - T_i)$. To account for a stepwise change of k_1 in (3.3e) when the temperature exceeds T_m, the time t_m when $\Theta_t = 1$ at $z = 0$ is

$$t_m = \frac{\pi\,(k_t\,\alpha_a{}^{1/2} + k_a\alpha_t{}^{1/2})^2}{4\,\bar{Q}^2\,\alpha_a\,\alpha_t}. \tag{3.9}$$

Equation (3.9) predicts that the time to the onset of melt is inversely proportional to the power squared. For time $t \geq t_m$, a solution is defined such that

$$\Phi_a(z,t) = \Theta'_a(z,t) - \Theta_a(z,t_m)\,, \tag{3.10a}$$

where $\Phi_a(z,t_m) = 0$ and

$$\Phi_a(z,t \geq t_m) = \frac{\bar{Q}}{k'_t\,(\alpha_a/\alpha'_t)^{1/2} + k_a} \times$$

$$\left(\frac{2\sqrt{\alpha_a\,(t-t_m)}}{\sqrt{\pi}}\, e^{-z^2/4\alpha_a(t\,-\,t_m)} - z\ \mathrm{erfc}\,\frac{z}{2\sqrt{\alpha_a\,(t-t_m)}}\right). \tag{3.10b}$$

The prime (′) denotes the stepwise change in thermal properties of the target. The temperature gradient in the deflecting medium from (3.10a&b) is

$$\frac{\partial \Theta_a'}{\partial z}(z,t) = \frac{-\bar{Q}}{k_t'(\alpha_a/\alpha_t')^{1/2} + k_a} \operatorname{erfc} \frac{z}{2\sqrt{\alpha_a (t - t_m)}} - \frac{\bar{Q}}{k_t(\alpha_a/\alpha_t)^{1/2} + k_a} \operatorname{erfc} \frac{z}{2\sqrt{\alpha_a t_m}}, \tag{3.11}$$

and the time derivative of (3.11) for $t \geq t_m$ is

$$\frac{\partial}{\partial t}\left(\frac{\partial \Theta_a'}{\partial z}\right)(z,t) = \frac{-\bar{Q}}{k_t'(\alpha_a/\alpha_t')^{1/2} + k_a} \frac{z}{2\sqrt{\pi\alpha_a}(t - t_m)} e^{-z^2/(4\alpha_a(t - t_m))}. \tag{3.12}$$

Equation (3.12) shows that a local maximum with time is not present for $t \geq t_m$. The time derivative in (3.12) also represents the case when there is no discontinuity in thermal properties, seen by setting $t_m = 0$ and removing the prime notation. Thus, a maximum does not occur before phase-change. Furthermore, the temperature gradient at $t = t_m^{(-)}$ is the same as at $t = t_m^{(+)}$ as shown by (3.11), and by differentiating (3.10b) and setting $t = t_m$. Since (3.12) is zero and is a minimum at $t = t_m$ and the gradients are equal, a local maximum will not occur for the case when the initial temperature differs from T_m. This analysis shows that the discontinuity in thermal properties of the material due to phase-change can certainly change the slope of the PTD signal after melt. Since a change in the sign of the slope does not occur in the case of planar heating, I must conclude that an observation of a maximum/minimum pair in the PTD response is not strictly a result of material properties.

3.3.4 Point-source with phase change

In this section, a point-source solution is developed for the temperature field in the deflecting medium with the target undergoing phase-change. Heating a target with a small source, as is often the case with lasers, can produce a three-dimensional temperature field in the target and the surrounding medium. With a three-dimensional temperature field that is changing in time, the direction of the flux vector at any point in the deflecting medium changes in time, and the integrated effect of these changes is reflected in the temporal shape of the PTD signal. Only in the special case of equal constant diffusivities in the two regions, no phase-change, and a point-source at the interface will spherical symmetry be achieved and the heat flux direction remains constant in time. This symmetry can be demonstrated in a manner similar to the planar case. Unlike the planar case, however, differing thermal properties between the regions can produce a local maximum in the deflection response over time, as described in chapter 2. Since point-source heating allows a local maximum to be observed due to changing heat-flux directions, the conditions in which phase-change modifies the heat-flux to cause the observed maximum/minimum pair to occur will be analyzed.

As with planar heating, the effect of latent heat of melting on the temperature field in the deflecting medium is explicitly considered by considering the case when the initial temperature is T_m. As before, the thermal conductivity of the target material is assumed to be much greater than the deflecting medium ($k_1 \gg k_2$), allowing the governing equations in (3.3a) to be decoupled between regions by treating the target/medium interface as a variable temperature boundary condition. The solution for

the target in spherical coordinates for an infinite solid initially at T_m is now developed. The origin at r = 0 receives a constant supply of heat, Q, when time t > 0. The phase-front is assumed to move slowly with respect to the thermally affected zone, and the ratio of the sensible heat to the latent heat, defined as the Stephan number, is assumed to be less than one. Equation (3.3a) for this case is considered quasi-static and the explicit time dependence is neglected [16]. The steady-state energy equation in spherical coordinates for constant properties is

$$\frac{d}{dr}\left(r^2 \frac{dT}{dr}\right) = 0 , \tag{3.13a}$$

where

$$T(r=X) = T_m . \tag{3.13b}$$

The heat supply at r = 0 must be balanced by $Q = -k_l A\,(dT/dr)$ at r = X, which gives the second boundary condition

$$\left.\frac{dT}{dr}\right|_{r=X} = \frac{-Q}{2\pi k_l X^2} . \tag{3.13c}$$

Solving the general solution to (3.13a), T(r) = A/r + B, and using (3.13b,c) gives

$$T(r) = \frac{Q}{2\pi k_l}\left(\frac{1}{r} - \frac{1}{X}\right) + T_m \quad 0 < r \le X$$

$$T(r) = T_m \quad r > X , \tag{3.14}$$

which is singular at r = 0, as expected for a point-source. Applying the energy balance across the front (3.3b), noting that $dT_s/dr = 0$ at r = X, and using (3.13c) yields the differential equation in time for X

$$X^2 \frac{dX}{dt} - \frac{Q}{2\pi\rho_l L_m} = 0 \tag{3.15}$$

which integrated over the melt region up to the time t gives

$$\int_0^X \xi^2 \, d\xi = \int_0^t \frac{Q}{2\pi\rho_l L_m} d\tau \tag{3.16}$$

and

$$X(t) = \sqrt[3]{\frac{3Qt}{2\pi\rho_l L_m}} \, . \tag{3.17}$$

Therefore, the temperature of the target at the boundary of the deflecting medium in radial coordinates is

$$\begin{aligned} \Theta_t(r,t) &= \frac{T(r,z=0,t) - T_m}{T_{max} - T_m} \\ &= \frac{Q}{2\pi k_l (T_{max} - T_m)} \left(\frac{1}{r} - \sqrt[3]{\frac{2\pi\rho_l L_m}{3Qt}} \right) \end{aligned} \tag{3.18}$$

which is singular at $r = 0$ and $t = 0$. Non-dimensionalizing the time by the heating period, $\bar{t} = t/t_p$, and the distance by the phase-front position at a characteristic time, $\bar{r} = r/X_c$, and using (3.14), (3.17), and (3.18) gives

$$\Theta_t(\bar{r},\bar{t}) = \frac{1}{\bar{r}} - \frac{1}{(\bar{t_p}\,\bar{t})^{1/3}} \quad \text{for} \quad \bar{r} \le (\bar{t_p}\,\bar{t})^{1/3}) \tag{3.19a}$$

subject to the physical constraint that $\Theta_t \le 1$, and

$$\Theta_t(\bar{r},\bar{t}) = 0 \quad \text{for} \quad \bar{r} > (\bar{t_p}\,\bar{t})^{1/3}) \, , \tag{3.19b}$$

where $\bar{t_p} = t_p/t_c$. The characteristic time for the melt front to move from $t = 0$ to $t = t_c$ is defined as

$$t_c = \left(\frac{Q}{2\pi}\right)^2 \frac{1/3\ \rho_l L_m}{k_l^3 (T_{max} - T_m)^3} = \frac{1}{12}\left(\frac{\bar{Q}}{\pi k_l}\right)^2 \frac{1}{Ste\ \alpha_l}, \qquad (3.20)$$

where $Ste = c_p \Delta T / L_m$ is the Stephan number, and $\bar{Q} = Q/(T_{max} - T_m)$. This characteristic time gives a measure of the time scale for the laser heat to diffuse out over the whole domain versus the diffusion of the sensible heat over the latent heat near the phase-front. As $Ste\ \alpha_l$ gets smaller for a fixed power and conductivity, the phase-front will take longer to move a fixed distance, because more energy in the domain goes into the changing phase than in raising the sensible heat.

Choosing the same method of non-dimensionalizing the energy equation (3.3a) with constant properties and no volumetric heating gives, in coordinate free form,

$$\bar{\nabla}^2 \Theta_a(\bar{t}) = \frac{X_c^2}{\alpha_a \bar{t}_p t_c} \frac{\partial \Theta_a}{\partial \bar{t}}, \qquad (3.21a)$$

and using (3.17) and (3.20) yields

$$\bar{\nabla}^2 \Theta_a(\bar{t}) = \frac{3}{\bar{t}_p} Ste \frac{\alpha_l}{\alpha_a} \frac{\partial \Theta_a}{\partial \bar{t}}. \qquad (3.21b)$$

Equation (3.21b) reveals the non-dimensional group, $Ste\ \alpha_l/\alpha_a$, governing the transient response of the medium due to phase-change in the target. Two points are of note. When $Ste\ \alpha_l/\alpha_a$ is small, the system behaves close to steady-state heating. Also $\bar{t}_p$ is linear in pulse length t_p, and t_c is a function of the power and material properties, so increasing t_p or decreasing Q reduces the dependence on time for a given material. Since the onset of melt is the transient event we wish to observe, the power and

pulse length can be adjusted for a given material. The implications of Ste α_l/α_a with respect to the PTD signal is discussed in §3.4.

3.3.5 Solution method

This sections considers the restrictions placed on the materials and heating conditions to ensure that the solutions of the point-source model of §3.3.4 are physically valid, and presents the method of solution for the deflections of the probe-beam presented in the results.

A formal analytical solution can be found for equation (3.21b), subject to the temperature boundary condition given by (3.19a&b) at $z = 0$, by the method of Green's functions. For a semi-infinite domain initially at zero, which is heated on the boundary by a transient, radially symmetric temperature field with no angular dependence, the solution obtained is

$$\Theta_a(\bar{r},\bar{z},\bar{t}) = \left(\mathrm{Ste}\,\frac{\alpha_l}{\alpha_a}\right)^{3/2} \frac{\bar{z}}{8(\pi\bar{t}_p)^{3/2}} \int_0^{\bar{t}} \frac{1}{(\bar{t}-\tau)^{5/2}} \times$$

$$\left\{ \int_0^{\rho=(\bar{t}_p\,\tau)^{1/3}} \left(1 - \frac{\rho}{(\bar{t}_p\,\tau)^{1/3}}\right) I_o\left(\mathrm{Ste}\,\frac{\alpha_l}{\alpha_a}\,\frac{\bar{r}\,\rho}{2\bar{t}_p(\bar{t}-\tau)}\right) \exp\left(-\mathrm{Ste}\,\frac{\alpha_l}{\alpha_a}\,\frac{\rho^2+\bar{r}^2+\bar{z}^2}{4\bar{t}_p(\bar{t}-\tau)}\right) d\rho \right\} d\tau \qquad (3.22)$$

where I_o is the modified Bessel function of the first kind of zero order. However, the integration of (3.22) proves to be very difficult, both analytically and numerically, even in an approximate sense [17]. It can be shown, though, using asymptotic expansions of the integrand that (3.22) is singular at $\bar{r} = 0$. The distance that the melt front moves X_c, over the characteristic time t_c, must be greater than the boiling temperature region

given by the singularity. From (3.17), (3.19a) and (3.20), Xc is restricted such that

$$X_c > \frac{Q}{4\pi k_l (T_{boil} - T_m)} \cdot \tag{3.23}$$

Furthermore, when Ste α_l/α_a is large with respect to $\bar{t}_p$ the integrand becomes vanishingly small for times near the onset of melt. Therefore, when X_c greatly exceeds that of the thermal diffusion length in the medium, $\delta_{th}{}^a$, changes to the temperature field due to melt are small. The velocity of the phase-front bounds the solutions to those where X_c satisfies (3.23) and $X_c \lesssim \delta_{th}{}^a$, as well as Ste < 1 from the original assumption made in (3.13a).

A numerical model was constructed to solve equation (3.21b) subject to the boundary condition (3.19a&b) to predict the transient temperature gradients in the deflecting medium above the target surface. The method uses a radially symmetric two-dimensional finite difference equation in cylindrical coordinates [18] for the temperature grid function *V* at time step *k* for r > 0 where

$$V_{i,j}^{(k+1)} = V_{i,j} + \frac{1}{3}\frac{\Delta\bar{t}}{\bar{t}_p}\frac{1}{\text{Ste}\,\alpha_l/\alpha_a} \times$$

$$\left\{\frac{V_{i+1,j} - V_{i,j}}{\Delta\bar{z}^2} + \frac{V_{i-1,j} - V_{i,j}}{\Delta\bar{z}^2} + \left(1 + \frac{\Delta\bar{r}}{2\bar{r}}\right)\frac{V_{i,j+1} - V_{i,j}}{\Delta\bar{r}^2} + \left(1 - \frac{\Delta\bar{r}}{2\bar{r}}\right)\frac{V_{i,j-1} - V_{i,j}}{\Delta\bar{r}^2}\right\} \tag{3.24}$$

subject to

$$V_{0,j} = \frac{1}{\bar{r}_j} - \frac{1}{(\bar{t}_p - \bar{t})^{1/3}} \quad ; \quad V_{0,j} \le 1$$

and (3.25)

$$V_{0,j} = 1 \quad \text{if} \quad V_{0,j} > 1$$

to ensure that the solution is physically bounded. The outer boundaries are at infinity so the domain size (m,n) is set to 3 δ_{th} in all directions to approximate a thermally infinite domain, and it is assumed that

$$V_{i,j} = 0 \quad @ \quad i = m \text{ and/or } j = n \quad . \tag{3.26}$$

Note that V is only dependent on $\bar{t}_p$ and Ste α_l/α_a and may be solved for a general class of problems, provided that Ste < 1 and the restrictions on X_c given above are met.

The normal deflection of a single ray of the probe-beam is found by using a trapezoidal integration of (3.1) for each node along the path that the ray traverses, which for the grid function in cylindrical coordinates yields

$$\Delta\theta_j \approx -\frac{1}{n_0}\frac{dn}{dT_j}\left(\frac{\partial V_{i,j}}{\partial \bar{z}} + \frac{\partial V_{i,j+1}}{\partial \bar{z}}\right)\frac{\Delta\bar{r}}{2} \quad . \tag{3.27}$$

The change in the refractive index with temperature is dependent on the medium, which is assumed to be a fluid that obeys the Lorentz-Lorenz relation [19,20]. For an ideal gas, the equation simplifies to

$$\frac{dn}{dT_j} \approx \frac{-(n_0 - 1)}{T_j} \tag{3.28}$$

where the average dimensional temperature {K} between the surrounding nodes for T_j is used. The integration of (3.1), however, depends on the path and on the solution of (3.24) for the current position of the ray, $z_{ray}(\bar{r}, \bar{t})$, as it deflects from its initial distance from the surface, $\bar{z}_0$. The method of solution employed was to first solve (3.24) over the domain, and

then interpolated the solution near $z_{ray}(r_j,t_k)$ with a second order polynomial to approximate $\partial V/\partial z$ at $z = z_{ray}$. Then $\Delta\theta_j$ is calculated from (3.27) and (3.28), and summed over j to find θ_j. With the angle known at each point, the i^{th} ray position is found by

$$z_{ray}(\bar{r}_{j+1},t_k) = z_{ray}(\bar{r}_j,t_k) + dz_{ray}(\bar{r}_j,t_k) \approx \bar{z}_0{}^i + \sum_{q=1}^{j}\Delta\theta_q\,\Delta\bar{r} \quad . \qquad (3.29)$$

The path of the integration starts at the outer boundary of the target, traverses to the center and back to the outer edge. Although the symmetry of the problem is exploited for the calculation of V, the path back is not identical to the inward path since z_{ray} is continually varying. Denoting the polynomially-approximated grid-function differentials by $\partial V^p/\partial z$, the deflection of the i^{th} ray is

$$\theta^i(t_k) = -\sum_{j=n}^{2,-1} 2\,\frac{n_0-1}{T_j+T_{j-1}}\left(\left.\frac{\partial V^p{}_j}{\partial z}\right|_{z=z_{ray}(\bar{r}_j)} + \left.\frac{\partial V^p{}_{j-1}}{\partial z}\right|_{z=z_{ray}(\bar{r}_j)}\right)\frac{\Delta\bar{r}}{2}$$
$$- \sum_{j=1}^{n-1} 2\,\frac{n_0-1}{T_j+T_{j+1}}\left(\left.\frac{\partial V^p{}_j}{\partial z}\right|_{z=z_{ray}(\bar{r}_j)} + \left.\frac{\partial V^p{}_{j+1}}{\partial z}\right|_{z=z_{ray}(\bar{r}_j)}\right)\frac{\Delta\bar{r}}{2} \quad . \qquad (3.30)$$

It is assumed that $z = z_{ray}(\bar{r}_j)$ for $\bar{r}_j$ and $\bar{r}_{j\pm1}$ since (3.1) is derived for small deflections. To integrate over the thickness of the beam, the intensity weighting function is taken as unity, and the centroid is calculated directly from (3.2) by summing ray deflections for a given diameter and initial $\bar{z}_0$. The Fortran computer code used for the calculations is contained in Appendix I.

3.4 Results and Discussion

How the latent heat of melting, L_m, effects the PTD signal is of primary interest if the effect of L_m is to be observed in real time at a surface. But whether or not the effect of L_m can be observed by PTD is closely tied to other factors. From the results found in §3.3.2, L_m does not have any effect on producing a local maximum/minimum pair in the PTD response for a target with a flat surface heated by a planar source. Clearly the geometry of the temperature field is a major factor for being able to detect phase-change at a surface with PTD. Physically, the effect of geometry can be explained as follows. With a planar source heating a flat surface, the net heat that diffuses into the target raises its sensible heat. At the melt temperature, any additional energy changes the phase of the solid at the surface. A planar melt front then moves away from the surface, and the net heat again raises the temperature at the surface. The result is that at the onset of melt, the surface temperature is at the melting temperature for only an instant. The effect of L_m on the heat-flux entering the medium above the surface would also be momentary, since a volume of material is not absorbing heat at a constant temperature. The net magnitude of the flux leaving the surface could change due to phase-change, but a change in the direction of the flux in time is not expected. However, if the source is small, a phase-front can propagate along the surface, and the heat absorbed due to L_m can have an effect, depending on the thermal properties as discussed below. Changes in the thermal properties, from the results in §3.3.3, are not be enough to cause a maximum/minimum pair if the heating source were planar. The abrupt changes in thermal properties which can occur at melt may only a change the slope of the deflection response.

Since the laser beam is small with respect to the target (160 μm vs. 1 cm) and the samples are thermally infinite, the point-source solution is examined for the parameters governing the observed PTD response for melting. The non-dimensionalization of the energy equation subject to a temperature boundary condition undergoing melt gave Ste α_l/α_a in (3.21b). This group includes both the ratio of the sensible heat versus the latent heat of melting of the target, as well as the ratio of the thermal diffusivity between the target and the medium. For the case when the sensible heat is much greater than the latent heat, the system would behave like one without phase-change, and the ratio of the diffusivities would dominate, similar to the case shown in figure 3.4. In figure 3.6, the angular deflection of a ray at the surface is plotted versus non-dimensional time (t/t_p) and Ste α_l/α_a, where Ste < 1. Reflection and absorption of the probe-beam at the surface are ignored for clarity. When Ste α_l/α_a is 10, the deflection increases to a local maximum and then decreases monotonically. This is similar to the case where there is no phase-change but the diffusivity ratio differs from one. As Ste α_l/α_a decreases below 4, a negative deflection occurs after a small lag in time. A minimum is reached and the deflection becomes positive again at later times. When Ste α_l/α_a drops below 1.5, the angle remains negative for the entire pulse. For the smallest Ste α_l/α_a, the negative deflection begins almost immediately after the onset of heating, and reaches a large pronounced minimum. While this graph does not represent true deflections, it demonstrates the importance of Ste α_l/α_a for determining if a local minimum can occur in the PTD response for a particular material, medium, and temperature range.

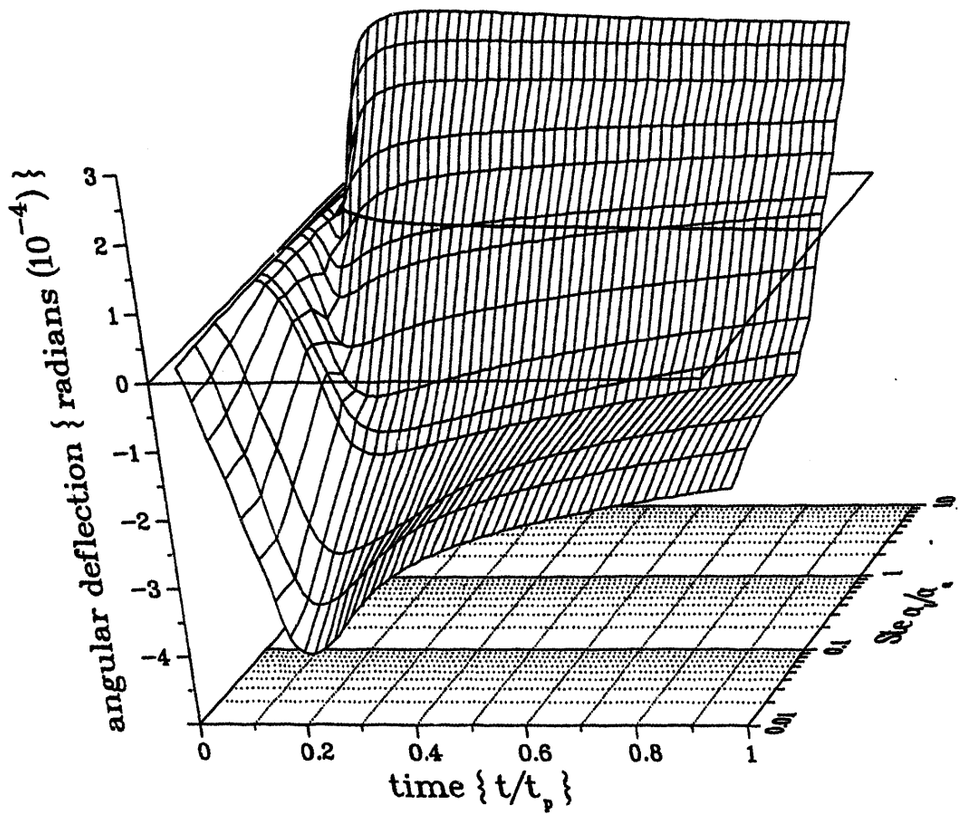

Figure 3.6 Theoretical angular deflection of a ray at the interface. Zero plane shows the times, t, in the heating period, t_p, that the deflection becomes positive over three decades of Ste α_l/α_a ($\bar{t_p} \cdot t_c = 1$ ms).

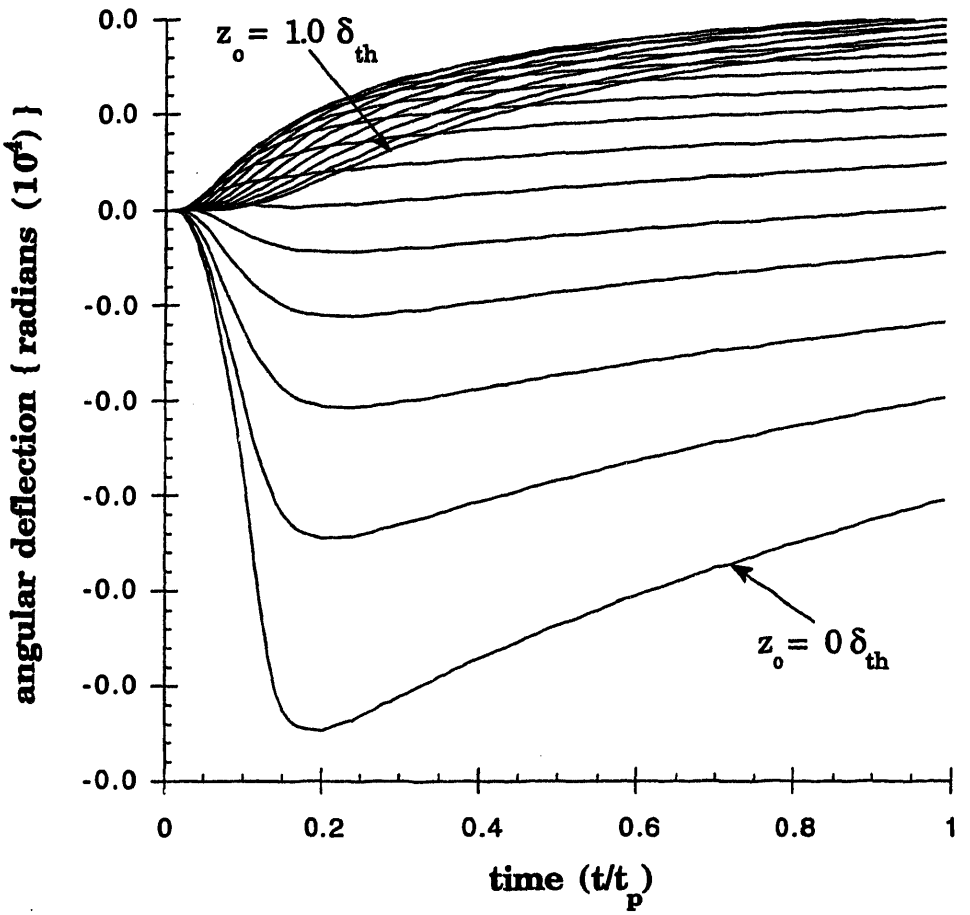

Figure 3.7 Deflection of a ray with the initial distance, z_o, varying from 0 to 1 thermal diffusion lengths in air. Target is simulated for indium with Ste = 0.42, α_l/α_a = 0.46, and with an average incident fluence of 2.25 (10^4) W/cm^2.

For the indium target, a maximum/minimum pair was experimentally observed signifying the onset of melt. The Stephan number for this experiment was determined to be about 0.42 for a temperature rise of 100 °K above the melting temperature. The incident power density was 2.5 (10^4) W/cm^2. Figure 3.7 shows the calculated deflections of rays with

initial distances z_i ranging from 0 to a thermal diffusion length in the medium, $\delta_{th}{}^a$. The closest rays would exhibit a large negative angle, if they were not reflected or absorbed by the surface. As the offset increases to $\delta_{th}{}^a$, the ray deflections experience only positive deflections and also lag due to the time for the heat to diffuse. The integrated deflection is shown in figure 3.8 for the indium and tin targets for a 200 μm diameter probe-beam with z_o = 100 μm, which was the experimental probe-beam size and offset. For both cases, the deflection undergoes a small rise to a maximum, a descent to a minimum, and then a monotonic increase to the end of the heating period. These curves show that a local maximum/minimum pair can occur in the PTD signal and that the observed pair corresponds with the onset of melt in the analysis.

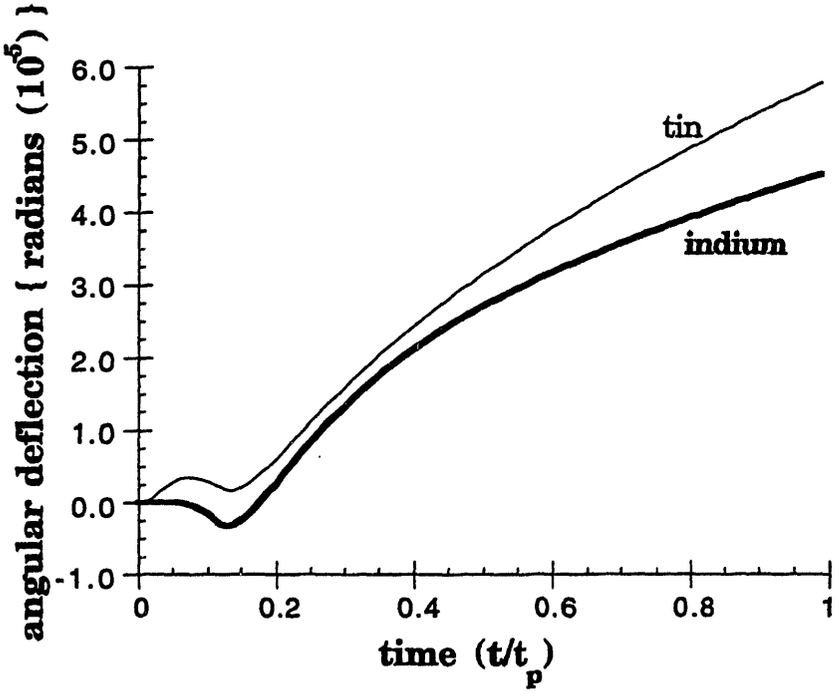

Figure 3.8 Integrated angular deflection for a finite probe-beam size of 200 μm and z_o of 100 μm, over tin and indium targets. Average incident fluence is 2.25 (10^4) W/cm^2.

Even if the value of Ste α_l/α_a predicts that a minimum in the deflection response is possible, the existence of a minimum/maximum pair depends on the probe-beam radius and initial distance z_o. When Ste α_l/α_a is one, figure 3.9(a) shows the effect of increasing the radius of a probe-beam whose closest ray is grazing the surface. When the radius is small with respect to the thermal diffusion length of the medium, the beam shows a large negative angular deflection. As the beam radius increases to $\delta_{th}{}^a$, the positive deflections which occur farther from the surface integrate out the negative deflections near the surface. Figure 3.9(b) demonstrates the effect of increasing the offset distance from the surface while keeping the probe-beam radius constant. The deflection exhibits a local minimum for $z_o = 0.15\ \delta_{th}{}^a$, and has no local minimum or maximum as z_o approaches $0.5\ \delta_{th}{}^a$. Therefore, in order to observe a maximum/minimum pair associated with the onset of melt the probe-beam must be small and close to the surface, with respect to the medium's δ_{th}.

The source of the negative deflections predicted by the analysis and the effect of L_m on the observed PTD response are closely related. As discussed in §3.4, when both the target and medium have the same diffusivity, point-source heating at the interface cannot produce a local minimum or maximum in the PTD response if there is no phase-change. Yet reviewing figure 3.9(a) for the case when $\alpha_l/\alpha_a = 1$ shows that changes in direction of the PTD signal are possible for a small probe-beam grazing the surface. Figure 3.6 shows that a local minimum is possible for this case whenever the Stephan number is less than one, for a particular material and temperature range. Since Ste gives the ratio of the sensible heat over the latent heat of melting, clearly the latent heat affects the PTD signal. From

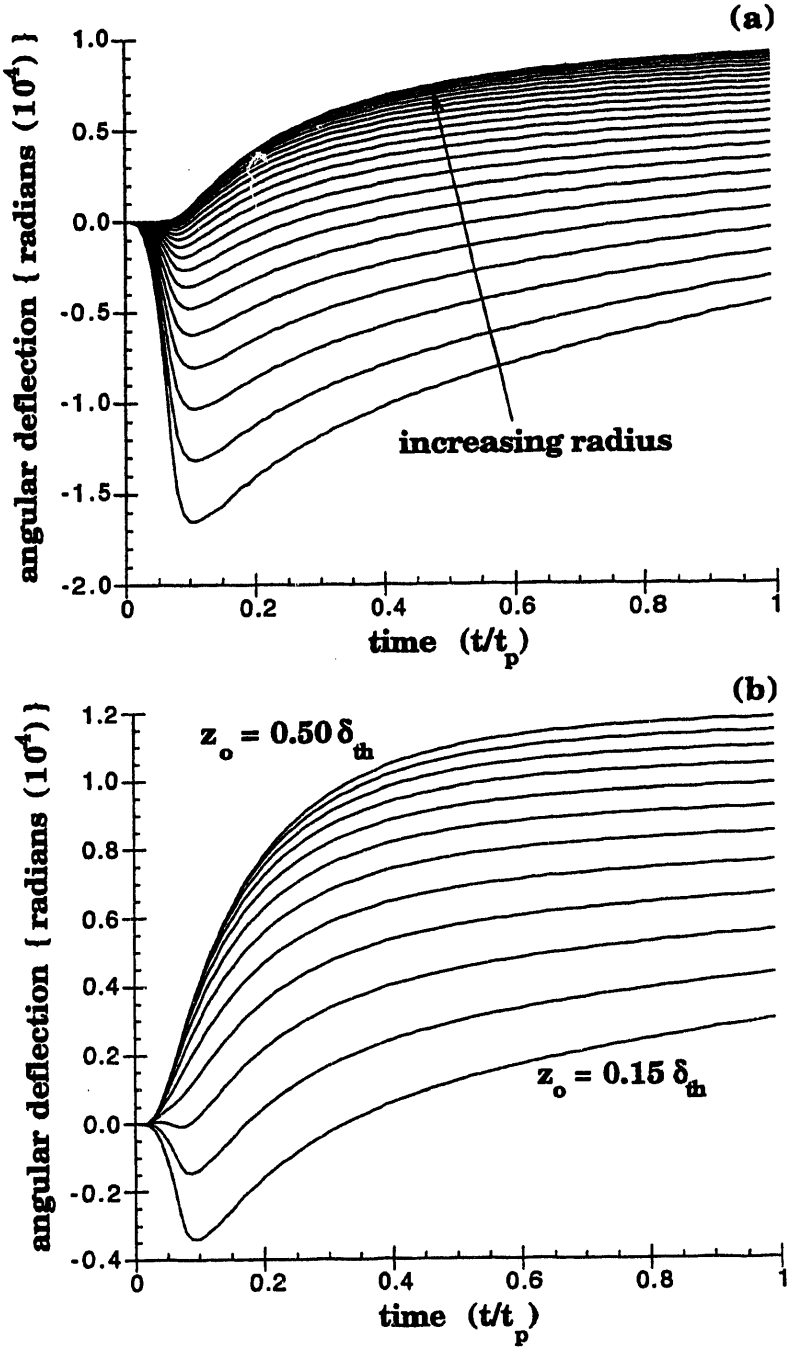

Figure 3.9 Effect of (a) increasing the radius of a probe-beam which is grazing the surface of target from 0 to 1 thermal diffusion lengths in air, δ_{th}, and (b) changing the initial centroid distance of a 200 μm probe-beam from z_o of 0.15 to 0.50 δ_{th}.

(3.7) and (3.12), we also know that neither latent heat nor abrupt property changes can account for maxima or minima if the geometry is planar. At most the magnitude of the heat flux vector may change in time, but not its direction. Therefore, it is proposed here that the propagation of the phase-front along the surface locally changes the heat flux direction due to the absorption of energy required to advance the front. The integrated effect of these local changes near the moving front are reflected in the overall deflection of a ray passing over the surface.

The effect of changing flux directions is readily seen by observing the calculated temperature gradients at the surface as the phase front passes a given point in time. In figures 3.10(a & b) for Ste $\alpha_l/\alpha_a = 1$, the temperature gradient in the normal (a) and the radial (b) direction at the surface shows the changes to the heat-flux at specific times for each $\bar{r}$ position. The phase-front position is projected from the ($\bar{r}$, $\bar{t}$) plane to the gradient surfaces. Plotting the phase-front position in the ($\bar{r}$, $\bar{t}$) plane of figure 3.10(a) shows that the positive ridge in the gradient corresponds with the position of the front. In figure 3.10(b), the heat flow in the radial direction tends to zero at a position just beyond phase-front. The motion of the front serves as a cylindrical sink that absorbs heat from the adjacent medium, changing the direction of the flux vector in time. On melting, the phase-front moves with a velocity found from (3.19a) and (3.17) as

$$\frac{d\bar{X}}{d\bar{t}} = \frac{1/3\ \bar{t}_p}{(\bar{t}_p\ \bar{t})^{2/3}}\ , \tag{3.31}$$

or

$$\frac{dX}{dt} = \frac{1}{3}\sqrt[3]{\frac{Q}{\pi\rho_l L_m}}\ \frac{1}{t^{2/3}}\ . \tag{3.32}$$

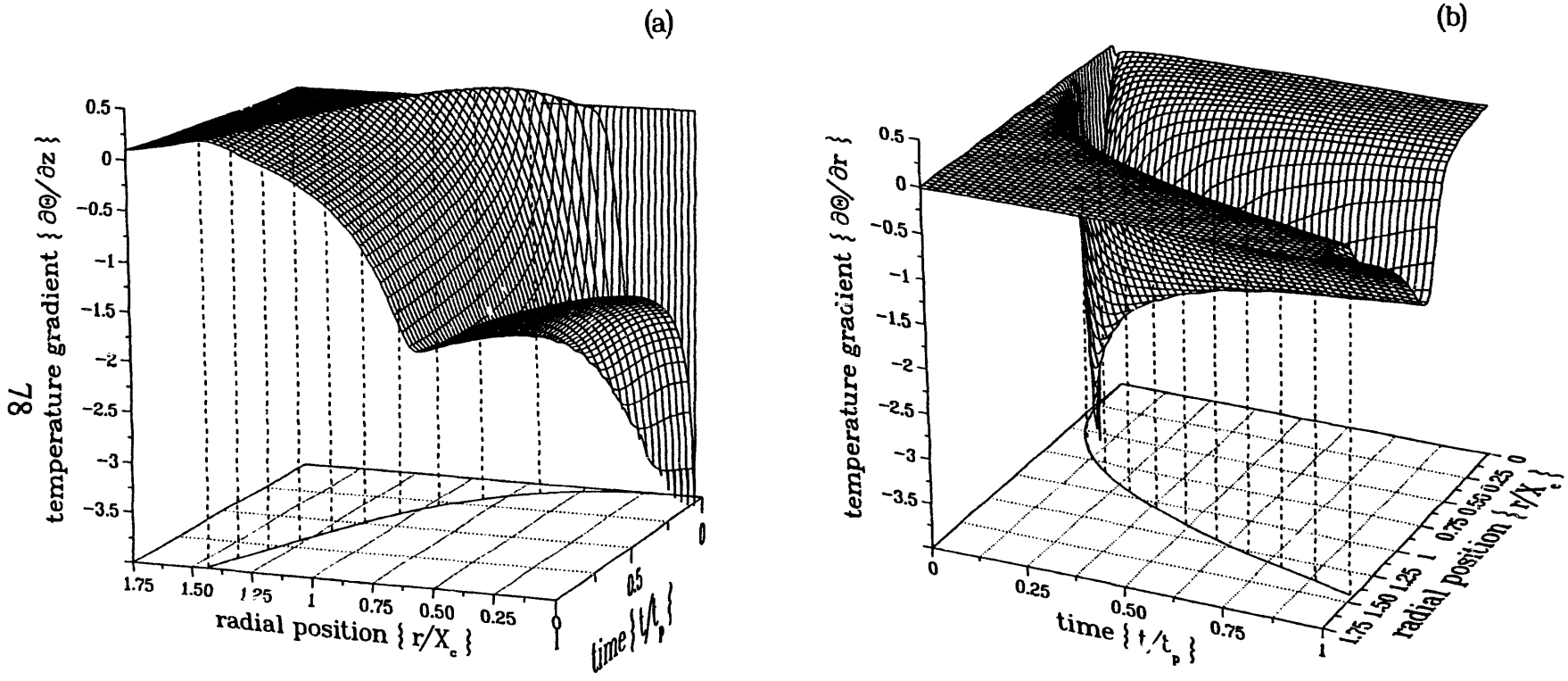

Figure 3.10 Temperature gradients normal (a) and parallel (b) to the surface for the case when Ste $\alpha_l/\alpha_a = 1$ are plotted versus radial position and time. The phase-front position is projected from the ($\bar{r}$, $\bar{t}$) plane showing its effect on the gradients.

As $Q/\rho_i L_m$ increases, the velocity at any given time increases by a power of 1/3. Yet at the onset of melt the velocity is high, even for low power. As seen in figure 3.10(b), the radial component is a strong function of the velocity, since steep gradients exist at small times and decrease at later times. At high velocities, the heat flux vector has a large radial component near the sink. Though the radial component does not directly cause the beam to deflect normal to the surface, it acts to direct the heat towards the sink. As the velocity of the front slows, the radial component diminishes and the negative normal gradients over the melt region cause the probe-beam to deflect in the positive direction. The shape of the deflection, therefore, gives a measure of the velocity of the phase-front at a particular time.

A question that needs to be addressed is when the onset of melt occurs. The point-source model developed has the onset of melt beginning at $t = 0$, since it was assumed that the target was solid at T_m. Figures 3.8 and 3.9 show it is possible to have a local maximum and minimum soon after melt starts. If the velocity of the phase-front at the minima in figure 3.8 is calculated for indium and tin, then from (3.31) the ratio of $d\bar{X}/d\bar{t}$ for indium and tin is 1.3. Comparing the experimental results for indium and tin in figure 3.3, the durations of the first local maximum to minimum are 2.5 ± 0.1 (10^{-4}) sec and 3.6 ± 0.1 (10^{-4}) sec for indium and tin, respectively. If it is assumed that the first local maximum is at the onset of melt, the velocity of X at the minimum would be from (3.32), 0.156 ± 0.004 m/s for indium and 0.095 ± 0.002 m/s for tin, giving a ratio of 1.6. To be consistent with figure 3.8, the onset of melt for the indium case would occur before the first maximum. The laser beam, however, is

not a point-source. Indeed, at small times the area heated by the finite-sized beam would behave more like a planar source at $r = 0$. Using equation (3.9) to estimate the onset of melt for the planar heating case, t_m is found to be approximately 300 μs and 100 μs for the indium and tin, respectively. These times place the onset before the first maximum as shown by the first arrows in figure 3.3. Using the limiting cases of the planar and point-sources as a guide, the onset of melt is estimated to occur just before the first local maxima observed in the PTD signals.

3.4.1 Further Considerations

There are several factors that were not explicitly considered in this work, but should affect the temporal PTD response for studying laser-induced phase-change phenomenon.

The melting of many solids occurs over a range of temperatures, such as with some alloy compounds and polymers. The melt-front moving out from a point-source will absorb heat due to the latent heat of melting over a larger area, but the spatial intensity of this sink on the deflecting medium will diminish. Therefore, whether or not a local maximum or minimum occurs in the signal will depend on the integrated changes to the flux vector across the surface. If PTD is to be used to discern whether or not a material has a unique melting temperature or a range of temperatures for a quickly propagating front, the analysis must be extended to consider this case.

Lasers may radiatively heat a volume of material. The absorption of heat in a solid occurs in a finite volume, which depends on the optical properties of the material as a function of wavelength and temperature.

When the penetration depth is large, a volume of material may undergo phase-change at the same time, even if the melting temperature is unique. In this case, the latent heat is absorbed at constant temperature at the surface, which can modify the direction of the heat flux vector in time. It should be possible, then, for a maximum or minimum to occur over time due to phase-change, even for a planar source. For a finite source with heat energy deposited below the surface, the propagation of the phase-front can differ considerably from the case considered in this work. If the phase-front reaches the surface, the front will again act as a moving sink and the PTD signal should be modified. Detailed analysis of laser heating of a material with a finite absorption depth may reveal whether the onset of subsurface melting can be detected using the PTD technique.

Many materials exhibit strong anisotropy in thermal properties and crystalline structure. Therefore, the transport of heat and the propagation of a phase-front will depend on the orientation of the microstructure in the target. Due to the path dependence of the deflection of a light ray, the shape of the PTD signal could differ markedly from the isotropic materials considered here, depending on directional orientation of the probe-beam. PTD, then, might be used to investigate thermal transport in compounds to determine the degree of anisotropy.

Since PTD can be used to detect the onset of melt due to the latent heat, solidification should also be detected. Yet the experimental results in figure 3.3 and 4 do not show any reversal in direction upon cooling indicating that solidification occurred. For these cases, the surface temperature still exceeds the melting temperature for the time period shown since the cooling rate is considerably slower than the heating rate.

However, there are other factors to consider. The energy leaving the melt region on cooling is broadly distributed, not primarily confined to a small area as during heating. Depending on the thermal properties and boundary conditions, solidification may be a reversal of melting with the phase-front retreating back towards the surface. Or a second solidification front may proceed from the surface inward to meet the retreating front. Furthermore, how a material recrystallizes can determine the microstructure and thus the energy released. The conditions for solidification, therefore, are quite different than for melting, which needs to be examined carefully to correctly use PTD for studying cooling.

Finally, a remark on interpreting a PTD signal with subsequent heating cycles. Figure 3.11 shows the PTD signal for an indium target with four cycles. The first cycle contains the characteristic local maximum and minimum pair associated with the onset of melt. The second cycle, however, does not have such a pair but does have a local maximum and decline suggestive of heating without phase-change for domains with different diffusivities. If the surface is still melted at the resumption of heating, the shape of the second cycle is consistent with heating of the surface without extensive front motion. The third cycle contains a sharp oscillation which corresponds to oxidation of the indium and the evolution of vapor from the surface. Upon oxidation due to abruption of the surface coating, the surface morphology and optical properties of the target change dramatically. These changes cause subsequent PTD responses to rapidly deviate from the previous ones, as seen in the fourth cycle. Melt, vaporization, oxidation, morphology, and changing optical and thermal properties all combine to create a complex PTD signal. Each factor can be

analyzed for their effect on the temporal profile of the PTD signal to fully utilize this technique as a monitoring tool.

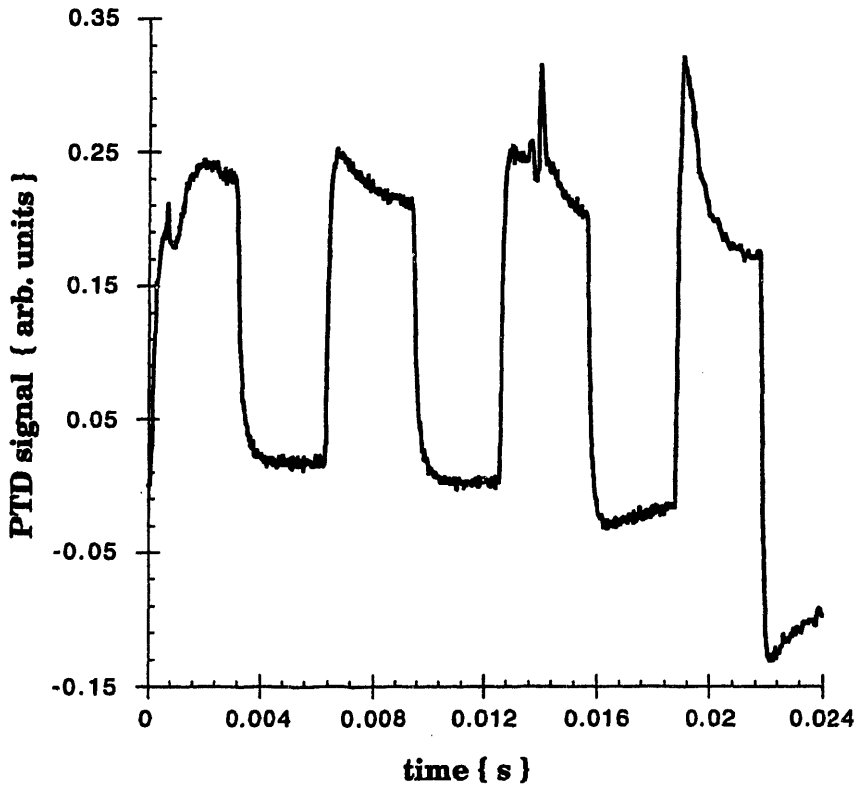

Figure 3.11 Multiple heating cycles show different PTD responses. Coated indium target undergoes melt, oxidation, and laser drilling with an average incident fluence of 2.50 (10^4) W/cm^2. z_o is approximately 100 μm.

3.5 Conclusion

A PTD technique was developed to monitor phase-change which occurs during laser heating of a solid target. The onset of melt can be detected by the presence of a local maximum and minimum pair in the deflection response of a probe-beam passing near the surface. The analysis

showed that this response could not occur if a planar heating source is used. However, when a point heating source is used, a local maximum/minimum pair in the PTD can occur at the onset of melt. Although the effect of changing the pump-beam size is not explicitly analyzed, planar and point-source heating are the limiting cases. As the pump-beam size increases with respect to the thermal diffusion length of the target, the system begins to approach the planar case. When the pump-beam is small, the phase-front will propagate along the surface, modifying the heat flux and thus the PTD signal in time. Therefore, the onset of phase-change at a surface can be detected in real time.

The main parameters governing the detection of phase-change at the target surface are the sensible heat and the latent heat of melting, as well as the thermal diffusivity of the target and deflecting medium. For a process where the latent heat is larger than the sensible heat, a probe-beam can deflect toward the target, causing a local minimum to occur in the temporal PTD response. By modifying the deflecting medium, the ratio of the thermal diffusivities can be changed separately from the ratio of the sensible heat to the latent heat, which can enhance or suppress the minimum. An important finding if this chapter is that the effect of latent heat of melting can be directly observed at a surface. When the thermal diffusivities are equal and there is no phase-change, no maximum or minimum can be observed. However with phase-change, a local minimum can occur in the PTD signal. Moreover, the relative depth of the minimum to the first local maximum will increase as the latent heat of melting grows larger with respect to the sensible heat. The class of materials for which this technique will work is, from a practical standpoint, restricted to

materials where the latent heat of melting is larger than the sensible heat as determined by its melting temperature and the ambient temperature, and where its thermal diffusivity at melt is similar to or smaller than that of the deflecting medium. An example of an important material that meets this criteria is silicon in an argon atmosphere initially at room temperature.

References

[1] W.T. Chan, X.L. Mao, and R.E. Russo, "Differential vaporization during laser ablation/deposition of Bi-Sr-Ca-Cu-O superconducting materials", Appl. Spectroscopy **46** (6), 1025 (1992).

[2] J.C. Gelpey, M.L. Green, R. Singh, J.J. Wortman, Eds., *Rapid Thermal and Integrated Processing*, Materials Research Society Symposium Proceedings **224**, MRS, Pittsburgh (1991).

[3] J.D. Rudnicki, F.R. McLarnon, and E.J. Cairns, *Techniques for Characterization of Electrodes and Electrochemical Processes*, R. Varma and J.R. Selman,, (eds.), John Wiley & Sons, New York (1991).

[4] J.A. Sell, D.M. Heffelfinger, P. Ventzek, and R.M. Gilgenbach, J. Appl. Phys. **69** (3), 1330 (1991).

[5] K. Rajasree, V. Vidyalal, P. Radhakrishman, V.P.N. Nampoori, and C.P.G. Vallabhan, Meas. Sci. Technol. **4**, 435 (1993).

[6] H.J. Seo, S.I. Yun, S.J. Min, and T.Y. Kim, Springer Series in Optical Sciences **62**, 303 (1990).

[7] S.I. Yun and H.J. Seo, Chinese J. Phys. **30** (5), 753 (1992).

[8] C.L. Enloe, R.M. Gilgenbach, and J.S. Meachum, Rev. Sci. Instrum. **58** (9), 1597 (1987).

[9] A.C. Tam, Rev. Modern Phys. **58** (2), 381 (1986).

[10] J.C. Murphy and L.C. Aamodt, J. Appl. Phys. **51** (9), 4580 (1980).

[11] A.C. Boccara, D. Fournier, W. Jackson, and N. M. Amer, Opt. Lett. **4**, 377 (1980).

[12] J.D. Spear, R.E. Russo, and R.J. Silva, Appl. Optics **29** (28), 4225 (1990).

[13] M. Woelker, B.K. Bein, J. Pelzl, and H.G. Walther, J. Appl. Phys. **70** (2), 603 (1991).

[14] H.S. Carslaw and J.C. Jaeger, *Conduction of Heat in Solids*, Oxford University Press, Oxford (1959).

[15] Y.S. Touloukian and C.Y. Ho, Eds., *Thermophysical Properties of Matter*, Plenum Press, New York (1972).

[16] B. Rubinsky and A. Shitzer, J. Heat Transfer **100**, 300 (1978).

[17] W.A. McGahan and K.D. Cole, J. Appl. Phys. **72** (4), 1362 (1992).

[18] A.A. Rostami, R. Greif, and R.E. Russo, In *Transport Phenomena in Material Processing 1990*, ASME Publication HTD **146** (1990).

[19] J.R. Partington, *An Advanced Treatise on Physical Chemistry*, Physico-Chemical Optics **4**, Longmans, Green and Co., London (1953).

[20] J.D. Jackson, *Classical Electrodynamics*, 2nd Ed., John Wiley and Sons, New York (1975).

Chapter 4

Monitoring mechanical transport of energy into a target and surrounding medium during high-power pulsed laser ablation

In this chapter, high-power pulsed laser-material interactions are investigated. At intensities above 10^8 W/cm^2, an explosive, plasma forming interaction occurs between the laser beam and the solid target, ablating material away. Stresses in the target caused by the laser ablation can be very large, which can make mechanical transport of energy significant. In this work, the effect of stress power during laser ablation is considered. Experimental work is conducted to measure how energy and intensity affects the stress power in the target and the power carried by pressure wave in the surrounding gas medium. A 30 nano-second excimer laser is used to ablate aluminum targets, and the resulting stresses are recorded by different types of transducers. The results show that gas ionization breakdown can be detected through the stress power, and that the power measured follows a quadratic dependence on the incident energy. The effect of pressure on the individual components of the stresses in the target is also considered. Variation of the ratio of the shock power in air to the stress power in the target shows that plasma shielding of the laser beam can be monitored using the mechanical stress power.

1.0 Introduction

In most treatments of laser-material interactions, the focus of laser energy transport in a solid target is purely thermal. In the first two chapters, the only transport mechanism considered was thermal diffusion. Convection and vaporization were ignored since the time and energy scales associated with these processes are large compared to those which occurred. Radiative heat transfer was treated only as a boundary condition of the target, since the absorption depth produced surface heating only, and the air atmosphere was essentially non-participating for the 1064 nm wavelengths used in the experiments for heating the targets. At higher laser energies, however, significant vaporization of the target material will occur, and significant amounts of energy will be convected away from the surface. Depending on the vapor's optical properties and density, significant radiative participation with the medium may occur, with subsequent heating of the vapor plume, and modification of the laser heating of the target. In these cases, both convection and radiation must be considered in solving the purely thermal energy equations.

At power densities above about 10^8 W/cm^2 two additional physical phenomena occur which alter the energy transport mechanisms. The first is the dissociation and ionization of the molecules and atoms in the medium and target material. Dissociation leads to the interchange of chemical energy similar to combustion processes. Often the formation of a laser-induced plume above a target is referred as ignition. Ionization of the plume produces a plasma of positively charged particles and negatively charged electrons. A plasma can give rise to electromagnetic energy transport, and radically alters the absorption and emission spectrum and

fluid dynamics of the plume. The main importance of plasma formation is that the incident laser radiation can be shielded from the target through absorption and scattering by the atoms, ions, and electrons in the plume. Moreover, the intense electric field in the laser beam can interact with the electromagnetic fields generated in the plasma, causing self focusing and defocusing, as well as changes to the fluid motion of the particles. From this discussion it is clear that to fully solve the laser/plasma interaction, chemical potential terms must be added to the energy equation, which must be solved simultaneously with Maxwell's equations and fluid dynamics. Presently, a few simplifying approaches have been undertaken to solve the temperature field, ion and electron density in a one-dimensional plasmas [1-3] which assumes a solution for the attenuation of the laser intensity, but considerably more work needs to be done.

The second phenomenon that occurs at high fluence is the rapid blow off or ablation of material and the rapid thermal expansion of the material. The high velocity of the ablation products and the thermal expansion can induce large stresses in the target. Accordingly, laser-induced stresses have been studied extensively. One important problem that has received attention is identifying the onset of ablation of a particular material. Often this onset is defined as the beginning of vaporization. But frequently the onset is considered to be the point where explosive removal begins, corresponding to shock wave generation at ambient pressure or a gas dynamic gas expansion instead of free molecular flow at very low pressures. Therefore, researchers have used photoacoustic monitoring [4], shock wave detection [5,6], and stress wave response in the target [7] to detect the onset. There is also a large amount of literature dating back to

the 1960's on the momentum recoil [8], shock pressures [9], mechanical response to shock [10-13], and stress waves generated by lasers [14,15]. But to date, the rate at which energy carried by the mechanical stress propagating through a target has not been used to monitor laser energy coupling with materials. The question remains, then, the extent to which energy is carried mechanically, and whether or not it must be considered in high-power laser-material interactions.

4.1.1 Motivation for Considering Mechanical Energy Transport

Energy can be transported in a solid due to rapid mechanical deformations, caused by so-called shock or impulse loading. The source of the shock during high-power laser-material interactions is twofold. The first source is from the velocity of the particles leaving the surface. From Newton's Third Law that every action has an equal and opposite reaction, the change in momentum of the particles as they break away from the target must be matched by a change in momentum in the target itself. The force produced by this momentum recoil can be substantial. Particle velocities have been measured by a number of researchers to exceed 5 (10^4) m/s for many medium mass elements[16-18] for periods measuring in nano-seconds. The rate in change in momentum for even a tenth of a micro-gram of material can produce a force on the order of 10 to 100 N. For a moderately focused laser beam with a diameter of 100 μm, this produces a stress at the surface on the order of 10^9 to 10^{10} Pa, or 10,000 to 100,000 atmospheres. Several investigators have deduced pressures of these orders and some have predicted pressures an order of magnitude

greater [3,8,19]. Therefore, the mechanical shock from the impulse produced by the recoil in a solid target can be significant.

Even though the above analysis considers only the momentum recoil of particles streaming off the surface unimpeded in free molecular flow, the force exerted can be greater due to the formation of a gas dynamic region often called the Knudsen layer, and by the formation of a shock wave in the medium above the surface. Due to the high density of the particles leaving the surface with a wide angular and velocity distribution, the frequency of collisions may be great enough to form a Knudsen layer, even in high vacuum [20]. A certain percentage of colliding particles will return back to the surface for a subsequent momentum transferring collision. This in itself would not be enough to increase the impulse force seen by the target, since momentum must be conserved by the colliding particles. However, for the collisions which occur during the laser pulse, there are opportunities by the particles for absorption of photons by inverse Bremsstrahlung (electromagnetic braking of particles), increasing their kinetic energy. The laser heating of the Knudsen layer can therefore increase the impulse and resulting stresses in the target, depending on the pulse length, wavelength, intensity, and absorption properties of the material being expelled. It should be noted that the effect of a Knudsen layer on the energy absorbed by the surface is still an open question. Absorption of photons by the particles in the layer reduces the number available for heating the surface. However, the presence of the layer can substantially change the reflectivity of the underlying material, changing the amount of laser energy absorbed far more than that removed in the Knudsen layer. The attenuation of the laser intensity near the surface is a complicated function of the particle and

electron density, the charge distribution induced by ions remaining at the surface and the resulting Debye length of electron shielding [1,21]. The net result is that the presence of a Knudsen layer can either increase or decrease the amount of energy absorbed by the surface.

If a gas medium exists above the target, the rapid mass flux of particles leaving the target collide with the gas particles, which rapidly accelerates the gas beyond its sonic velocity. The resulting shock wave in the surrounding atmosphere constrains the expansion of the plume, increasing the pressure at the surface of the target. It is difficult to estimate the change in pressure across the expanding shock front during the laser pulse. The first problem is estimating the mean velocity of the gas behind the front. For particles leaving the surface at 5000 m/s, after the angular distribution and collisions are accounted for, the mean velocity normal to the front will be much lower. How much lower will depend on the mass flux. If we use 5000 m/s as an upper bound, the resulting flow can be characterized as hypersonic. Since the temperature of the expanding plume exceeds 5000°K and dissociation and ionization is occurring, it is also a chemically reacting high-temperature flow. As such, the ratio of specific heats $\gamma = c_p/c_v$ is a function of temperature and pressure. To approximate the overpressure, p, behind the front, the hypersonic shock relation [22]

$$p = \frac{2\gamma}{\gamma+1} M^2 \qquad (4.1a)$$

is employed, where M is the mach number using the ambient temperature, T_{amb}. A similar approach is used to estimate explosive blasts in air [23]. If an effective γ is defined from combustion flows to estimate the temperature dependence as [22]

$$\gamma_{eff} = 1 + \frac{2}{M}\left(\frac{T}{T_{amb}} - 1\right), \qquad (4.1b)$$

then (4.1a) gives p equal to 240 atm for T = 5000°K. Of course, for mean velocities or temperatures much different than those assumed, the estimated overpressure would greatly vary.

The shock wave propagating over the surface of the target will affect a much larger area than from the recoil which is confined to the laser irradiated area. A loading on the order of hundreds of atmospheres of pressure would substantially change the stress field experienced by a target. However, the total added force due to the generation of a shock wave might still be much smaller than due to momentum recoil at the particle velocities and time period assumed.

4.1.2 Scope of the Chapter

In this chapter, an effort is made to understand how mechanical stress power changes in a target and in the ambient medium during laser ablation of a solid material. The goal is to monitor stress and shock power to determine how laser energy and intensity affects the energy coupling to the target. This chapter contains:

- The underlying theory on stress power, mechanical waves, and the assumptions made for the material response in the experimental measurements,
- An order of magnitude estimate of stress power that could be present near the laser irradiation zone,
- The analytical method used to determine the power in the experimental signal,

- A brief description of the experimental technique, apparatus, and procedure,
- Results for the measured stress power in a target, the resulting power of a pressure wave in the air above the surface, and how ratios of the individual stress components change,
- A discussion of the observed gas breakdown, and the influence of energy, pressure and spot size on stress power.

4.2 Theory

Mechanical stresses in a target being heated by a laser arise from the thermal expansion of the solid, vapor momentum recoil, shock waves in the ambient medium, phase-change induced density gradients, fracture and ejection of large particles, and for certain materials, electrostriction due to the laser's electric field intensities interacting with the atom/ion lattice. In this work, only the stresses arising from the first three mechanisms are considered.

In this section, the definition of stress power is presented and discussed with respect to an energy balance. The type of mechanical waves which carry the stress power are considered, and the equations governing the waves which are measured are presented. An order of magnitude estimate of the stress power in the ablation region is then presented. The section closes with the method of calculation of the signal power.

4.2.1 Stress Power

When loaded, a solid target deforms, storing energy as potential strain energy, releasing energy kinetically, or dissipating energy through non-conservative, or plastic, deformations. The rate at which the mechanical energy is transported in a body can be referred to as the stress power, P, which is a scalar quantity defined as

$$P = \mathbf{T} \cdot \mathbf{L} \tag{4.2}$$

where $\mathbf{T}$ is the Cauchy stress tensor, and $\mathbf{L}$ is the velocity gradient tensor. As background to this definition, the position of a particle in a body is given as $\mathbf{X}$ in the body's reference configuration. As the body undergoes deformation, translation, and rotation to a new position $\mathbf{x}$ in the current configuration, the response vector function $\boldsymbol{\chi}$ describing that motion is given by

$$\mathbf{x} = \boldsymbol{\chi}(\mathbf{X},t) \tag{4.3}$$

at a time t. The deformation gradient $\mathbf{F}$ is a tensor which relates the motion of the body to the reference configuration by

$$\mathbf{F} = \frac{\partial \boldsymbol{\chi}}{\partial \mathbf{X}} \tag{4.4}$$

which for definiteness is assumed invertible such that det $\mathbf{F} > 0$. The velocity in the current configuration is defined as

$$\mathbf{v} = \dot{\mathbf{x}} = \frac{\partial}{\partial t}(\boldsymbol{\chi}(\mathbf{X},t)) \tag{4.5}$$

and the velocity gradient is

$$\mathbf{L} = \frac{\partial \mathbf{v}}{\partial \mathbf{x}} . \tag{4.6}$$

L is related to the deformation gradient through the material derivative of **F**

$$\dot{\mathbf{F}} = \mathbf{L}\mathbf{F} \tag{4.7}$$

showing that the rate of change of **F** depends on both the deformation and the velocity gradients of the body. The Cauchy strain tensor is related to **F** by

$$\mathbf{C} = \mathbf{F}^{\mathrm{T}}\mathbf{F} \tag{4.8}$$

and the stress tensor **T** is determined by the appropriate constitutive equation relating the stress to strain. The components of **T** are recorded here in indicial notation related to the principal directions in figure 4.1, where

$$\mathbf{T} = \begin{bmatrix} \tau_{11} & \tau_{12} & \tau_{13} \\ \tau_{21} & \tau_{22} & \tau_{23} \\ \tau_{31} & \tau_{32} & \tau_{33} \end{bmatrix} . \tag{4.9}$$

The dimensions of τ_{ij} are force per unit area. The components of **L** are recorded as

$$\mathbf{L} = \begin{bmatrix} v_{1,1} & v_{1,2} & v_{1,3} \\ v_{2,1} & v_{2,2} & v_{2,3} \\ v_{3,1} & v_{3,2} & v_{3,3} \end{bmatrix} . \tag{4.10}$$

where $v_{i,j} = \partial v_i / \partial x_j$ (i,j = 1,2,3) has dimensions of $\{\text{time}\}^{-1}$. In this work, since electric fields do not exist inside the metallic conductive bodies, electrostriction is ignored. Electric moments are not assumed to exist, and all body moment couples are neglected, so **T** is symmetric for this case.

From these definitions, the stress power is the summation of the products of the components of **T** and **L**. At each point in a body, the summation $\tau_{ij}\, v_{i,j}$ describes the mechanical power contained instantaneously in each elemental volume. In a purely mechanical theory, P integrated over the whole body $\mathcal{B}$ is equal to the rate of work by contact forces and by body forces minus the rate of change of kinetic energy, or

$$\int_{\mathcal{B}} \mathbf{T}\cdot\mathbf{L}\ dv = \int_{\Omega\mathcal{B}} \mathbf{t}\cdot\mathbf{v}\ da + \int_{\mathcal{B}} \rho\mathbf{b}\cdot\mathbf{v}\ dv - \frac{1}{2}\frac{d}{dt}\int_{\mathcal{B}} \rho\mathbf{v}\cdot\mathbf{v}\ dv \quad (4.11)$$

where **t** is the stress vector, **b** is the body force vector, and ρ is the density. To complete the energy balance, however, we must include the effects of both volumetric and surface heat transfer, potential and internal energies, and internal heat generation. Note that internal energy density can be expressed in terms of entropy density and temperature to account for changes in energy due to irreversible deformations. Combining the rate of mechanical work with the rate of heat that is supplied to the body, this must equal the rate of change of kinetic energy plus heat density plus the potential energy. Expressing the energy balance in terms of Helmholtz free energy potential ψ, the entropy density per unit mass η, the absolute temperature θ, the external supply of heat r, the normal heat flux $h = \mathbf{q}\cdot\hat{\mathbf{n}}$ gives [24]

$$\int_{\Omega\mathcal{B}} (\mathbf{t}\cdot\mathbf{v} - h)\ da + \int_{\mathcal{B}} \rho(r + \mathbf{b}\cdot\mathbf{v})\ dv = \frac{d}{dt}\int_{\mathcal{B}} \rho(\tfrac{1}{2}\mathbf{v}\cdot\mathbf{v} + \psi + \eta\theta)\ dv \quad (4.12)$$

Equation (4.12) is a general thermal mechanical energy balance which includes internal energy generation terms which can account for the chemical as well as the mechanical processes occurring during laser

ablation of materials. Recognizing that the Helmholtz free energy and entropy densities account for the internal energy density, e, through

$$e = \psi + \eta\theta \ , \tag{4.13}$$

equation (4.12) may be written in a local form which shows the explicit dependence of heat transfer and the rate of change of internal energy on the stress power such that

$$\rho r - \text{div}\, \mathbf{q} - \rho\, \dot{e} = P \tag{4.14}$$

where div $\mathbf{q}$ is the divergence of the heat flux vector [24]. Equation (4.14) gives a direct measure to determine when the stress power becomes significant in short pulsed laser/material interactions. If P is small with respect to ρr, then the stress power can probably be neglected. However, if P is of the order of ρr, then the stress power is a significant mode of energy transport in the target. The relative size of P will be discussed in § 4.2.3.

4.2.2 Mechanical Waves and Constitutive equations

To determine the stress power in the target and surrounding medium, the stresses and motion must be known. The general equations governing the conservation of mass and momentum can be written in local form as

$$\frac{\partial \rho}{\partial t} + \text{div}\,(\rho \mathbf{v}) = 0$$

$$\text{div}\, \mathbf{T} + \rho \mathbf{b} = \rho \dot{\mathbf{v}} \tag{4.15}$$

$$\mathbf{T} = \mathbf{T}^T$$

where the third equation is the consequence of moment of momentum. To solve the equations of motion in $(4.15)_2$, a constitutive equation for stress versus strain must be known. For this problem, we do not know what the

constitutive relation is in the region near the laser irradiation. In the near field, there is a substantial rise in temperature, all three phases are present, and significant dissipative deformations are occurring from fracture and plastic deformation. In regions far from the near field, however, the aluminum target behaves as a linearly elastic, homogeneous isotropic solid. The distance away from the near field needed for this assumption to hold can be estimated by looking at Fourier's law of heat diffusion and the elastic wave speed. In the nano-second time regime, the thermal diffusion length for aluminum is no more than 10 μm and the wave propagation distance is on the order of 200 μm. In these experiments, the transducers are all located in the far field, and actually record the linear elastic response in the target. In indicial notation, the constitutive equations for these conditions are:

$$\tau_{ij} = \lambda\, \varepsilon_{kk}\, \delta_{ij} + 2\mu\, \varepsilon_{ij}$$
$$\varepsilon_{ij} = \tfrac{1}{2}\,(u_{i,j} + u_{j,i}) \qquad (4.16)$$

where λ and μ are Lamé's constants, and $\mathbf{u} = \mathbf{x}\text{-}\mathbf{X}$ is the displacement vector of the material point. It can be shown that in the absence of body forces that a dilatational wave is described in terms of displacement by the wave equation[25]

$$\nabla^2(\nabla\cdot\mathbf{u}) = \frac{1}{c_1^2}\frac{\partial(\nabla\cdot\mathbf{u})}{\partial t} \qquad (4.17)$$

where c_1 is the wave speed given by

$$c_1 = \left(\frac{\lambda + 2\mu}{\rho}\right)^{\frac{1}{2}} . \qquad (4.18)$$

Similarly, a distortional wave equation is

$$\nabla^2(\nabla\times\mathbf{u}) = \frac{1}{c_2^2}\frac{\partial(\nabla\times\mathbf{u})}{\partial t} \qquad (4.19)$$

where $c_2 = (\mu/\rho)^{1/2}$. The corresponding waves recorded by the stress transducers are the compression and shear waves as depicted in figure 4.1.

Besides the longitudinal compression and shearing waves, there are Rayleigh waves that propagate along the surface of a half-space as shown in figure 4.1. These waves are two dimensional which propagate with a velocity of $c_R = 0.9194\ c_2$ [25]. There are several things to note about these surface waves. The primary point is that they have the ability to carry a substantial fraction of the elastic stress power away from the near field.

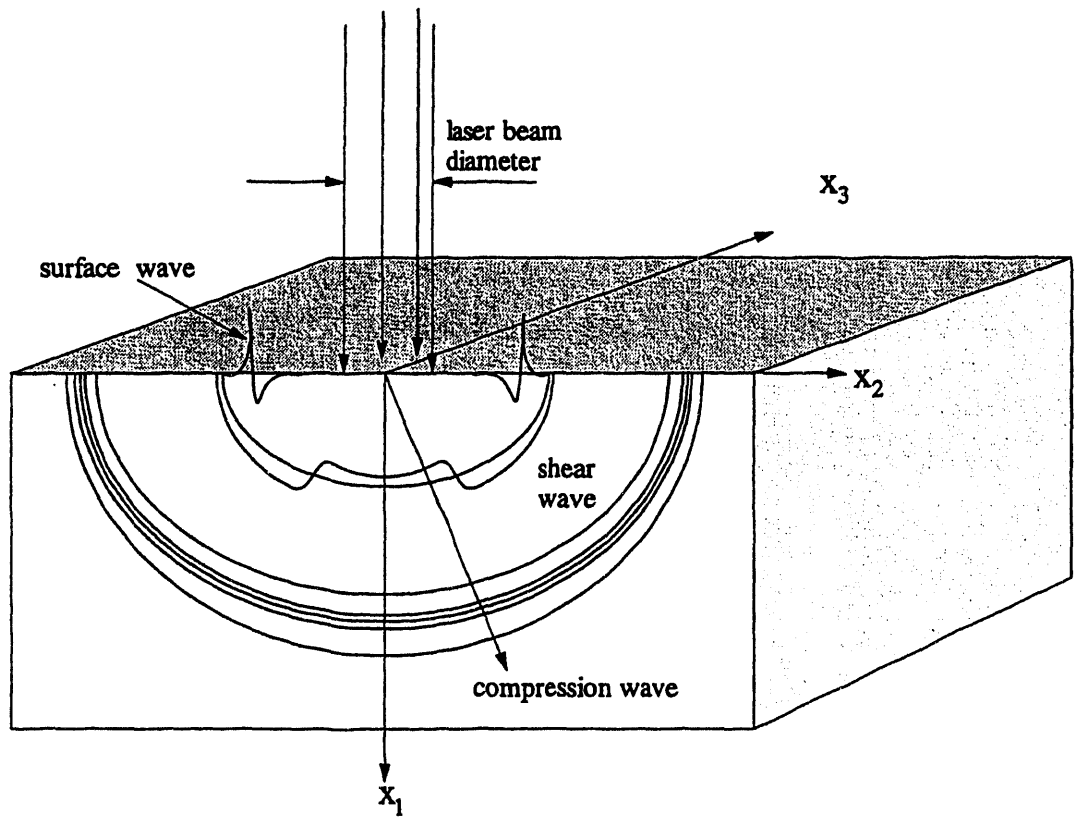

Figure 4.1 Conceptual drawing of mechanical waves propagating in a half-space due to irradiation of the surface with a finite size laser beam.

Also, solutions to surface wave equations show that the Rayleigh waves attenuate exponentially into the half-space, but only attenuate $\sim r^{-1/2}$ along the surface from the point of origin for the impulse type loading experienced in these experiments [26]. Compare this with the longitudinal and shear waves that attenuate $\sim r^{-1}$ in the body and $\sim r^{-2}$ along the surface. Due to these differences in attenuation, the magnitudes measured by the transducers the same distance from the near field will not have changed proportionally from their values at $r = 0$. The Rayleigh wave will have attenuated less and will measure a greater magnitude than the longitudinal and shear waves measured at the surface or in the body. Another feature of the Rayleigh wave is that it is non-dispersive, unlike the body waves, so attenuation of magnitude and power due to changes to the frequency, and thus wavelength, does not occur. Therefore, the measured Rayleigh wave in the far field will be greater than that of the body waves for the same input in the near field.

4.2.3 Stress Power Considerations

A pertinent question that needs to be addressed is when must the stress power be considered when solving the energy equation for laser material interactions. At low intensities of less than 10^4 W/cm^2, laser heating produces negligibly small mechanical response. Even for a slowly heated body that is fully constrained and plastically deforms, the stress power is small with respect to the incident power. In midrange intensities, less than 10^7 W/cm^2, whether or not P is large locally in a body depends strongly on the geometry, material, and optical properties. At intensities

above 10^8 W/cm^2, laser ablation occurs for nearly any material and significant loading occurs locally to the incident laser beam.

To illustrate, consider a loading of 10^{10} Pa caused by a 30 ns 0.5 J laser pulse with a 100 μm laser spot size and an average power of 17 MW. The energy travels into the target at a wave speed, c, which is at least the elastic wave speed of the material. As will be discussed shortly, for fully compressed materials the elastic wave speeds may be considerably surpassed. Assuming that the largest volume of material affected by a one-dimensional wave propagation is the laser spot area times the maximum distance, $x_1(\max) = c\ t$, then an average value for **L** may be approximated by

$$\mathbf{L} \approx \frac{\Delta v_1}{\Delta x_1} \approx \frac{c}{c\,t} = \frac{1}{t} = \frac{1}{30\ 10^{-9}\ \mathrm{s}} = O(10^7)\ \mathrm{s}^{-1}\ . \qquad (4.20)$$

The stress power is on the order of 10^{17} W/m^3, and the effected volume, $\mathcal{V}$, is on the order of 10^{-12} m^3 for an elastic wave speed of c_e = 5000 m/s. $P\mathcal{V}$ for this case is roughly 1 MW, which is a small but appreciable fraction of the total available power from the laser. If a shock wave were to propagate through the material and $c > c_e$, then $P\mathcal{V}$ would increase linearly with c. From elastic wave theory, we know that the longitudinal wave velocity given in (4.18) in terms of the elastic modulus E and Poisson's ratio ν such that [25]

$$c_1 = \left(\frac{E(1-\nu)}{\rho(1+\nu)(1-2\nu)} \right)^{\frac{1}{2}} \qquad (4.21)$$

tends toward infinity as $\nu \rightarrow 1/2$. We also know that beyond the elastic limit, materials may deform plastically which is often thought to be an

isochoric process. Thus, for an isochoric process where ν approaches 1/2, the wave speed would tend to grow without bound unless constrained by conservation of energy. For the aluminum targets used in the experimental work, the static yield strength is on the order of 2.5 (10^8) Pa. Considering inertial forces which resist yield under dynamic loading, work hardening, and tempering which may occur during repeated loading, 10^9 Pa is a conservative estimate of the yield strength of aluminum under dynamic loading. With the loading an order of magnitude greater than yield, it is reasonable to assume that the material in the near field of the laser irradiated surface could be fully compressed. As such, the wave speed will greatly exceed the elastic limit, and thus $P\forall$ would only be limited by the partition of the laser energy between plasma heating, thermal heat transfer, and the dissipative plastic deformation processes.

4.2.4 Calculation of Signal Power

In the calculation of the mechanical power measured by the stress transducers, it is important to remember that the transducers are only recording changes in the far field that are caused by changes in the near field. The actual power transmitted and dissipated in the near field can be significantly different than the transmitted power measured in the far field. The power that is dissipated in the near field will thermalize, causing an additional thermal expansion to be recorded in the far field. However, the time response is much slower than that of the mechanical wave, and thus the power measured will be less. The dissipation of power in the near field will cause the power recorded in the far field to be less than what actually occurred. Power is also dissipated due to scattering and dispersion over the

distance to the transducers. Therefore, the power recorded in the far field is also a lower bound of what actually occurs in the near field.

The transducers employed in the measurements produce a voltage whose potential is proportional to the stress integrated throughout the active piezoelectric transducer element. The resulting voltage is a scalar quantity that is proportional to the average stress in the element volume. The individual components of the stresses in the transducer all contribute to the voltage output in time. Dividing this average stress by the volume gives a stress per unit volume that is changing in time. For an averaged scalar stress given by 1/3 tr **T** along the principle stress directions in a isotropic homogeneous linear elastic material, where tr **T** is the trace of **T**, the stress power in (4.2) can be written

$$P = C \, \mathrm{tr}\,\mathbf{T} \; \overline{\dot{\mathrm{tr}}\,\mathbf{T}} = 2C' \, \sigma\dot{\sigma} \qquad (4.22)$$

where C and C' are proportionality constants, and σ is the average stress in the transducer. Therefore, the average stress power at any time in the transducer is a function of the stress and the rate of change in the stress.

The average power contained in a signal, s(t), is calculated by employing Parseval's theorem, which states that

$$\int \langle s^2(t) \rangle \, dt = \int \langle |S(f)|^2 \rangle \, df \qquad (4.23)$$

where $\langle s^2(t) \rangle$ is the mean-square of the signal denoting the average power, and S(f) is the Fourier transform of s(t) [27]. Equation (4.23) holds over infinite time, and the mean of a random signal is defined as

$$< s(t) > = \lim_{T \to \infty} \frac{1}{T} \int_0^T s(t)\ dt \qquad (4.24)$$

where T is the time period for repetition. When T is finite, the equality in (4.23) still holds if the mean value of every subset p of s has the same value as the total, or

$$< s_p(t) > = < s(t) > \qquad (4.25)$$

for all t and p. The resulting process for such a random signal is ergodic. For these experiments, the time data acquired from the transducers was made ergodic by fitting a curve to pass through the mean of the signal and subtracting off the baseline curve from the data. In terms of the stress power, the time quantity in (4.23) is actually

$$s^2(t) = C' \frac{d}{dt}(\sigma^2(t)) \ , \qquad (4.26)$$

from (4.22). In the Fourier domain, using the convolution theorem on (4.26) transforms the now ergodic integral in (4.23) to

$$\int | S(f) |^2 \ df = 2C' \int f \Sigma(f) \Sigma^*(f)\ df = 2C' \int f \Sigma^2(f)\ df \qquad (4.27)$$

where $\Sigma(f)$ is the Fourier transform of $\sigma(t)$, and Σ^* is the complex conjugate [28]. The power is calculated by performing a fast Fourier transform on the data, squaring it, and discretely integrating (4.27). The power contained in the baseline curve is then calculated in time and added back to the result. This correction proved to be small with respect to the total power. The data analysis was performed using *Mathematica*, and the sample program is contained in Appendix II.

4.3 Experimental

In this work, a series of experiments were carried out to consider separately the effect of energy, intensity, and spot size during excimer laser ablation of aluminum targets in air. The mechanical response of the ablation was detected with three different types of transducers to identify each separate stress wave carrying energy: the density wave in the ambient medium, and the longitudinal, shear, and surface waves in the target. Plate, or Lamb, waves are ignored due to the short time periods involved and the geometric configuration of the target, transducer and holder which minimizes their production. In the first series of experiments, a 2 mm thick aluminum sheet was ablated using 16 different energy levels and 8 different spot sizes for a total of 128 intensities. The purpose of this group of experiments was to observe how the total stress power *as measured* in the target changed as a function of energy and intensity. Using the same 2 mm plate for the next series, the density wave and stress waves in the target were recorded using 4 different energy levels which spanned over the previous 16, with the same 8 spot sizes. In the last series, a semi-infinite aluminum target was ablated using the same 4 energy levels and 8 spot sizes. The purpose of these two series were to record the onset, magnitude, and power of the individual components of the mechanical waves to determine how the individual modes of transport change as a function of energy and intensity.

4.3.1 Apparatus

A schematic of the apparatus used for the experimental work is shown in figure 4.2. The laser is a Questek 2860 excimer operating at

248 nm with a half-maximum pulse length of 30 ns. Power attenuation was achieved through a combination of 25 and 50% beam splitters and energy output adjustment of the excimer. The energy output ranged from 250 to 550 mJ per pulse. The excimer beam was passed through an aperture to achieve an 8 mm diameter top-hat beam profile. A silicon photodiode was used to capture the energy of each shot of the laser, which first passed through a 94% reflecting UV-grade fused-silica mirror, and a glass microscope slide. The photodiode output was calibrated using a Molectron model PD-104 NIST traceable pulsed-laser power meter for

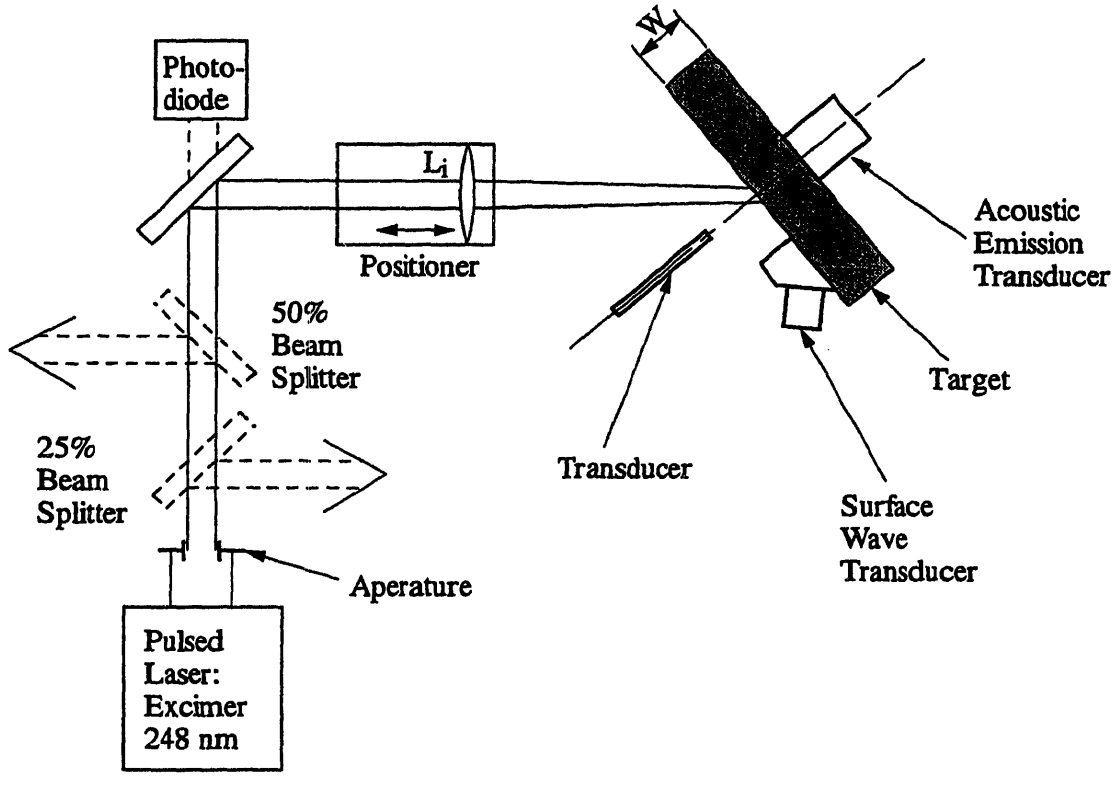

Figure 4.2 Schematic of the experimental system. Beam splitters are moved in and out for a total combination of 4 powers. $L_{i=1,2}$ are the focal lengths 33 mm and 70 mm for the first and second experimental series. Width W = 2 mm and 38.5 mm for the respective series. Lens positioner changes spot size.

each combination of beam-splitters and energy levels. The laser-beam passed through a single quartz lens. The focal length was L_1 = 33 mm at 248 nm for the first series of experiments and L_2 = 70 mm at 248 nm for the second. The spot size was altered by translating the lens with respect to the target. A new location on the target was used for each energy level and spot size by shifting the target relative to the beam and transducers. The spot sizes were determined by measuring with a microscope the burn and ablation patterns made at the plane of incidence on UV burn paper. The targets are 6061 Al in T6 condition, with both surfaces lapped flat to within 10 μm per cm and finished with 600 grit sandpaper. The surface at each spot size was preconditioned with approximately 100 laser pulses at 5×10^6 W/cm^2 intensity. In the first two series, the target is 2 mm thick by 8 cm square, and in the last, the target is 3.85 cm thick by 30 cm diameter round. A one inch diameter acoustic emission transducer (AET) with a –3 dB frequency response from 10 kHz to 18 MHz was placed at the rear of the target along the centerline of the irradiated spot for all the series to detect longitudinal and shear waves propagating through the material. A 1/2 inch diameter 1 MHz Panametrics transducer mounted on a Panametrics 45° shear wave wedge for aluminum, was placed 4 cm from the center of the spot for the last series to detect longitudinal, shear, and Rayleigh waves propagating along the surface of the material. It should be noted that although the Rayleigh wave angle for Al is approximately 69° and the angle for transmitting longitudinal waves is less than 30°, the 45° wedge had a sufficiently large enough solid angle with respect to the source at the 4 cm placement that all modes at the surface could be detected with the same transducer. Both of these transducers were mounted on a thin

layer of Dow Corning silicone high vacuum grease. A Valpey-Fisher model VP-1093 0 to 1.2 MHz Pinducer was placed 5 mm from the surface along the centerline normal to the spot for the second series to detect the density wave propagating through the air. The Pinducer's response is linear up to approximately 2000 atm when saturation is reached. The saturation voltage is well over 5 V into a 20 Ω load. The peak voltage reached was a fraction of that at 1 MΩ impedance. All of the data was captured with a Tektronix model 602A digitizing oscilloscope.

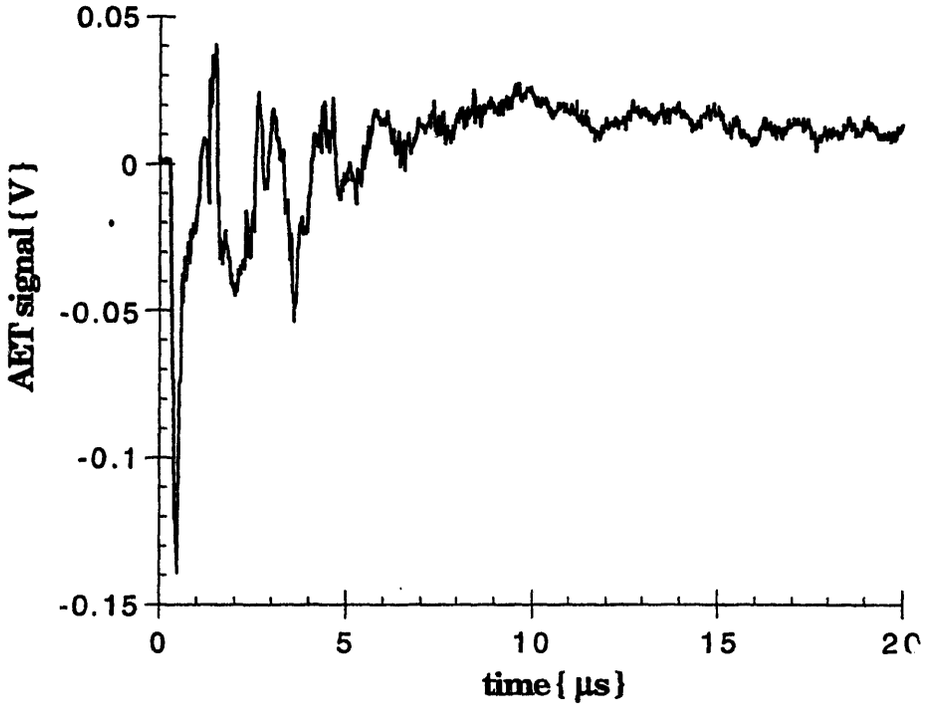

Figure 4.3 Representative trace from the AET transducer from the ablation of a 2 mm thick Al target. Laser beam focused to 1.0 mm spot size, with energy of 20 mJ/pulse.

For the first series of experiments, the first 20 μs of data was recorded for analysis. For the 2 mm thick sample used in this series, multiple reflections with significant mode conversion occur in a time period over 200 ms. Since the scope of these experiments is to determine changes which occur in the near field at short time periods, the relevant information is contained in the first few micro-seconds. For 2 mm thick aluminum, the first longitudinal reflections would reach the AET after approximately 1 μs and the first shear waves after 2 μs. Furthermore, there is significant scattering occurring in the near field which would lengthen the time period for all the waves to reach the transducer. The initial wave trains died away by 20 μs before additional reflections and plate vibrations reached the transducer as seen in figure 4.3. Also, the power content in the 20 μs time period closely followed the trend for power content in the 200 ms time period, except that the mean value changed with target thickness. Since important temporal information would be lost in the early time period due to discretization, and information of questionable content is present in the long time frame, only the first 20 μs of data was analyzed.

4.3.2 Results

The results the stress power for the ablation of the 2 mm Al target over 128 intensities will first be presented, followed by the power in the density wave in air for 32 different intensities. This section concludes with the results for the changes in the stress component ratios with intensity for the 3.85 cm thick Al target.

The log of the calculated signal powers for 8 different spot sizes are shown in figure 4.4 versus the log of the intensity. As is immediately

apparent for each spot size, the signal power grows exponentially with intensity. The signal power, and thus P, grows according to the power law

$$P = c\, I^m \qquad (4.25)$$

where the values for c and m are tabulated in Table 4.1. For the first five runs, the exponent m averages 2.34, and for the final 3 runs m average 1.76. Therefore, the stress power has a near quadratic dependence on intensity for a given spot size. Yet, for the first five spot sizes ranging from 4 to 1 mm in diameter, the signal power has only a weak dependence on area. For the first few energy levels in each run, there is virtually no

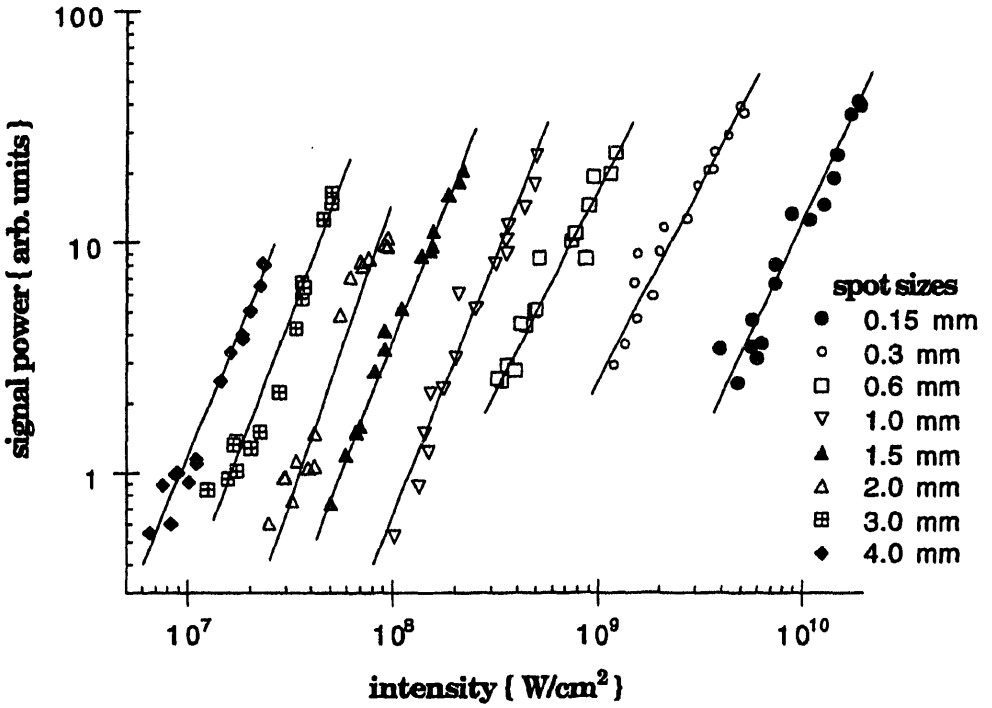

Figure 4.4 Signal power from AET transducer during ablation of a 2 mm thick Al target. Intensity varied by changing the nominal incident energy from 20 to 100 mJ/pulse, and varying the area over 8 spot sizes.

increase as the spot size decreases, even as the intensity increases by over an order of magnitude. At the higher energy levels, there is a weak dependence on area, as P roughly increases with m at 0.2. The most telling change to P versus size occurs when the spot size decreases below 1 mm in diameter and the base power level jumps nearly an order of magnitude. Yet the smallest three sizes again exhibit a weak dependence on spot size after the apparent stepwise change has occurred.

Table 4.1

Values for $P = c\ I^m$ from Figure 4.4.

Spot Size { mm }	c	m
4.0	$6.3\ (10^{-16})$	2.18
3.0	$7.7\ (10^{-18})$	2.37
2.0	$3.4\ (10^{-20})$	2.58
1.5	$1.5\ (10^{-18})$	2.30
1.0	$5.3\ (10^{-19})$	2.26
1st 5 avg.	$1.3\ (10^{-17})$*	2.34
0.6	$7.9\ (10^{-15})$	1.70
0.3	$1.7\ (10^{-15})$	1.69
0.15	$1.0\ (10^{-18})$	1.91
last 3 avg.	$8.4\ (10^{-16})$*	1.77

* Averaged using m(avg.)

A plot of the log of signal power as a function of the log of the pulse energy in figure 4.5, confirms that the change in P is essentially independent of spot size for the laser diameters ranging from 1 to 4 mm. For the spot sizes less than 1 mm, the signal power starts at a baseline an order of magnitude higher than for those ≥ 1 mm, and then approaches the values reached by the larger spot sizes. Note that for the 0.6 mm spot size, the signal power starts wiin those at 0.15 and 0.3 mm at 20 mJ but nearly joins with those ≥ 1 mm at 100 mJ/pulse. Assuming the trend would continue, the stress powers for all spot sizes appear to intersect as the

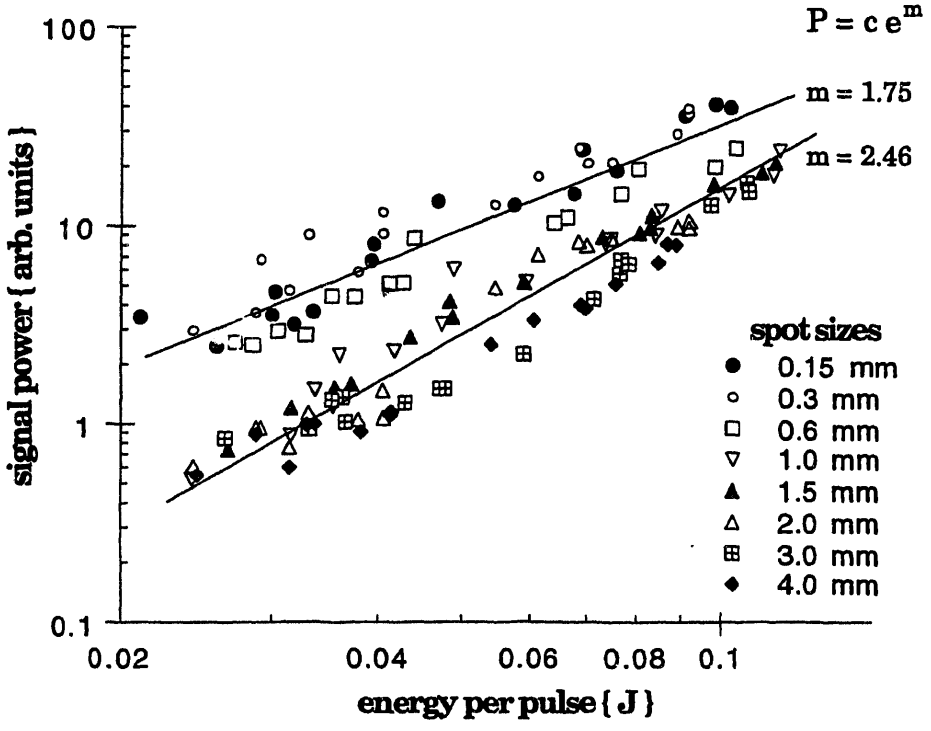

Figure 4.5 Signal power from AET transducer for ablation of 2 mm Al target versus energy per pulse. Data taken for 8 spot sizes as shown.

energy is increased beyond 100 mJ/pulse. The change in slopes noted in Table 4.1 between the first five and the last three spot sizes appears to be only a function of the change in the baseline stress power at the lowest energy levels.

For the shock wave measurements, the power of the density wave in air is plotted in figure 4.6 as a function of the energy per pulse for 4 different energy levels. The effect of spot size has a clear effect on the strength of the density wave in air. Starting at 20 mJ, the power of the

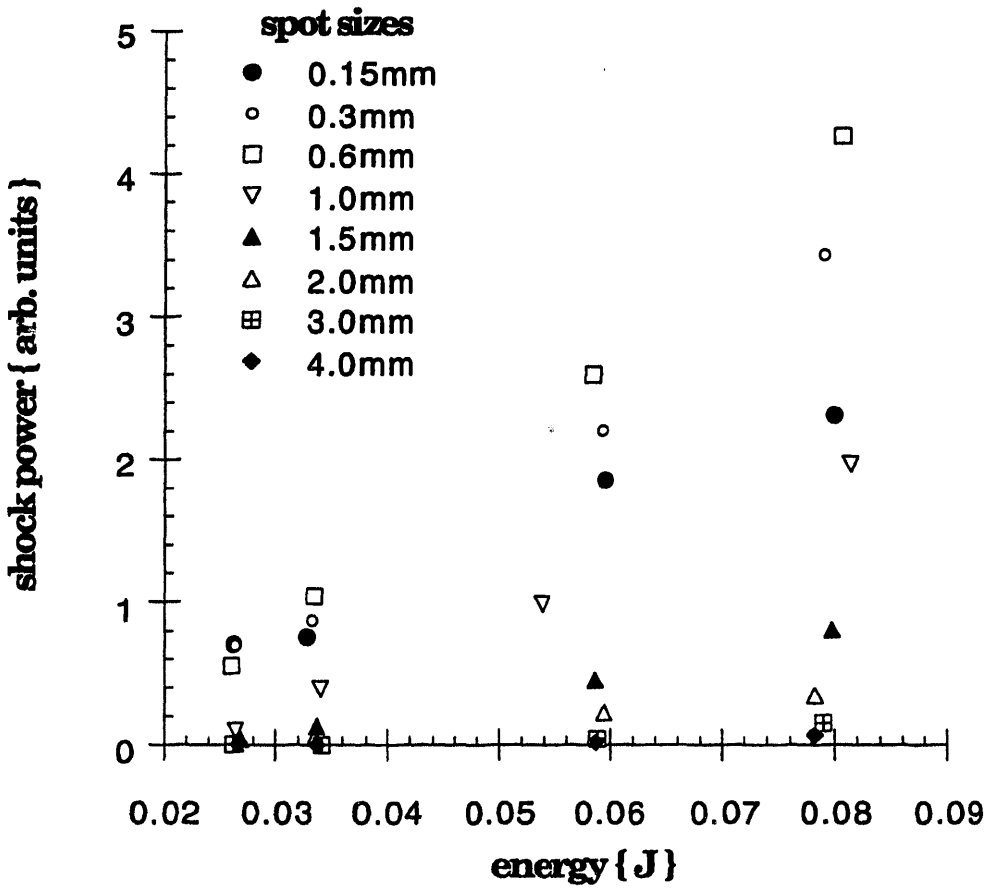

Figure 4.6 Signal power from Pinducer of density wave in air created by irradiation of Al target is plotted versus energy per pulse.

density wave in air for spot sizes ≥ 1 mm is essentially zero, since it is acoustically propagating at the speed of sound. Yet for the spot sizes below 1 mm in size, the density wave is now much greater than zero and was observed to travel faster than sound. As the energy increases, the power of the resulting shock increases but not uniformly. The power is flat for the 3 and 4 mm spot sizes, and grows slowly for the 2 mm spot size. For those less than 2 mm, the shock power grows quickly, but note that the highest power is achieved by the 0.6 mm spot size, and that at the highest energy level it is greater than at 0.3 mm which is greater than at 0.15 mm. These results were repeatable for different runs with different setups.

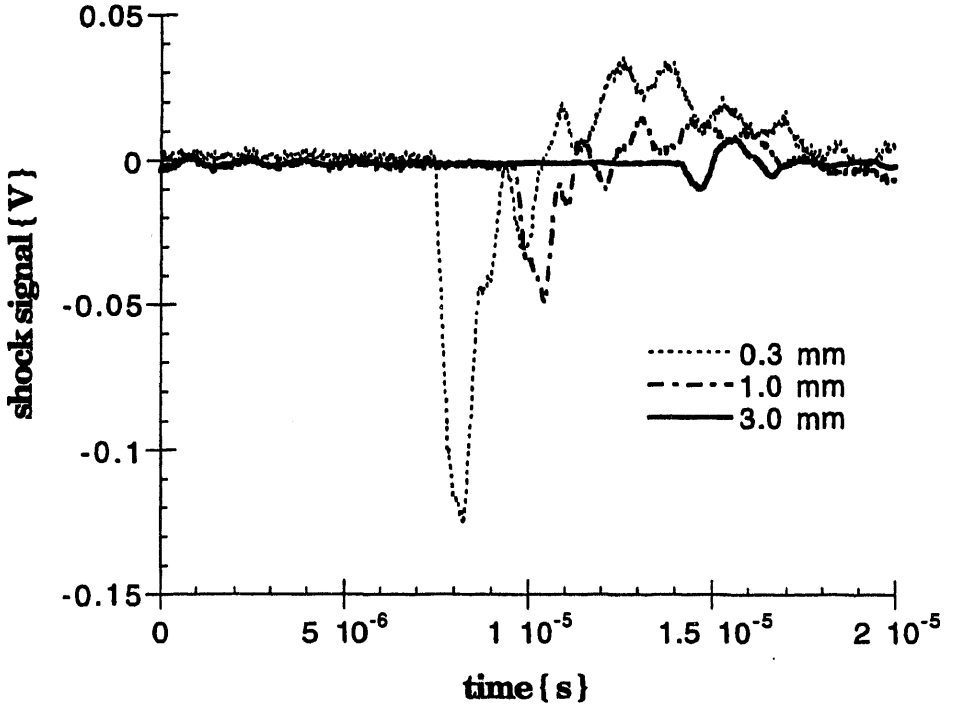

Figure 4.7 Representative traces of Pinducer signal for density waves in air. Laser focused to 0.3, 1.0, and 3.0 mm diameter with energy at 20 mJ/pulse.

Representative traces of the shock signal are shown in figure 4.7 for the 0.3, 1, and 3 mm spot sizes. Note that not only does the magnitude of the shocks increase as the spot size decreases, but the speed of the shock wave increases as well, indicating the velocity and pressure of the gas behind the shock has increased as well. The time of onset for the 3 mm spot size trace corresponds with the sound speed in air.

Normalizing the shock wave power with the stress power in the target gives a measure of how the shock power affects the stress power. In figure 4.8, the log of the power ratio of the shock to the AET signal for

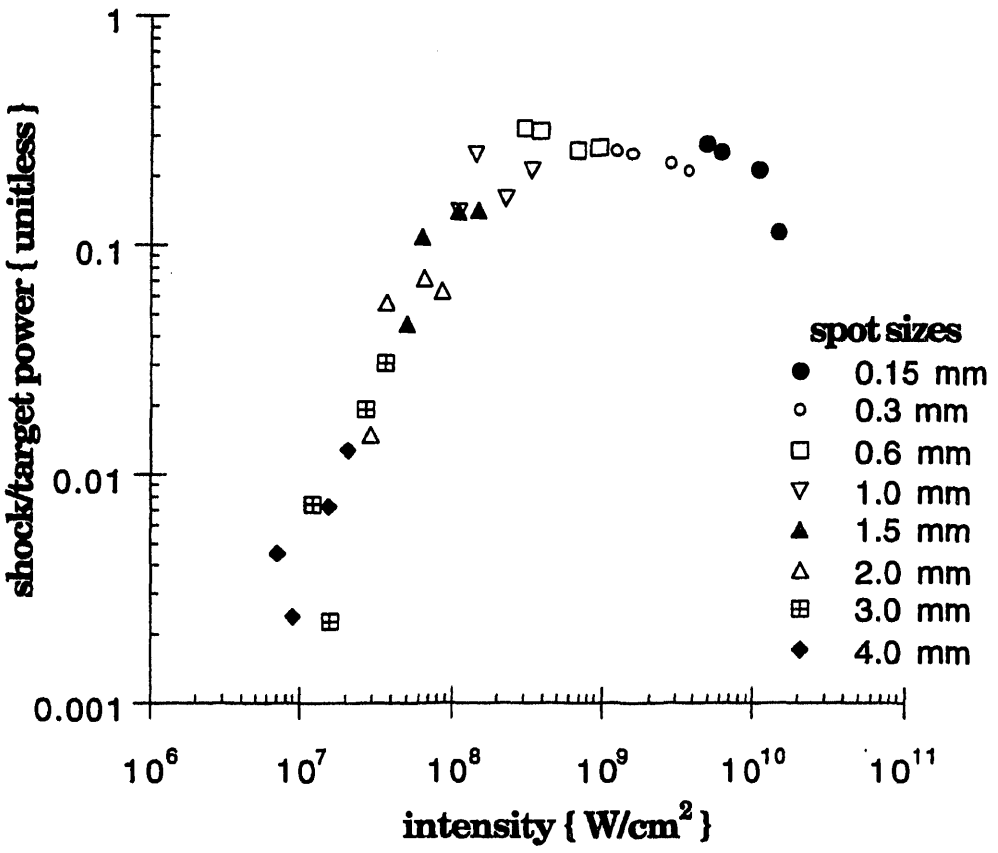

Figure 4.8 The ratio of the stress power in air over the target power is plotted versus the incident intensity at the surface of an Al target.

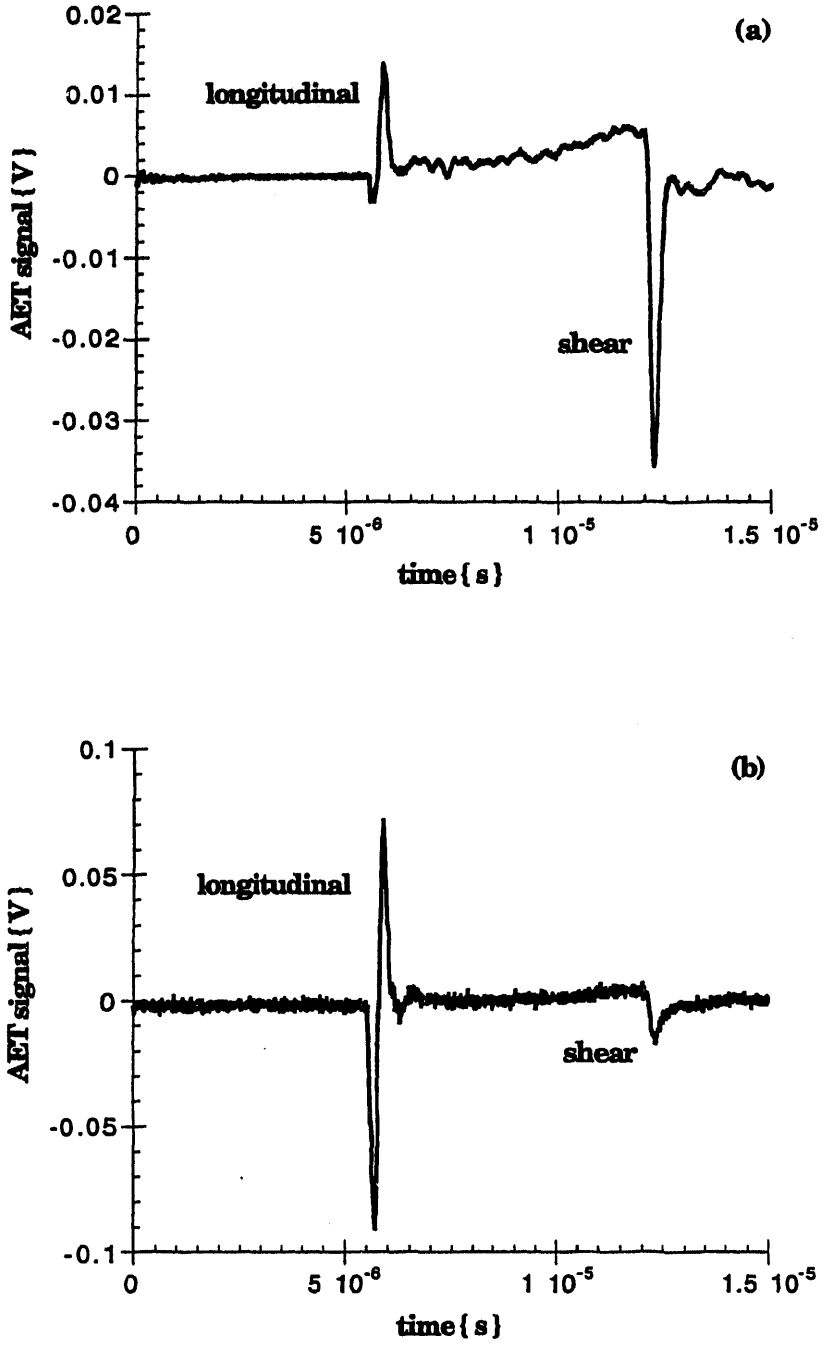

Figure 4.9 Representative traces of AET signal showing longitudinal and shear waves propagating in 38.5 mm thick Al target. Laser beam focused to 1 mm diameter at surface with incident energy at 20 mJ/pulse.

each run is shown as a function of the log of the intensity. The ratio increases linearly on the log-log plot at a rate of 1.7 decades to 1 decade of intensity until about 10^8 W/cm^2 where it begins to roll off. A plateau is reached and then the ratio decreases above 10^9 W/cm^2. Two features are noteworthy for figures 4.6 and 4.8: 1) below 10^8 W/cm^2 the shock power increases faster than the stress power and above 10^9 W/cm^2 the situation is reversed, and 2) unlike for the stress power, the shock power is directly related to the spot size. Above 10^8 W/cm^2, the shock power begins to roll off with intensity whereas the stress power does not.

In the second series of experiments in the semi-infinite Al target, the individual components of the stress power were measured versus intensity. The stress waves observed were the longitudinal wave in the body and at the surface, the body and surface shear waves, and the Rayleigh surface waves. Figures 4.9(a & b) shows representative traces of longitudinal and shear waves in the body for 3 mm and 1 mm spot sizes at 20 mJ/pulse. Note that the magnitude of the shear wave is much greater than the longitudinal wave for the 3 mm spot size, and the situation is reversed for the 1 mm spot size. Also, note that the magnitude of the longitudinal wave is 16 times larger at 1 versus 3 mm spot size, but the shear wave magnitude is slightly less at 1 versus 3 mm.

Plotting the magnitudes of the shear over the longitudinal waves in figure 4.10 shows that the power carried by shear versus longitudinal wave decreases with intensity until about 2×10^8 W/cm^2 before leveling off. A slight rise is seen above 10^{10} W/cm^2. Note that the pattern for the magnitude of the shear and longitudinal waves versus intensity follows a

similar but inverse pattern as the shock over stress power plotted in figure 4.8.

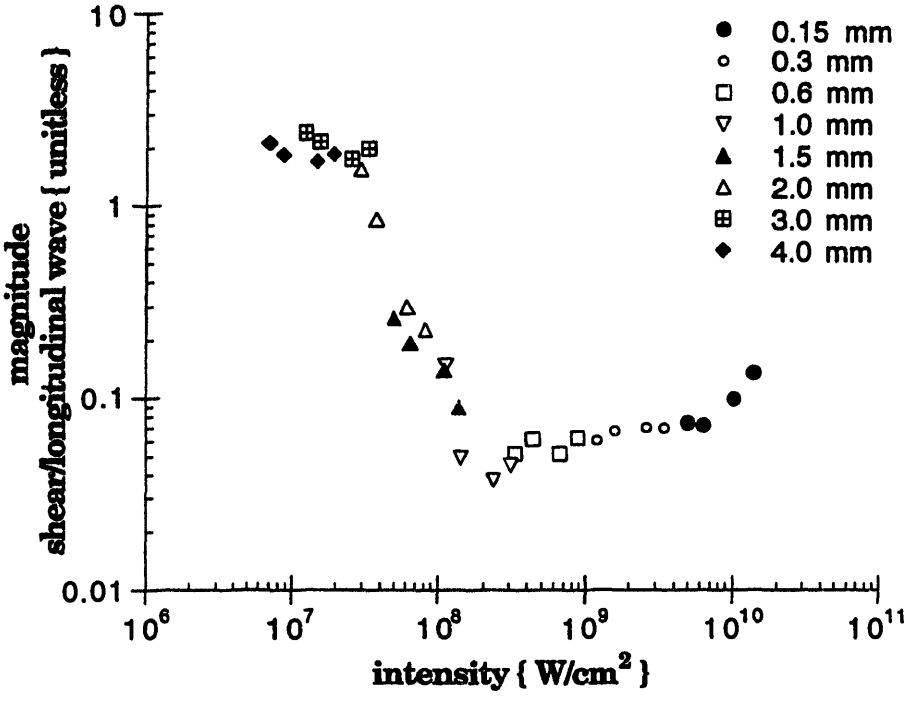

Figure 4.10 The ratios of the shear over the longitudinal wave magnitude are plotted versus intensity for eight spot sizes, at four different energies per size.

Surface waves were monitored to determine how much power is carried along the surface, and to estimate the relative size of the shear stress component in the plane of the surface, τ_{23} in equation (4.9). Figure 4.11 shows representative traces of longitudinal, shear, and Rayleigh waves at the surface of the target for 3 mm and 1 mm spot sizes at 20 mJ/pulse. The magnitude of the Rayleigh is approximately 4 times larger than the longitudinal wave at the surface, indicating that the power carried by the Rayleigh wave is significant. Note that the shear wave is vanishingly small

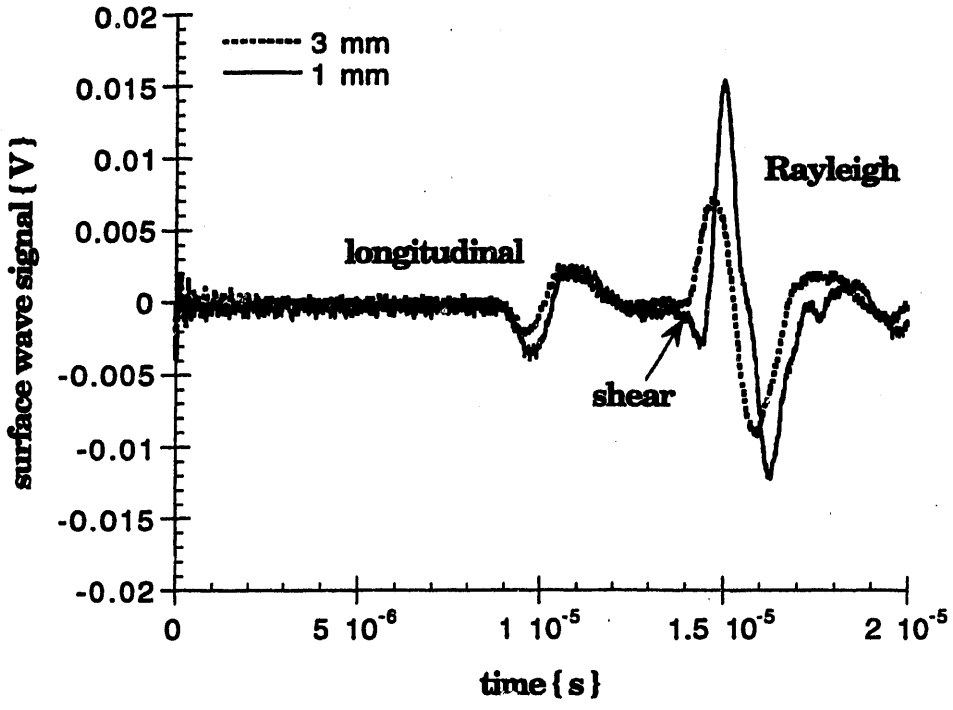

Figure 4.11 Representative traces from the surface wave transducer that shows the longitudinal, shear, and Rayleigh wave propagating at the surface of the 38.5 mm thick Al target. Laser spot sizes are 1 and 3 mm and energy is 20 mJ/pulse.

for the 3 mm spot size, and is much less than the Rayleigh wave for the 1 mm spot size.

Plotting the signal power of the Rayleigh over the body waves in figure 4.12 shows that the power carried by Rayleigh versus body waves decreases with intensity until about 2×10^8 W/cm^2 before leveling off. This behavior follows the same pattern as with the shear versus longitudinal wave magnitude ratio shown in figure 4.10.

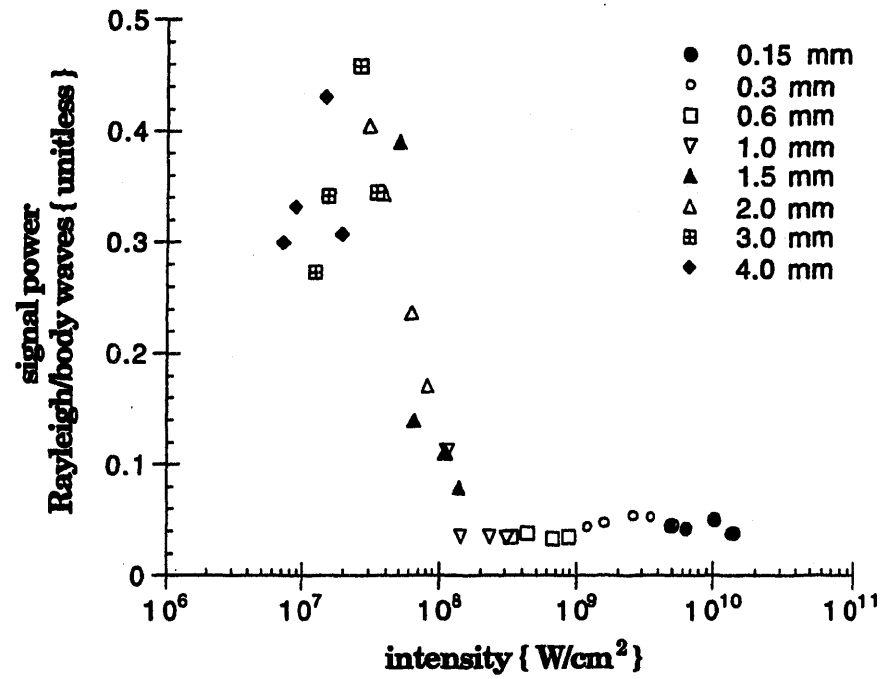

Figure 4.12 The ratio of the power in the Rayleigh over the longitudinal and shear waves is plotted versus intensity. Laser is focus to 8 spot sizes, at 4 different incident energies per spot.

4.4 Discussion

There are two striking features of the mechanical power versus incident intensity and energy data in figures 4.4 and 4.5. The first feature is that the stress power grows approximately quadratically with the incident power without saturating or tapering off. The second feature is that the stress power is relatively independent of spot size save that the baseline shifts an order of magnitude for spot sizes less than 1 mm. In this section, the baseline shift due to shock wave generation, the quadratic energy dependence and relative area independence are discussed first. The area

independence is a puzzling finding which deserves further research. Following the dependence developments, the effect of pressure on the stress power and the roll off of the shock versus target power ratio in figure 4.8 are discussed. The findings on the longitudinal, shear, and Rayleigh wave ratios complete the discussions.

4.4.1 Baseline Shift due to Ionization Gas Breakdown

The sources of the stress power that dominate these laser-material interactions are thermal expansion in the target, vapor recoil, and shock wave generation. Considering the data contained in figures 4.4 to 4.6, an effect of shock wave generation on the stress power is readily seen. A shock wave generated at the surface for laser spot sizes < 1 mm increases the baseline of the stress power by an order of magnitude over that for spot sizes ≥ 1 mm. The likely cause for the generation of this shock wave is the ionization breakdown of the air. However, the breakdown threshold for air above a target is complicated to predict [29]. Laser-induced breakdown of pure N_2 occurs at intensities on the order of 10^{12} W/cm^2, which is four orders higher than those observed [30]. However, the presence of a metal target can greatly reduce the ionization potential due to photoelectric and thermionic emission from the surface [31]. Thresholds for gas breakdown in front of a metal target can occur for power densities 10^8 W/cm^2 [32]. In these experiments, this threshold was reached at the lowest energy level of 20 mJ/pulse when the spot size dropped below 1 mm. With the 0.6 mm spot size, the lowest intensity was 3×10^8 W/cm^2 which appears sufficient for air breakdown in front of an aluminum target.

Once gas breakdown occurs, the air becomes a radiatively participating medium. Significant energy from the laser radiation can be absorbed depending on the incident wavelength and intensity, as well as the number density of the ions and electrons. Plasma shielding has been [33], and still is an actively studied area in laser-material interactions, and a more thorough discussion of shielding mechanisms is contained in chapter 5. Of importance in this work is that plasma shielding can have an effect on the stress power. Energy absorbed by the plasma increases its temperature and thus the kinetic energy of the gas particles. The increased kinetic energy adds to the pressure acting on the target surface, increasing the stress power. Energy initially present to thermally heat the material is transferred to mechanical energy. However, reducing the energy that reaches the surface reduces the amount of material entering the ablation plume. Therefore, with significant plasma shielding the recoil and pressure acting on the surface can be reduced. It should be noted that the plasma itself is radiating heat back to the target. Depending on the wavelength dependence of the material's absorption coefficient, that energy may be more readily absorbed. However, most of the radiant energy is lost to the surroundings due to geometric considerations, i.e. the solid angle from anywhere in the plasma to the laser irradiated zone is small with respect to the remaining hemispherical region.

4.4.2 Quadratic Dependence of Stress Power with Energy

The approximate quadratic dependence on the incident energy per pulse shown in figure 4.5 is consistent with a simple conservation of energy argument. Assuming that the stress power is the superposition of

the power from thermal expansion and the power induced by surface pressure, the stress power dependence on energy can be developed separately. For thermal expansion, let us assume a symmetric finite volume, $\forall$, in an infinite body receives a heat input, J, which raises its sensible heat such that

$$J = \forall \rho \, c \, \Delta T \ . \tag{4.28}$$

Assuming the strain ε is proportional to the change in temperature, or

$$\varepsilon = \alpha_\varepsilon \Delta T \tag{4.29}$$

then

$$\varepsilon = \frac{\alpha_\varepsilon}{\forall \rho \, c} J \ . \tag{4.30}$$

If it is further assumed that the stress restraining the expansion is proportional to the strain, and that the body is homogeneous and isotropic, then the stress power from equations (4.2) and (4.22) takes the form

$$P = 2 \, E \varepsilon \, \dot{\varepsilon} = E \frac{d}{dt}(\varepsilon^2) \tag{4.31}$$

where E is the proportionality constant with units of force per unit area. Making the final simplifying assumption that the properties remain constant, and substituting in (4.30) gives

$$P = E\left(\frac{\alpha_\varepsilon}{\forall \rho \, c}\right)^2 \frac{d}{dt}(J^2) = E\left(\frac{\alpha_\varepsilon}{\rho \, c}\right)^2 \frac{d}{dt}(j^2) \tag{4.32}$$

where j is the energy per unit volume. With $J = A \, f(t)$ where A is the maximum amplitude of the energy, then P is proportional to the square of the amplitude. For the excimer laser pulse where $f(t)$ is Gaussian in time, we would expect that the stress power would increase quadratically with energy due to thermal expansion. If the thermal expansion was not linear

with change in temperature, then P would diverge from a quadratic dependence on J. In the near field, material undergoing phase change could expand or contract at a rate independent of temperature. Phase-change expansion that occurs with Al would lead to a greater than quadratic dependence. Also, if the stress is not proportional to strain then the quadratic dependence of P on J would also diverge. When the stress versus strain dependence rolls off due to yield, the P versus J dependence would be less. However, for fully constrained and compressed material such that $\nu \rightarrow 1/2$, any addition of energy would cause P to exceed the quadratic dependence. There are certainly non-linear dependencies on expansion and stress with strain that occur in the near field. Add to that the uncertainty in property data, and the spread from 1.7 to 2.5 for m given in Table 4.1 is remarkably close to 2 predicted by linear thermoelastic theory.

For the stress power due to vapor recoil, a similar argument for a P versus J dependence can be made. Assuming the stress at the surface due to a pressure pulse p is proportional to the strain, then the stress power may be expressed as

$$P = 2\,C p \dot{p} = C \frac{d}{dt}(p^2) \qquad (4.33)$$

where C is a proportionality constant with units of area/force. To express P in terms of incident energy, the relationship between the mass flux, velocity, and energy must be known. If it is assumed that the pressure is proportional to the incident energy in time, then a quadratic dependence for P with J would again be found. It is extremely difficult to theoretically find a direct relationship between p and J, as discussed in § 4.2. However,

experimental data can be used to determine a constitutive relation. If the dependence of p on J is expressed as a power law

$$p = c\, J^n \tag{4.34}$$

and c is a function of area $f(a)$ where a is the spot size diameter, then (4.33) becomes

$$P = C f^2(a) \frac{d}{dt}(J^{2n}) \ . \tag{4.35}$$

The experimental data for shock power in figure 4.6 suggests that n = 1 within the range of 20 to 80 mJ, for each different area until the spot size became less than 0.6 mm. For the 0.15 and 0.3 mm spot sizes, the limited data is not quite linear, and n diverges slightly from 1. However, the pressure data also gives a quadratic dependence of the stress power on energy, within the limits of that found in Table 4.1.

4.4.3 Area Independence Puzzle

The relative area independence of the data in figures 4.4 and 4.5 is puzzling in light of the developments given above, and is still an open question. In this section, an argument will be presented as to why there should be a dependence, and then possible explanations for the results will be considered.

On first consideration, it would appear reasonable that the area would not affect the stress power, since the incident power is not changing with spot size. Yet power is not conserved, energy is. Considering thermal expansion, for low intensities the stress power is a very small fraction of the total power and the thermal transport of energy can safely be decoupled from the thermoelastic expansion. The assumptions that were made in

deriving (4.32) are reasonable for this case. However, equation (4.32) clearly shows that the stress power will increase as the energy per unit volume increases, as it must do as spot size is reduced. Although the AET transducer is essentially recording the total stress power in the target, integrating P over the total volume, such that

$$P_{tot} = \int_{V_{tot}} P \, dv \tag{4.36}$$

still leaves P_{tot} increasing with decreasing spot size.

The area independence also holds when the intensity is high enough to vigorously ablate material. If the change in pressure with area is chosen such that $f(a) \sim a^{-1/2}$, then after integration of (4.36) the total stress power would be independent of area. However, the function $f(a)$ suggested by the limited data in figure 4.6 is a decaying exponential centered about a maximum spot size, a_{max}, such that

$$f(a) \sim e^{-|a - a_{max}|} . \tag{4.37}$$

Even taking the first two terms of the series expansion of (4.37), P_{tot} still has an inverse dependence on spot size.

There are several possibilities for the area independence results that are considered here. First, it is possible that the area dependence is a complicated function of the total energy partitioning during ablation. While the data from the stress power alone does not appear to bear this out, work by Chan and Mao [34] shows similar area independence in intensity and emission data during ablation. Clearly, future work needs to be done to resolve this issue. Considered below is the possibility that the results are skewed due to systematic error in the experiment, or due to mode

conversion and reflections. Another possibility is that significant energy is carried by the Rayleigh surface wave which is not recorded by the AET.

It is possible that a systematic error exists in measuring the AET response. However, several factors were considered. The AET response is below its saturation limit, as seen in the quadratic increase with energy. Also, the response is not threshold dependent since the AET accurately recorded the baseline increase at 0.6 mm which was also measured by the Pinducer. The 20 μs time period over which the power is calculated is sufficiently long, since samples taken over 200 ms yielded similar results.

There are several possibilities that need to be considered in future work to determine if the observed area independence is physically valid. For the thin 2 mm samples used, multiple reflections occur in the 20 μs time period. At the target interfaces, significant mode conversion and reflection of the waves may take place which is angularly dependent. Initially the spot size is twice as thick as the target, and the angle of incidence that waves propagating from the surface will strike the target/transducer interface is small with respect to the normal. Wave reflection and mode conversion will be small for this case. Also, as seen in figure 4.10, more of the energy in the body is initially carried by shear waves for the largest spot sizes, which propagate slower with fewer reflections. However, as the spot size decreases to 1/10 the target thickness, the waves propagating from the source may strike the interface with a large angle of incidence, which then will be reflected and converted to other components. As seen in figure 4.10, most of the body energy is carried by longitudinal waves for the smallest spot sizes. A dispersion of frequencies and a dissipation of the strength of the waves could then occur.

Although the AET can detect both longitudinal and shear waves, losses will occur upon each subsequent reflection due to scattering and attenuation with distance. Recall from § 4.2 that body waves attenuate inversely with distance. In future work, using different thickness targets and different width transducers may verify if significant mode conversion, reflection, and attenuation exist to cause an apparent area independence.

A final consideration for area independence of the body waves is that the power carried away by the Rayleigh surface wave may vary inversely with area. The target and the transducer behave like a layered half-space for the smaller spot sizes, and up to 2/3 the mechanical energy can be carried by a Rayleigh wave [25] . However, figure 4.12 shows for the 3.85 mm thick aluminum target that as the spot size drops, less of the power is carried by the Rayleigh versus the body waves. Therefore, it is unlikely that the Rayleigh wave carries more power as spot size is reduced on the 2 mm thick target.

4.4.4 Pressure Effects on Stress Power

The development of a plasma and the generation of a shock wave is central to understanding laser-energy coupling to a solid target. In this section, the effect of a laser-induced pressure pulse on the mechanical stresses in the target are discussed.

As seen in figure 4.6, two competing factors affecting shock power are present. The power in the density wave increases linearly with energy and is exponentially dependent on the laser spot size as estimated by equation (4.37). As discussed in § 4.4.2 and 4.4.3, the response of the shock power should lead to a quadratic increase in stress power with

energy and initially an inverse increase with area until a maximum is reached, followed by a decline. From figures 4.4 and 4.5, the stress power is increasing quadratically with energy, but how much of that is due to a shock wave? Figure 4.8 shows that initially the power carried in the air is increasing faster than the stress power. At the lowest energies, a shock wave has not developed at all, and the density wave results from the thermal expansion of the target surface. As the energy is increased and vaporization is driving a shock wave, the individual stress components change with respect to each other. The first change is that the compressive portion of the longitudinal wave increases rapidly until it as large or larger than the tensile portion as seen in figure 4.9. Simultaneously, the shear to longitudinal ratio drops off. This drop off occurs when the spot size is $\leq$ 2 mm as seen in figure 10. Similarly, the ratio of the Rayleigh to body wave also decreases at the same point as seen in figure 4.12. It is not that the magnitudes of shear or Rayleigh are changing quickly. Indeed, the shear magnitude is dropping linearly with spot size, and the Rayleigh wave is losing magnitude by the square root of the spot size. Therefore, the increase in pressure due to shock generation primarily only affects the power carried by the longitudinal component of the stress power. Since the stress power is also affected by thermal expansion, the growth in stress power due to pressure is slower than the growth in the shock power due to pressure increases. This conclusion is supported by the 1.7 to 1 increase in the shock to target power ratio in figure 4.8.

At approximately 2 (10^8) W/cm^2 the shock to target power ratio begins to roll off, even though the shock power is growing at its fastest rate with energy, as seen in figure 4.6 for the 0.6 mm spot size. This roll off

implies that the stress power is growing at a faster rate than the shock power. At the same intensity levels and spot sizes, the ratios of shear to longitudinal and Rayleigh surface to body waves level off. Since this is the same intensity observed to cause gas ionization breakdown with a corresponding shock wave generation, it appears that plasma shielding is occurring. The plasma in the air absorbs some of the energy, and through shock wave generation, often called laser-supported detonation, transfers some of the power to mechanical stress power. The shock wave generated due to gas breakdown may occur away from the surface, spreading the loading on the surface from the previously more localized source. The wider loading acts similar to a larger spot size, thereby changing the ratio of shear to longitudinal and surface to body waves. As plasma shielding increases, less laser energy will make it to the surface and less material will be vaporized to support the expanding plume. Therefore, the shock power will be reduced, as is seen in figure 4.6 for the 0.3 and 0.15 mm spot sizes. Further work needs to be done to analyze changes to the stress and shock powers so that the effect of plasma-shielding on the amount of material ablated can be monitored using this technique.

4.5 Conclusion

While several researchers have used stress measurements to monitor the onset of ablation [6,7,11], this work is an introductory effort for understanding how mechanical stress power changes in a target and in the ambient medium during laser ablation of a solid material. At high intensities and short pulses, the stresses imposed on a target are substantial enough that stress power can not be ignored when considering an energy

balance for the laser-material interaction. This concern about the relative size of the stress power was in fact the motivation behind starting this study.

Several interesting results came out of this study. First, the dependence of the stress power on the incident laser energy basically followed a quadratic dependence, varying a small but significant amount from that predicted by a simplified linear theory. Second, the stress power data for a thin Al target shows a relative independence of spot size area, which is unexpected and needs further work to establish if it is true. Gas ionization breakdown was also observed to occur by monitoring the stress and shock power at an intensity that has been reported in the literature by different techniques. Moreover, the power in the density wave propagating in the gas medium versus the stress power in the target shows a saturation and roll off which corresponds with plasma shielding initiated by the gas breakdown. This work also demonstrated that the pressure at the surface of the target affects primarily the longitudinal component of the stress waves, as would be expected for a normal force acting on a surface. Most of the stress power is carried by the longitudinal wave at the higher intensities. Finally, at gas breakdown, the resulting plasma shielding transfers more energy into a measurable increase in the stress power.

Future research into monitoring the stress power during laser-material interactions will shed more light into its relative importance as laser intensities continue to increase. In chapter 5, monitoring stress and shock power is applied to studying plasma-shielding mechanisms at high-intensity laser-material interactions.

References

[1] C. R. Phipps and R.W. Dreyfus, "Laser ablation and plasma formation", *Laser Ionization Mass Analysis*, A. Vertes, R. Gijbels, and F. Adams (eds.), Wiley and Sons, New York (1993).

[2] F. Dahmani and T. Kerdja, Phys. Fluids B **3** (5), 1232 (1991).

[3] L. Balazs, R. Gijbels, and A. Vertes, Anal. Chem. **63**, 314 (1991).

[4] A.C. Tam and H. Coufal, Appl. Phys. Lett. **42** (1), 33 (1983).

[5] G. Koren, Appl. Phys. Lett. **51** (8), 569 (1987).

[6] W.R. Leung and A.C. Tam , Appl. Phys. Lett. **60** (1), 23 (1992).

[7] P.E. Dyer and R. Srinivasan, Appl. Phys. Lett. **48** (10), 445 (1986).

[8] G.A. Askar'yan and E.M. Moroz, Sov. Phys. JETP **16**, 1638 (1963).

[9] R.E. Beverly III and C.T. Walters, J. Appl. Phys. **47**, (8), 3485 (1976).

[10] F. Cottet and M. Boustie, J. Appl. Phys. **66** (9), 4067 (1989).

[11] K. Tonyali, L.C. Jensen, and J.T. Dickinson, J. Vac. Sci. Technol. A **6** (3), 941 (1988).

[12] C.S. Speight, L. Harper, and V.S. Smeeton, Rev. Sci. Instrum. **60** (12), 3802 (1989).

[13] J. Fournier, P. Ballard, P. Merrien, J. Barralis, L. Castex, and R. Fabbro, J. Phys. III France **1**, 1467 (1991).

[14] S.J. Davies, C. Edwards, G.S. Taylor, and S.B. Palmer, J. Phys. D: Appl. Phys. **26**, 329 (1993).

[15] A. Neubrand and P. Hess, J. Appl. Phys. **71** (1), 227 (1992).

[16] H. Wang, A.P. Salzberg, and B.R. Weiner, Appl. Phys. Lett. **59** (8), 935 (1991).

[17] F.J. Mayer and G.E. Busch, J. Appl. Phys. **57** (3), 827 (1985).

[18] J.C.S. Kools, T.S. Baller, S.T. De Zwart, and J. Dielman, J. Appl. Phys. **71** (1), 4547 (1992).

[19] F. Dahmani and T. Kerdja, Phys. Rev. A **44** (4), 2649 (1991), and F. Dahmani and T. Kerdja, Lasers Part. Beams **9** (3), 769 (1991).

[20] C.H Tsai and D.R. Olander, Phys. Fluids **30** (2), 386 (1987).

[21] R. Kelly and R.W. Dreyfus, Nucl. Instrum. Methods **B32**, 341 (1988).

[22] J.D. Anderson, Jr., *Modern Compressible Flow Second Edition*, McGraw-Hill Publishing Co. New York, (1990).

[23] G.F. Kinney, *Explosive Shocks in Air*, Macmilan Co., New York (1962).

[24] A.C. Green and P.M. Naghdi, Proc. Royal Soc. Lond. A, **432**, 171 (1991).

[25] K.F. Graff, *Wave Motion in Elastic Solids*, Ohio State University Press, Columbus, (1975).

[26] R.D. Woods, J. Soil Mech. Founds Div. Am. Soc. Civ. Eng. **94**, 951 (1968).

[27] K.G. Beauchamp and C.K. Yuen, *Digital Methods for Signal Analysis*, George Allen and Unwin, London (1979).

[28] H. Joseph Weaver, *Applications of Discrete and Continuous Fourier Analysis*, John Wiley and Sons, New York (1983).

[29] C.G. Morgan, Rep. Prog. Phys. **38**, 621 (1975).

[30] D.I. Rosen and G. Weyl, J. Phys. D: Appl. Phys. **20**, 1264 (1987).

[31] V. Kumar and R.K. Thareja,, Laser Particle Beams **10**, (1), 109 (1992).

[32] C. Boulmer-Leborgne, J. Hermann, and B. Dubreuil, Plasma Source Sci. Technol. **2**, 219 (1993).

[33] J.F. Ready, *Effects of High-Power Laser Radiation*, Academic Press, Inc., Orlando (1971).

[34] W.T Chan and X.L. Mao, Private communications. Lawrence Berkeley Laboratory (1993).

Chapter 5

The Influence of Plasma Shielding during Pico versus Nano-second Laser Ablation Depending on Gas Medium and Pressure

In this chapter, laser-material interactions at pulse lengths that are three orders of magnitude shorter than nano-second excimer laser ablation are investigated. Specifically, the influence of plasma-shielding on the coupling of laser energy to a target surface during pico-second pulsed laser-material interactions is demonstrated using helium (He) and argon (Ar) gas atmospheres. Using a combination of three different physical measurements, (i) the emission from the ablation products, (ii) the depth of craters left by ablation, and (iii) the stress and shock power in the target and atmosphere, reduced ablated mass is shown to occur in Ar versus He. Possible mechanisms of shock waves, multiphoton ionization, and plasma-shielding to explain these observations are discussed. For plasma-shielding to occur in the pico-second time regime, the existence of high-energy photoelectrons emitted from a Cu sample during the leading edge of laser pulse is postulated. These electrons form a plasma in the gas above the target via an inverse Bremsstrahlung process. The plasma absorbs part of laser energy, more so in Ar than He.

5.1 Introduction

The interaction of a high-energy pulsed-laser beam with a solid material has a wide range of applications including chemical analysis [1-4], thin-film deposition [5-7], microfabrication [8,9], medical applications [10], among others. Laser-material interactions involve processes that range from the heating of the target surface at low-power densities as discussed in chapter 1 and 2, to the complicated violent ablation of materials that occurs at high-power densities. Often it is desirable to minimize the extent of thermal heating, melting, or vaporization for many of these applications. For example, in laser-sampled chemical analysis and thin-film deposition by laser-ablation, extensive heating will influence the stoichiometry of the ablated vapor through preferential vaporization of the surrounding matrix [11-13] Also, in microfabrication techniques employing laser ablation, the precise removal of material is essential and thermal degradation of the surrounding material must be minimized. If a plasma forms during the laser pulse the incident energy may be absorbed by the plasma, thereby shielding the target [14]. Plasma-shielding can reduce the efficiency of laser-energy coupling and may lead to an enhancement of slower thermal processes by taking a high intensity source and transforming the heating source to a larger, less intense plasma.

Under what conditions plasma-shielding arises is of considerable interest for understanding how laser energy is coupled to a solid target. The mode of energy coupling depends on the laser wavelength, pulse

duration, energy per pulse, and power density at the surface, as well as the properties of the target and the gas medium. In chapter 4, the conversion of the laser power to mechanical power was considered. In this chapter, the influence of the gas medium on the laser energy coupling to the target is considered for laser pulses that vary by three orders of magnitude. How the amount of material removed and the stress and shock power change during the ablation of copper targets in a helium (He) and an argon (Ar) atmosphere with pico-second (ps) and nano-second (ns) pulsed-lasers are investigated. This effort results from the initial observation by W.T. Chan that the intensity of copper (Cu) emission, using an inductively coupled plasma - atomic emission spectrometer (ICP-AES) to monitor ps pulsed laser-sampling of copper targets, shows a significant increase in a He versus an Ar atmosphere. This change in intensity did not occur when sampling with a ns-excimer laser of approximately the same energy and wavelength in the UV spectral range. The increase in the ICP-AES signal also occurred using the near IR wavelength of 1064 nm of the pico-second Nd:YAG laser. This gas medium dependence suggests that the laser-energy coupled to the target changes dramatically.

In this chapter, the relation between the ICP-AES signal intensity and the gas medium is reported first. The intensity of the Cu I emission from the ICP-AES was measured for laser-sampling of copper at 248, 266, and 1064 nm in He and Ar. At one atmosphere the intensity increased 16.4 times in He compared to Ar when sampling with a pico-second laser at 1064 nm. To determine if the increase in intensity was due to a greater amount of material being ablated from the target, the

depth of the craters was measured after multiple laser pulses. The crater depth studies were extended to laser sampling of Cu in He and Ar at pressures ranging from 10^{-5} torr to one atmosphere. From the crater depth and carrier gas studies, anomalies such as particle size distribution and the effect of transport gases are found to negligibly affect the ICP-AES intensity. Instead, the increase in ICP-AES intensity is correlated with an increase in the material removed from the crater.

Next, to determine if the change in vapor emission from the target was due to changes in the power reaching the surface, the mechanical stress power in the target and the shock power in the medium were measured. The results show that there is little difference in stress power between He and Ar for the excimer laser, but significantly more power was coupled to the stress power in the target in Ar versus He for the ps-laser. The shock over stress power in the He versus Ar atmospheres was many times greater for the ps versus ns-laser indicating that more material is being removed.

In the discussion section, possible mechanisms for the increased material removal during pico-second laser-ablation in He versus Ar are considered: shock waves, multiphoton ionization, and plasma-shielding from inverse Bremsstrahlung absorption. The crater-depth data correlate with mass density of the gases, as does the propagation of the shock wave in a medium [15]. The shock and stress results, crater depth measurements, and the ICP-AES data shows that removal of particulate mass directly through pressure effects are small. For the wavelengths and intensities used in the experiments, why multiphoton ionization can be ruled out is discussed for the pico-second experiments. Inverse

Bremsstrahlung absorption due to thermal emission of ions, atoms, and electrons from the target during the pico-second laser pulses is also ruled out. However, if high-energy electrons are generated early in the pico-second laser pulse, then inverse Bremsstrahlung absorption due to collisions between the electrons and gas atoms can occur. Based on these conditions, plasma-shielding is a viable mechanism to describe the results.

Whether it is plausible for initial, high-energy electrons emitted from the target to initiate a plasma in the pico-second time scale is considered. To do so, a model developed by X.L. Mao based on inverse Bremsstrahlung absorption between the gas atoms and the fast electrons is presented. The basic concept is to solve for the electron density in the medium immediately adjacent to the surface, based on initial estimates of the energy and flux of the emitted electrons. The composition and pressure of the medium is taken into account to qualitatively show how the electron number density increases. The model behavior is compared to the measurements of the crater depth versus gas pressure, and shock versus target power and is found to have similar behavior. The generation of the fast electrons is discussed, and the chapter concludes that their presence, number density, and velocity distribution needs to be definitively determined to confirm that plasma-shielding occurs during pico-second laser ablation.

5.2 Experimental

5.2.1 Apparatus and Procedures

The experimental apparatus for all the work except the ICP-AES is shown in figure 5.1. A Questek model 2860 excimer laser at $\lambda = 248$ nm with a 30 ns pulse length and a Continuum 601C Nd:YAG laser at $\lambda = 266$ and 1064 nm with a 30 ps pulse length were used to ablate 1 mm thick by 2 cm diameter copper targets. The beams of both lasers were apertured to 6 mm diameter leaving the lasers. The power was controlled with a Newport 935-10 UV-grade high-power variable attenuator, and the energy was measured for each pulse with a photo-diode pick-off calibrated to a NIST traceable Molectron PD-104 pulsed-laser power meter. The pressure and gas-type for both the stress power and crater depth was controlled in a vacuum chamber fitted with gas flow controllers and pressure gages. The pressure was varied from 10^{-7} torr to atmospheric pressure. The laser beam was focused for both experiments through a 400 mm focal length lens to a diameter of 1 mm. The incident energy for the stress power work was nominally set to 3, 6, 9, and 12 mJ per pulse for the excimer and 9 mJ for the ps-laser. The shot to shot variation from the nominal value was recorded, and the all the energy data was normalized to the nominal value. The copper disk was mounted with a thin layer of Dow Corning high vacuum silicone grease to an acoustic emission transducer (AET) with a 1 inch diameter set 45% from normal. The laser beam was focused on the centerline of the AET at the surface of the target. A Valpey-Fisher model VP-1093 Pinducer transducer was set 9 mm from the target along the centerline to record the shock waves generated at the surface of the target. The data

from the AET, Pinducer, and photodiode was captured with a Tektronix 602A digitizing oscilloscope. The stress power is calculated according to the theory and method described in chapter 4.

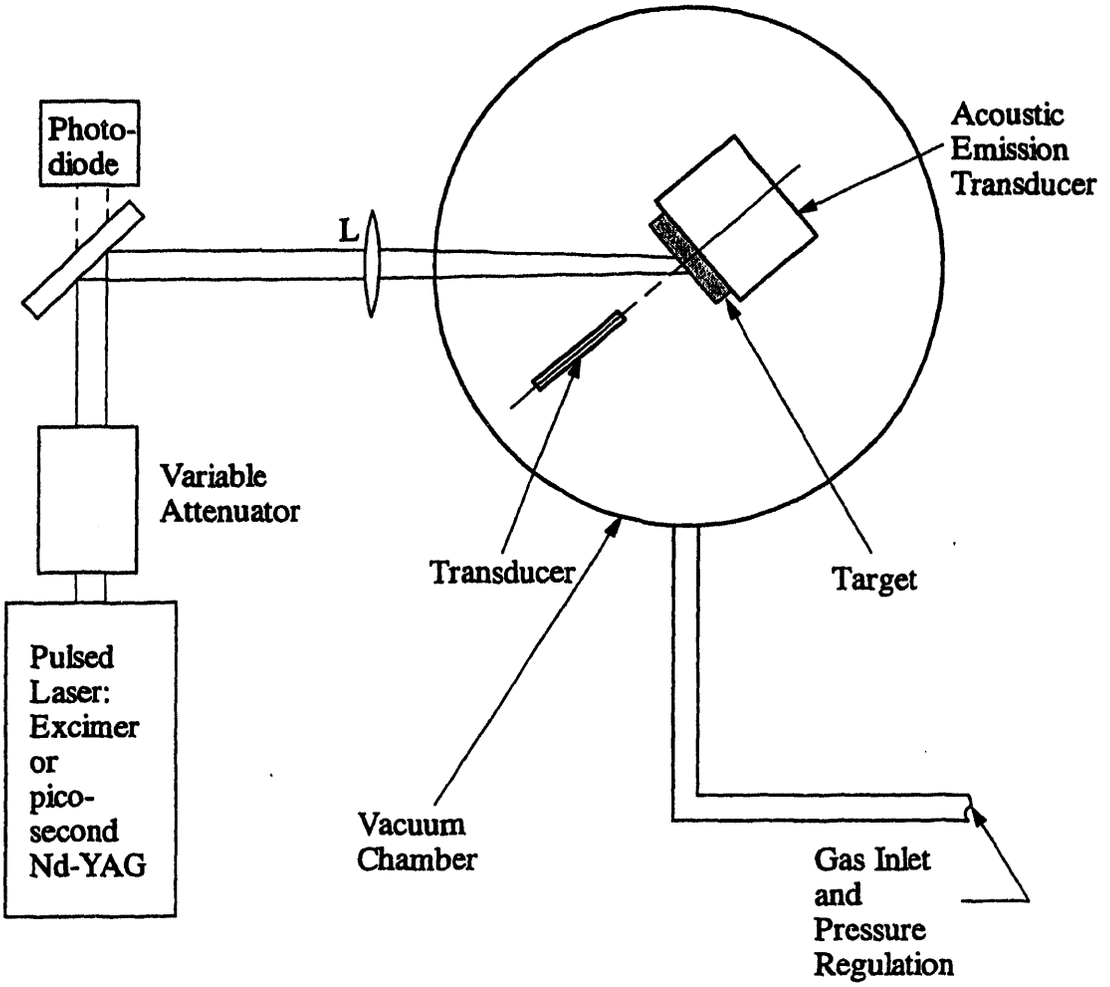

Figure 5.1 Schematic of experimental setup used for acquiring stress and shock power data as a function of gas medium, pressure, and laser wavelength, duration and energy. Focal length for L is 400 mm.

An ICP-AES with a photodiode array detector was used to monitor the material vapor during laser sampling of copper, by measuring the

intensity of the Cu I line at 327.4 nm. In this technique, the vapor products of ablation are transferred to inductively-coupled argon plasma which heats the ablation products until dissociation and ionization occurs [16]. The temperature of the argon plasma is such that singly ionized copper (Cu^+) dominates and very few ions are multiply ionized. The ratio of ions to neutrals is set by the ICP characteristics and remains constant, independent of the ablation process. The intensity of the Cu I line then is directly related to the Cu ions number density and thus to the amount of vapor products being ablated. In this experiment, a laser beam is focused onto the sample surface at normal incidence with a 200 mm plano-convex lens. The 30 ps-Nd:YAG and 30 ns-excimer lasers were used to study the effects of pulse duration on the interaction. An aperture of 6 mm diameter was placed between the excimer laser and the focusing lens to control the laser-beam spot size and energy; the energy after the aperture was 30 mJ. The energy of the ps-laser was 10 mJ at 266 nm and 15 mJ at 1064 nm. The lasers were pulsed at 10 Hz and 1500-3000 pulses were delivered to each location on the sample surface. As shown in figure 5.2, the sample is ablated in a gas-filled chamber. A stream of carrier gas delivers the laser sampled material to the ICP-AES. After passing through the chamber, the chamber gas (Ar or He) merged through a T-joint with the carrier gas (He or Ar) with the same flow rate. The merged gas (Ar + He) then flows to the central channel of the ICP torch, the usual configuration for sample introduction. This procedure ensures that the gas composition in the ICP is constant, independent of the gas atmosphere in the chamber. Therefore, the ICP temperature and excitation characteristics will be constant.

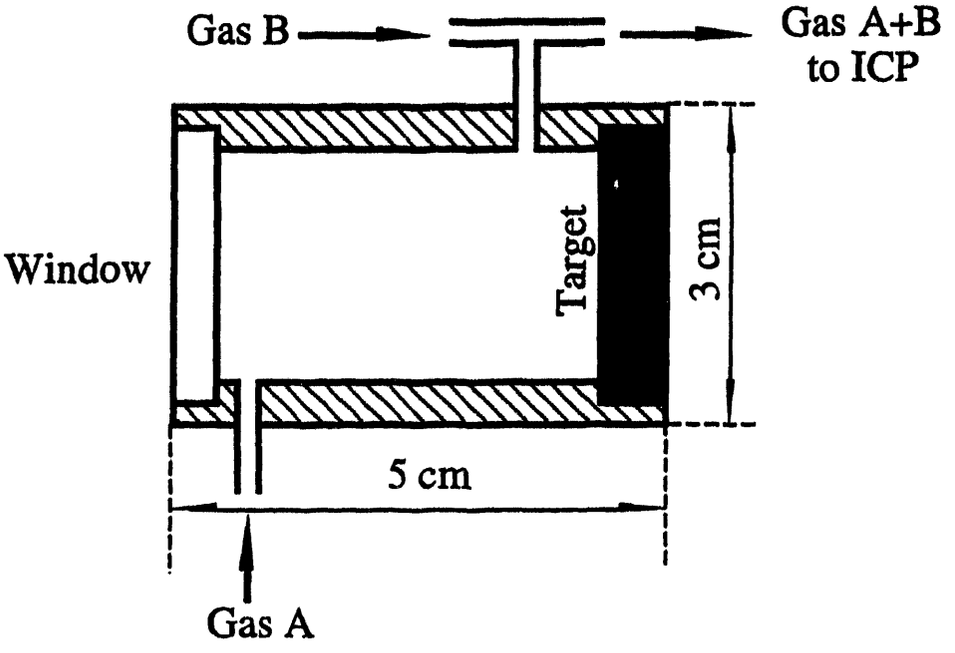

Figure 5.2 Diagram of gas flow configuration in the laser sampling chamber.

During repetitive-laser sampling, the typical temporal profile of the ICP-AES signal is a rapid rise in intensity, followed by a lower but steady plateau region [17]. The precision of the emission intensity during the steady region (~ 3% Relative Standard Deviation (RSD)) is better than that for single shot experiments (~ 50% RSD). The integrated emission signal obtained during this steady plateau region of the temporal profile was used as the data presented in this work. All reported emission intensity data are normalized to the copper intensity when sampling in pure Ar.

Power densities from 0.1 to 10 GW/cm^2 and 10 to 50 GW/cm^2, for the excimer and Nd:YAG lasers, respectively, were obtained by maintaining a constant pulse energy and varying the lens-to-sample distance. Power density was calculated using the laser spot size, pulse

energy, and pulse duration. The laser-spot area on the target sample was calculated based on the lens-to-sample distance. The calculated area was found to be within 10% of that observed using a microscope image of burn patterns, and the cross-sectional profile of the crater scanned with a profilometer.

Crater profiles from laser sampling of copper in He and Ar atmospheres at gas pressures ranging from 10^{-5} torr to atmospheric pressure were measured by surface profilometer. The incident angle of the laser beam was 45°. Each crater was produced by 1500 laser pulses with the same power density (~ 5×10^{10} W/cm^2). The crater and rim volume is calculated assuming that the crater is symmetric. Crater depths of 10 to 100 μm were developed at the incident spot, depending on the laser power density.

5.2.2 ICP-AES Experimental Results

The normalized ICP-AES Cu I emission intensities measured by W.T. Chan are given in Table 5.1 for the laser sampling of copper in He versus Ar. The gas atmosphere in the sampling chamber varied from pure Ar or He, to mixtures of Ar and He. For the 248 and 1064 nm wavelengths, note that the Cu I intensity is similar using pure Ar atmosphere in the sampling chamber with either pure Ar or Ar plus He as the carrier gas. Also, the gas atmosphere has little influence on the ICP-AES signal when the copper is sampled using the 30 ns pulses from the 248 nm excimer laser; the emission intensity was approximately the same using He versus Ar (1.3 versus 1.0). However, with the 30 ps-laser at $\lambda = 266$ nm, the ratio of intensity in He was 3.3 times that of Ar, which

shows pulse-length dependence for the laser-material interaction. Using the fundamental frequency of the ps-laser with $\lambda = 1064$ nm, the ICP-AES signal intensity was 16.4 times higher using He versus Ar in the sampling chamber. The final result to note in Table 5.1 is that when both Ar and He are present in the sampling chamber, the Cu I intensity changes little from Ar alone (1.2 versus 1.0). Without Ar in chamber, the emission intensity for He (16.4) was 13.7 times greater than when Ar and He (1.2) were mixed in the chamber. Therefore, the Ar in the atmosphere acts to suppress the ICP-AES signal over that of He alone.

Table 5.1

ICP-AES Cu I emission intensity from laser sampling of copper. The intensity is normalized to the intensity obtained in the atmosphere for each wavelength. The 248 nm wavelength was provided by a 30 ns excimer laser. The 266 nm and 1064 nm wavelengths were provided by a 30 ps Nd:YAG laser. The power density is 1.3 and 40 GW/cm^2 for ns-laser and ps-laser, respectively. The gas pressure is 1 atm.

Gas Atmosphere	Carrier Gas	Cu I (normalized)	Wavelength {nm}
Ar	Ar	1.0	248
He	Ar + He	1.3	248
Ar + He	Ar + He	1.3	248
Ar	Ar + He	1.0	266
He	Ar + He	3.3	266
Ar	Ar	1.1	1064
He	Ar + He	16.4	1064
Ar	Ar + He	1.0	1064
Ar + He	Ar + He	1.2	1064

5.2.3 Crater Spatial Profile and Depth Results

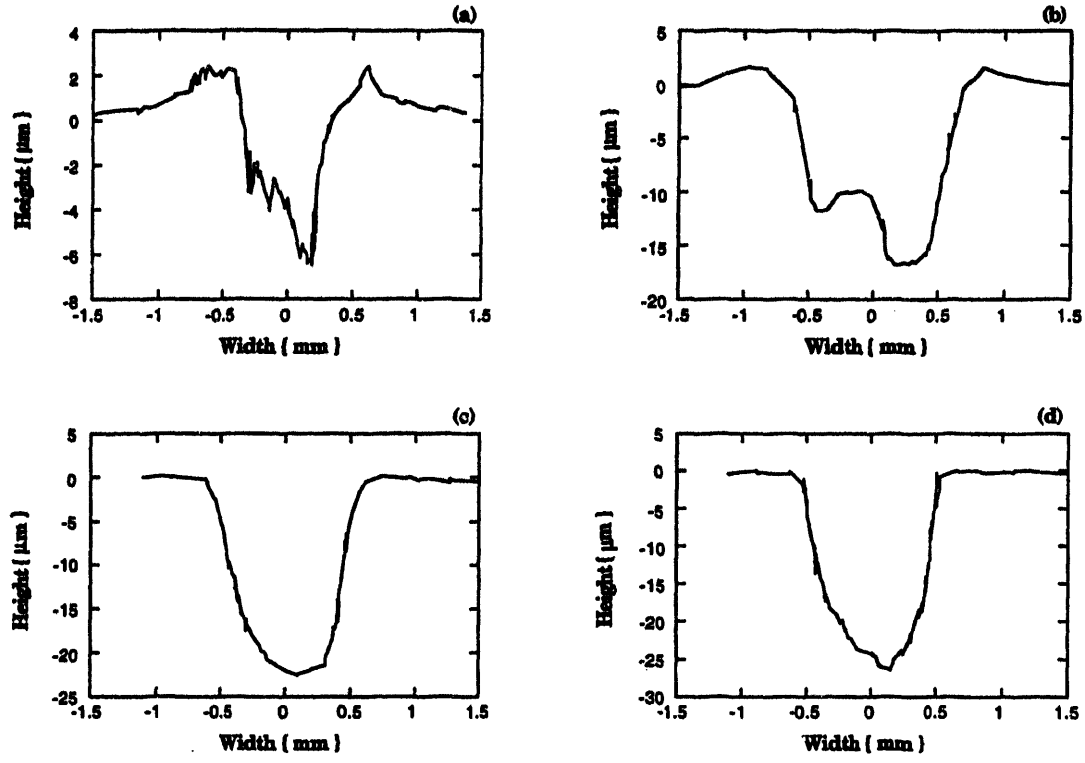

Figure 5.3 Cross sectional profiles of laser craters in copper targets created with the 30 ps-Nd:YAG laser at 1064 nm for (a) Ar at 760 torr, (b) He at 760 torr, (c) Ar at 10^{-5} torr, and (d) He at 10^{-3} torr.

In order to determine if the increased ICP-AES signal intensity for pico-second sampling in He versus Ar is due to increased material removal, the spatial profiles of the craters were measured. The cross-sectional profiles of the laser craters are shown in figures 5.3(a & b) at one atmosphere of pressure and in figures 5.3(c & d) at low pressures (< 10^{-3} torr), for Ar and He atmospheres, respectively. These craters were produced with the ps-laser beam at a 45° incidence and power

density of approximately 5×10^{10} W/cm^2. Only a minor difference in crater shape and volume between 45° and normal incidence was observed when the crater depth is small (< 100 μm). Note that the craters are deeper in the He atmosphere for the same number of pulses compared to the Ar atmosphere for both pressure regimes. However, as seen in figures 5.3(a & b) at one atmosphere the depth is over two times greater in He versus Ar, whereas the difference is smaller at low pressures. Also note that at one atmosphere of pressure, rims have formed around the craters, and at low pressure they have not. Most importantly, at one atmosphere the craters formed using He are much larger than those with Ar, and the increased Cu I intensity in He correlates to an increased laser-sampled volume in He versus Ar.

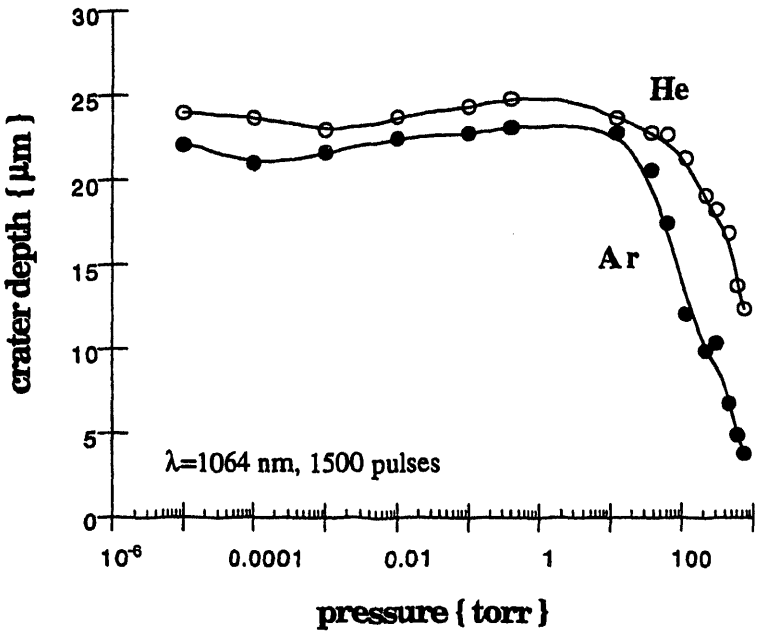

Figure 5.4 Plot of crater depth versus gas pressure after 1500 pulses from ps Nd:YAG laser with λ = 1064 nm. The laser energy is 15 mJ/pulse, and power density is 5×10^{10} W/cm^2.

To demonstrate the influence of pressure of the medium on the amount of material removed during laser sampling, a plot of crater depth versus gas pressure for He and Ar gas is shown in figure 5.4. For both He and Ar, crater depth is relatively independent of gas pressure lower than 10 torr. In Ar, the crater becomes shallower, reducing significantly for pressures higher than approximately 10 torr. A similar reduction is observed in He, except starting at higher pressure of approximately 100 torr. The appearance of a crater rim occurs at approximately the same pressure as the reduction of the crater depth. The volume of the craters and their rims are tabulated in Table 5.2 for $\lambda = 1064$ nm. As the pressure increases, the crater rim volume increases dramatically at 760 torr for He and 100 torr for Ar. The total mass of the material monitored by the ICP, however, can not be estimated from the difference between the crater volume and the rim volume, as there are numerous particles in the crater and surrounding area which cause the rim to be overestimated and the crater underestimated. Also, the density of the rim is smaller than that of the original solid.

Table 5.2

Crater and rim volume summary for laser sampling of copper with 1500 pulses from the 30 ps Nd:YAG laser, $\lambda = 1064$ nm, and energy = 15 mJ.

pressure {torr}	crater volume, 10^{-6} cm^3		rim volume, 10^{-6} cm^3	
	He	Ar	He	Ar
10^{-5}	14	13	0	0.3
10	13	14	0	0.6
10^2	16	7	0	7
760	8	1	4	5

5.2.4 Stress and Shock Power Results

The stress and shock power for ablation of a copper target versus pressure will be first presented for the 30 ns excimer laser with a 248 nm wavelength followed by those for the 30 ps Nd:YAG laser at both 266 and 1064 nm wavelengths. The excimer data is included so that a direct comparison of pulse length can be made for the UV wavelengths.

Figure 5.5 shows the signal power in the copper target being ablated by the excimer laser for a series of four energy levels from 3 to 12 mJ as a function of pressure. With an Ar atmosphere, the target power shown in figure 5.5(a) is basically flat from 10^{-6} torr up to atmospheric pressure for each energy level. A small dip is seen above 10 torr for the 9 and 12 mJ energy levels. For a He atmosphere, the target power is also flat, yet with more scatter in the data than for the Ar atmosphere. The mean target power is also slightly greater for the He versus Ar atmospheres at 9 and 12 mJ, with virtually no change at the lower energies.

The power in the shock wave during the excimer ablation is plotted in figure 5.6 as a function of pressure and gas type. As was done in chapter 4, the shock power is normalized to the stress power in the target. This normalization shows how the shock wave changes with respect to the stresses in the target as the energy is changed from 3 to 12 mJ. In the Ar atmosphere, the shock to target power ratio plotted in figure 5.6(a) remains at zero up to approximately 0.4 torr for all energy levels. At 10 torr, the ratio has already begun an exponential rise for the 9 and 12 mJ levels, with the rise just starting for the 6 mJ level. The

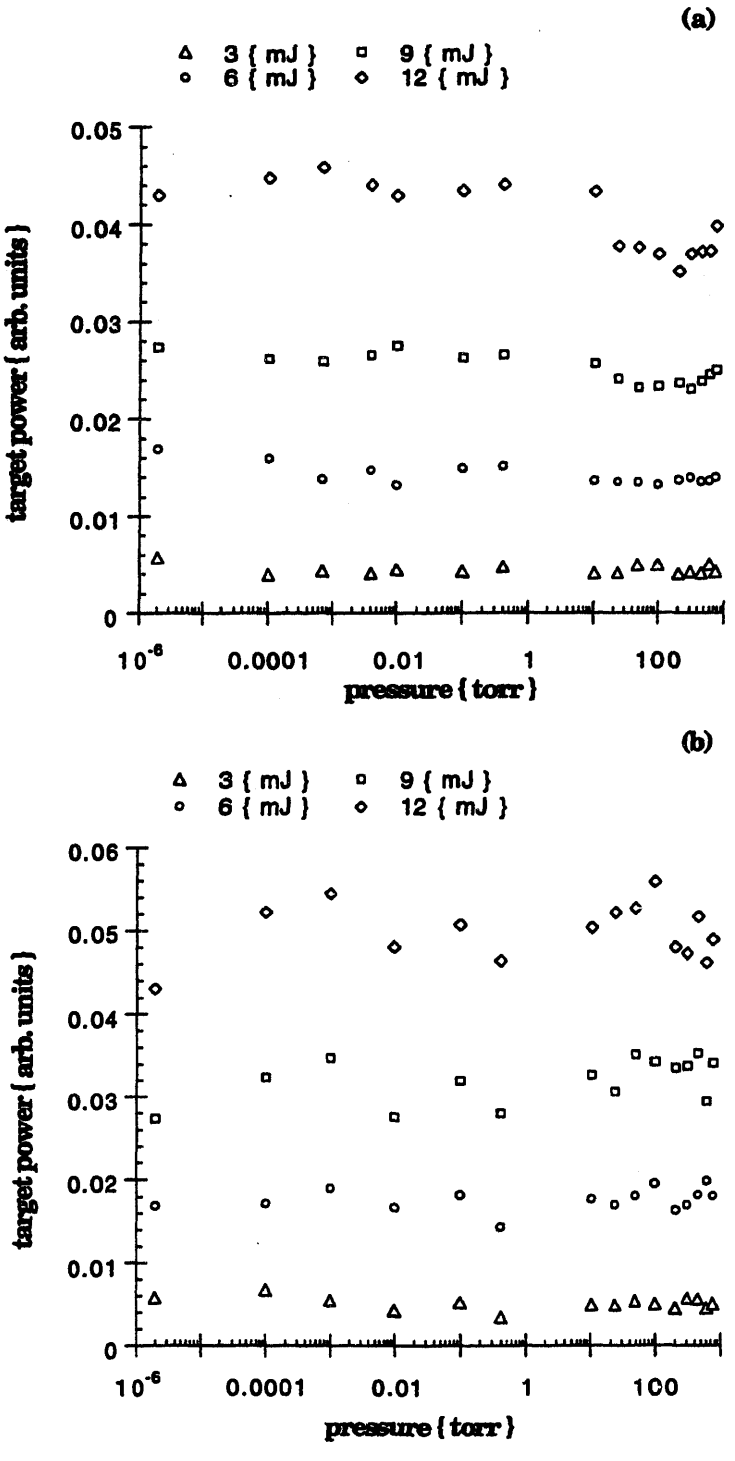

Figure 5.5 The signal power from the ablation of a copper target by a 248 nm, 30 ns excimer laser at 3, 6, 9, and 12 mJ/pulse as a function of the pressure of the ambient Ar (a) and He (b) atmosphere.

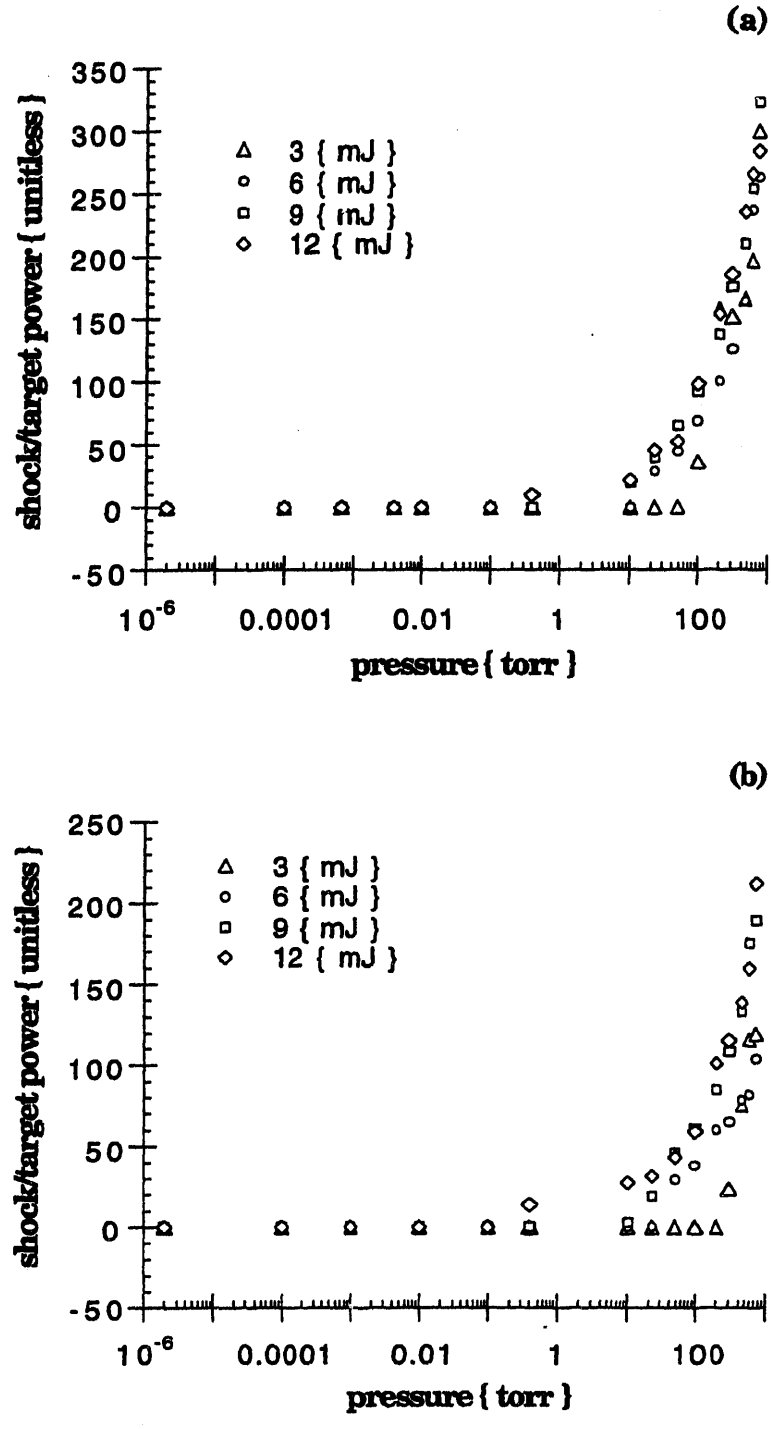

Figure 5.6 Power in shock wave normalized to power in copper target being ablated by a 248 nm, 30 ns excimer laser at 3, 6, 9, and 12 mJ/pulse plotted as a function of the pressure of the ambient Ar (a) and He (b) atmosphere.

rise for the 3 mJ series begins later at 50 torr. Note that the ratios all converge to the same levels as the pressure increases to 1 atm. In figure 5.6(b), the ratio plotted for the He atmosphere shows a similar response, except that the delay in shock onset is more pronounced at the lower energy levels, and they do not converge by 1 atm pressure. The magnitude of the ratio is also not as great as that in the Ar atmosphere, which ranges from 10 to 50% larger as the pressure increases. This increase is due to both a smaller stress power in the target and a greater shock power for the Ar atmosphere.

The results for the target and shock power due to ablation with the ps-Nd:YAG laser will be presented for two wavelengths, 266 and 1064 nm. The 266 nm results will be compared with the excimer data for 9 mJ/pulse and the ICP-AES data, and the 1064 nm will be compared with the crater depth and ICP-AES data in the following discussion.

The signal power in the target for both the Ar and He atmospheres is shown in figure 5.7 for (a) 266 nm and (b) 1064 nm wavelength as a function of pressure. In both figures, the target power is greater with an Ar versus a He atmosphere, increasing with pressure until at 1 atm the target power is 2 and 2.5 times greater for the 266 and 1064 nm cases, respectively. The ratio of the stress powers for He and Ar, P_{He}/P_{Ar}, is plotted in figure 5.8 for (a) 266 nm and (b) 1064 nm wavelength as a function of pressure. Even though there is a good deal of scatter for the Ar at 266 nm case, the trend for both is for the stress power to drop in a He relative to an Ar atmosphere as the pressure increases. For the 248 nm excimer irradiation, the stress power basically remained constant

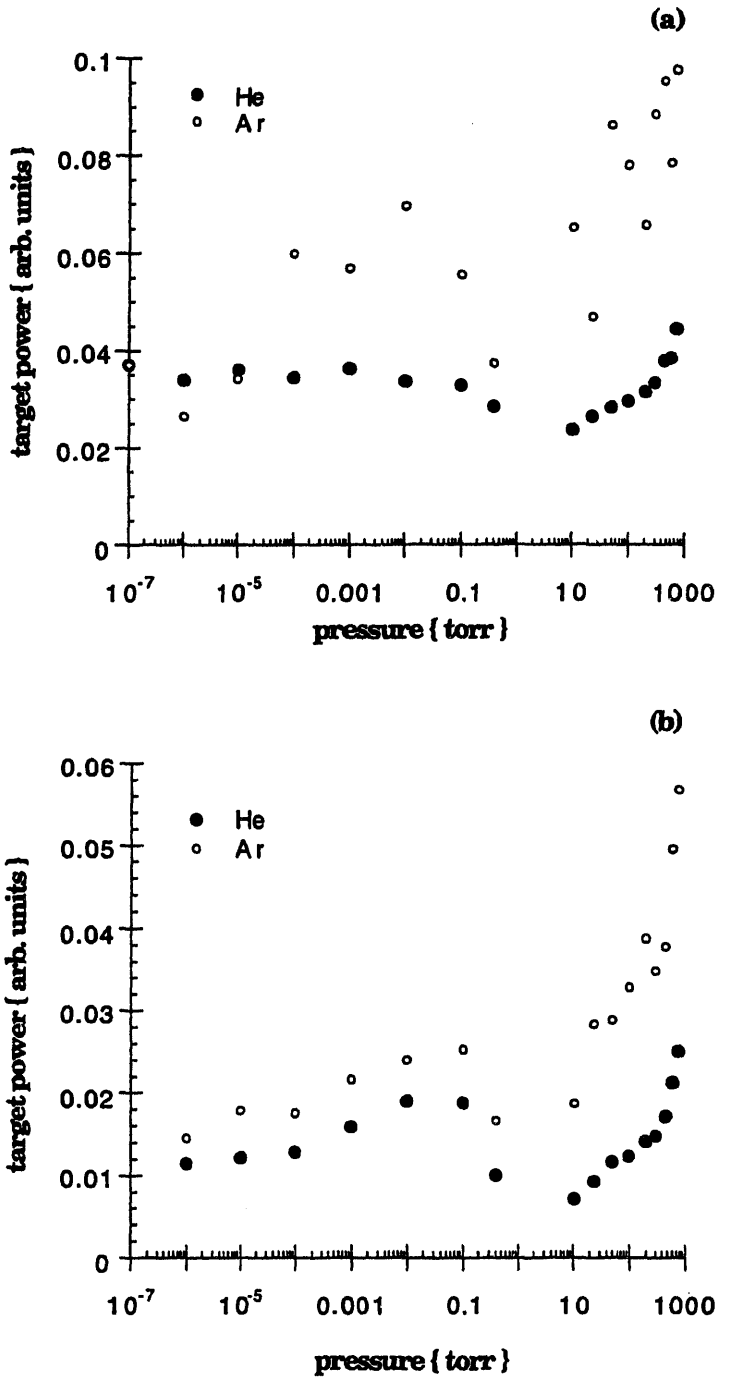

Figure 5.7 The signal power from the ablation of a copper target by a (a) 266 nm and (b) 1064 nm wavelength 30 ps Nd:YAG laser at 9 mJ/pulse as a function of the pressure of the ambient Ar and He atmospheres.

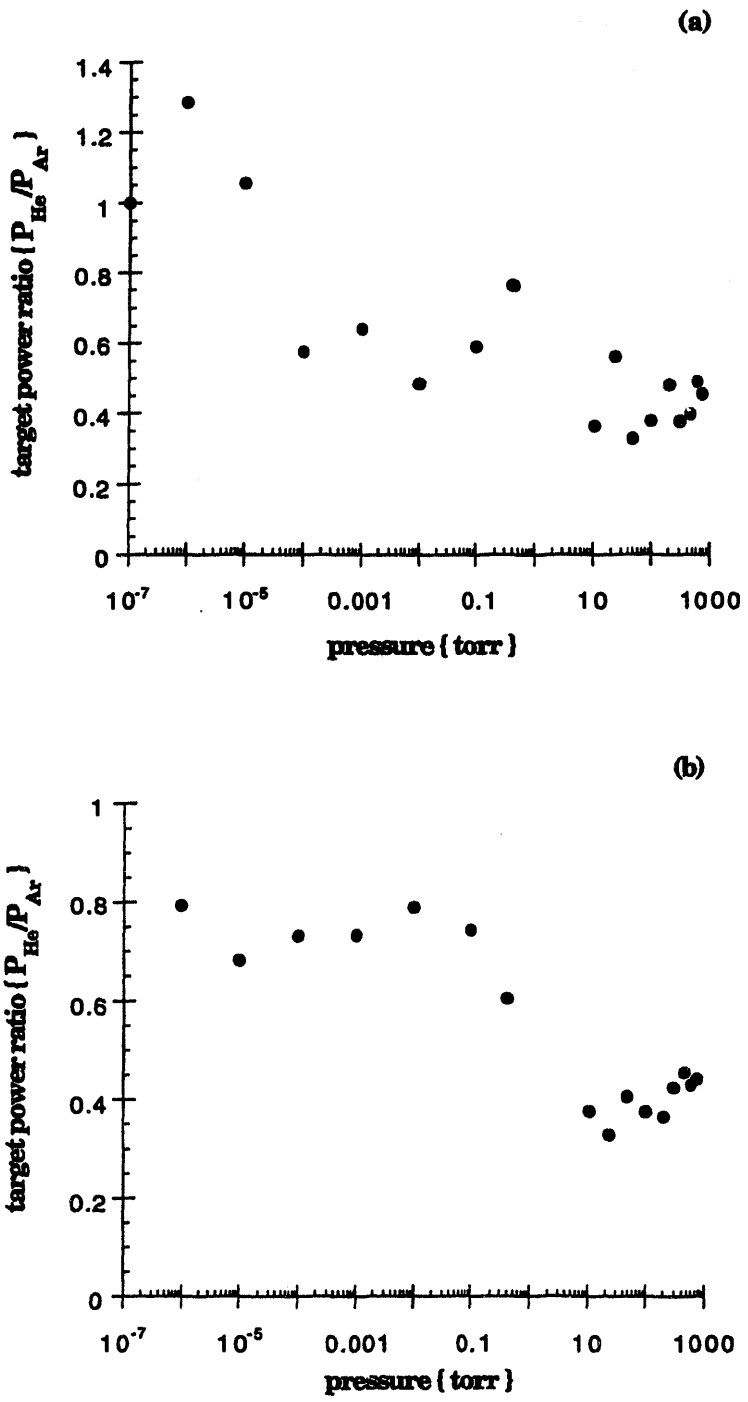

Figure 5.8 The ratio of target power in He versus Ar atmospheres during the ablation of a copper target by a (a) 266 nm and (b) 1064 nm wavelength 30 ps Nd:YAG laser at 9 mJ/pulse as a function of the pressure.

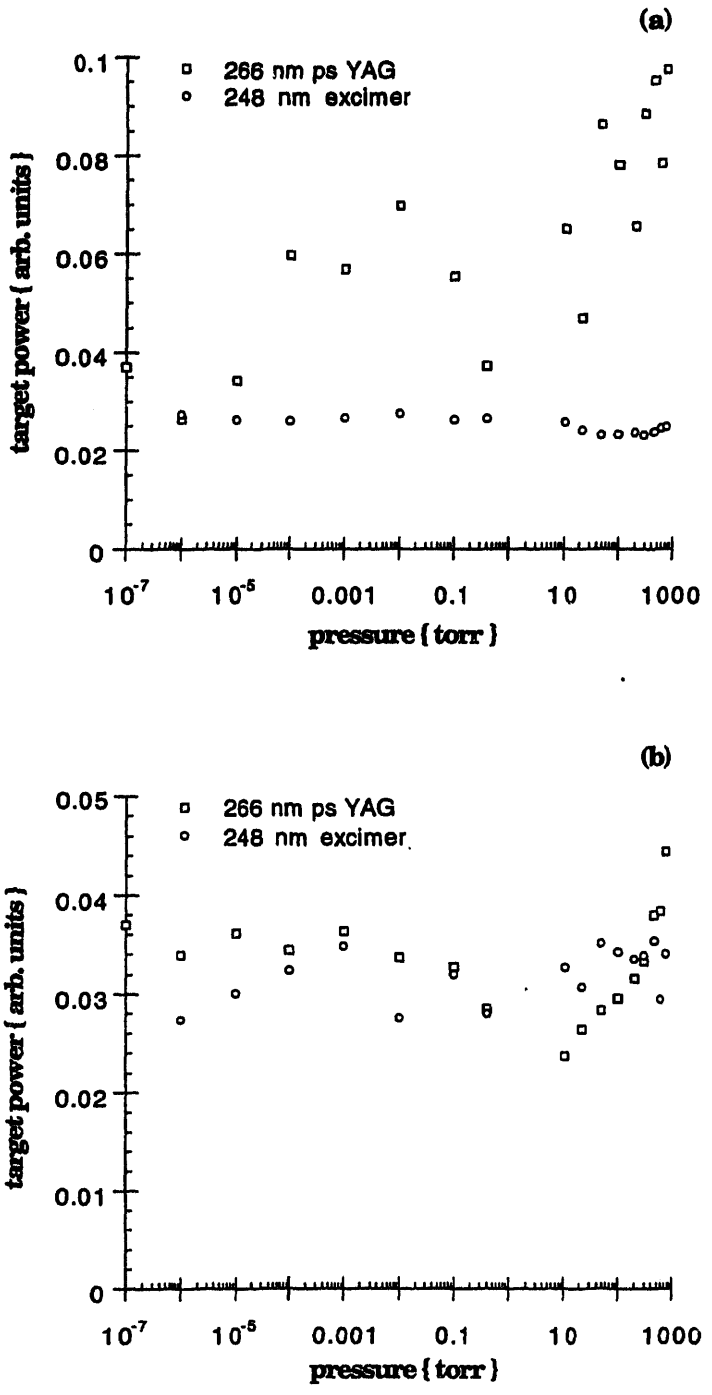

Figure 5.9 The signal powers in (a) Ar and (b) He atmospheres during the ablation of a copper target by a 266 nm wavelength 30 ps Nd:YAG laser and a 248 nm wavelength 30 ns excimer laser at 9 mJ/pulse as a function of the pressure.

with pressure, and the He stress power was slightly larger than with Ar which is opposite the results for the ps-laser at 266 nm. In figure 5.9, the target power is plotted for the ps-Nd:YAG and ns-excimer laser at 9 mJ per pulse for both. In figure 5.9(a), the ps-irradiated target power increases markedly with pressure for the Ar atmosphere, until it is three times greater than the ns case at 1 atm. But in the He atmosphere, figure 5.9(b) shows that the two target powers are approximately equal, even though the intensity is three orders of magnitude higher for the ps versus ns-lasers.

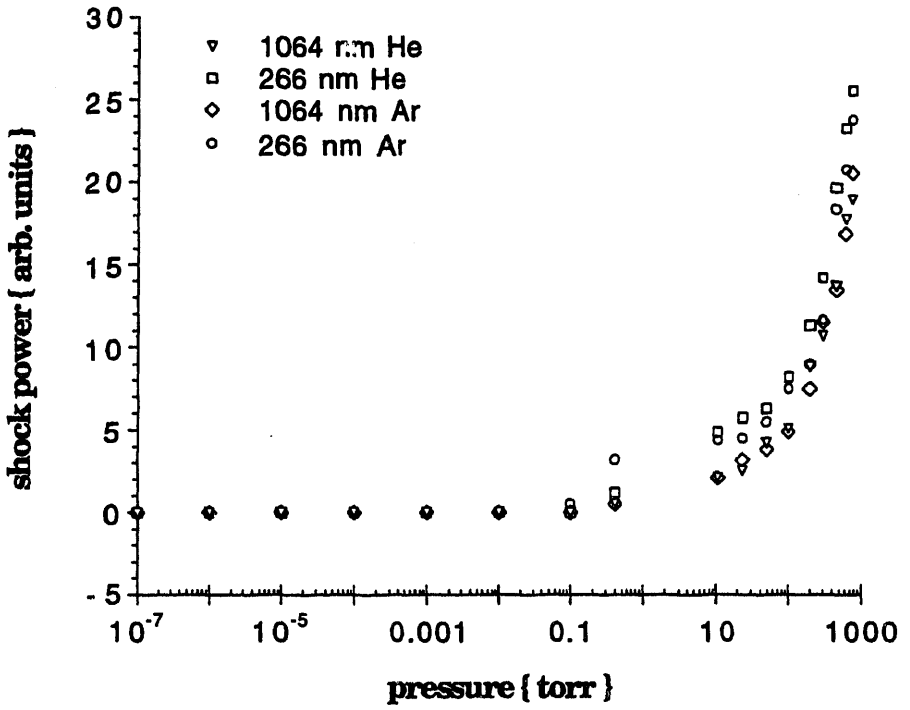

Figure 5.10 Power in shock wave for copper target being ablated by a 266 and 1064 nm wavelength 30 ps Nd:YAG laser at 9 mJ/pulse plotted as a function of the pressure of the ambient Ar and He atmospheres.

The shock powers generated by the ps-laser are shown in figure 5.10 as a function of pressure, for both wavelengths and gases. As for the excimer laser, shock waves are not measurable below 0.1 torr. Above 0.4 torr, shock waves are generated with the magnitude being slightly greater for the Ar versus the He atmosphere for both wavelengths. As the pressure increases, the power of the shock waves grow exponentially and all converge to the same values. In figure 5.11, the shock power is normalized against the target power to see how the shock power changes with respect to the stress power in the target. This

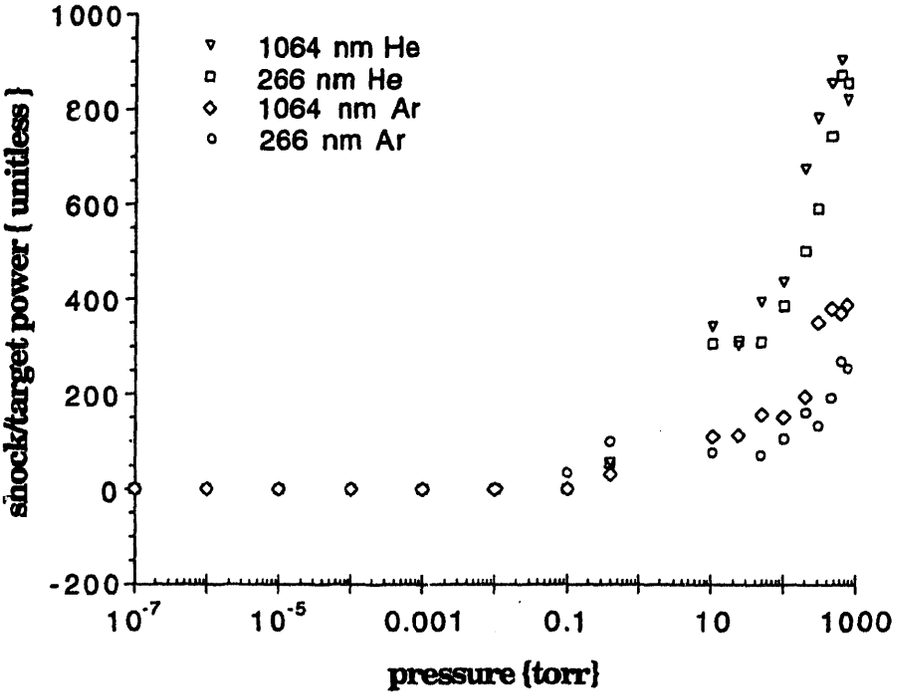

Figure 5.11 Power in shock wave normalized to power in copper target being ablated by a 266 and a 1064 nm wavelength 30 ps Nd:YAG laser at 9 mJ/pulse plotted as a function of the pressure of the ambient Ar and He atmospheres.

figure shows a distinct difference between in the shock powers between the gases at the same energy level. The shock/target power in He is greater at both 266 and 1064 nm wavelengths than in Ar. The difference is approximately six times greater at 10 torr and 4 times greater at 1 atm. The greater power in He versus Ar for the ps-laser stands in contrast with the case shown in figure 5.6 for the 30 ns excimer laser. Moreover, the magnitude of the ratio is three times larger in He and is approximately the same in Ar for the ps versus ns-lasers.

5.3 GAS IONIZATION MODEL

5.3.1 Model Development

A simplified physical model developed by X.L. Mao is presented based on an inverse-Bremsstrahlung absorption mechanism between fast electrons and the gas medium as a possible explanation for the initiation of a plasma above the target surface and the consequent shielding of the laser beam. The model assumes the existence of high-energy electrons on the order of 100 eV at the copper surface generated early in the pico-second laser pulse. The source and initial conditions of the electrons will be discussed later. These fast electrons absorb the laser photons during collisions with the gas medium through an inverse Bremsstrahlung process, developing an ionized plasma of the gas species over the target surface. The extent of plasma development through a change in ionization fraction depends on the properties of the gas. The model is used to calculate the electron density adjacent to the surface versus the gas pressure for Ar and He.

The energy of electrons is given by [18]

$$\varepsilon = \frac{3}{2} n_e k T_e + n_e k \Theta_I \qquad (5.1)$$

where n_e is the density of the electrons adjacent to the surface, T_e is electron temperature, Θ_I is the ionization energy of the gas atmosphere, and k is the Boltzman constant. The first term on the right hand side of equation (5.1) is the average kinetic energy, and the second term is the potential energy relative to a zero-energy reference state. The change of electron energy is equal to the sum of the energy gain via inverse-Bremsstrahlung and the energy loss to the gas atoms and ions via elastic collisions [18],

$$\frac{d\varepsilon}{dt} = \frac{3}{2} n_e k \frac{dT_e}{dt} + \frac{3}{2} k \left(T_e + \frac{2}{3} \Theta_I \right) \frac{dn_e}{dt} = k_L I - \frac{3}{2} n_e k (T_e - T_a) \nu_{tr} \qquad (5.2)$$

where ν_{tr} is the effective collision frequency for energy transfer between the gas species and electrons, T_a is the temperature of the gas atoms and ions, and k_L is the absorption coefficient of the laser radiation with intensity I. Defocusing of the laser intensity induced by fast electrons is neglected due to the small length scale (< 100 μm) in pico-second time region. k_L is expressed as [18]

$$k_L = \frac{3.7 \times 10^8}{\sqrt{T_e}\,\omega^3} Z^2 \left[\exp\left(h\omega / kT_e \right) - 1 \right] n_e n_i + \frac{e^2 \nu_c n_e}{\pi m c \omega^2} \qquad (5.3)$$

where ω is the laser frequency (Hz), Z is the ionic charge (Z=1), m is electron mass, e is the electron charge, c is the speed of light, and n_i is the density of ions. The electrons gain energy principally by electron-ion and

electron-atom inverse Bremsstrahlung, which are represented by the first and second terms in equation (5.3), respectively. The electron-atom collision frequency is [18]

$$\nu_c = n_a \sigma_c \sqrt{\frac{8kT_e}{\pi m}} \tag{5.4}$$

where σ_c is the electron-atom collision cross section and n_a is density of gas atoms.

The rate of change of the electron density representing the ionization and recombination process [18] is given by

$$\frac{dn_e}{dt} = \alpha_I n_a n_e - \beta_R n_i n_e^2 \tag{5.5}$$

where

$$\alpha_I = C_I \sqrt{kT_e} \exp(-\Theta_I / T_e) \tag{5.6a}$$

and

$$\beta_R = C_I \left[2 \left(\frac{2\pi m}{h} \right)^{3/2} \left(\frac{g_i}{g_a} \right) kT_e \right] \tag{5.6b}$$

with C_I equal to 0.015 $cm^3 s^{-1} erg^{-1/2}$ and 0.0015 $cm^3 s^{-1} erg^{-1/2}$ for Ar and He, respectively. C_I is an empirical constant which is estimated from ionization cross section data [19], and g_i and g_a are the degeneracy of ionic and atomic ground states. g_i/g_a is 1 and 0.727 for He and Ar, respectively. The change of ionization rate due to multiphoton absorption is neglected in this model, which is discussed in the next section.

Let the initial density of gas atoms be n, then

$$n_i = n_e - n_e(0) \tag{7a}$$

and

$$n_a = n - (n_e - n_e(0)) \tag{7b}$$

where $n_e(0)$ is the initial electron density, and n is gas atom density. n relates to gas pressure as $P = nkT_i$ assuming Ar and He are idea gases. T_i is the initial gas temperature.

5.3.2 Model Results

The electron density and electron temperature can be evaluated from equation (5.2) and (5.5) if the initial conditions are known. The initial energy and density of the electrons are taken from values found in the literature to obtain an order of magnitude estimate. The current density of high-energy electrons has been measured at 10^3 A/cm^2 for a laser power density of 1 GW/cm^2 [20]. The energy of fast electrons emitted from a gold surface using a ps-laser with a power density of 20 GW/cm^2 was reported to be 600 eV (velocity ~ 1.5 (10^9) cm/s) with an applied extraction field [21]. The work functions for gold and copper are similar at 5.1 eV and 4.65 eV, respectively. The magnitude of the energy of the fast electrons from copper is assumed to be of the same order as that of gold. From electron current density and energy, the initial values of the electron temperature is $T_e(0)$ = 5 (10^6) K and the density is $n_e(0) = 10^{17}$ cm^{-3}. The laser power density is 5 (10^{10}) W/cm^2, assuming a square pulse duration of 30 ps. The plasma densities of He and Ar at different pressure after 20 ps are evaluated from equations (5.2), (5.5), and (5.7) by the Runge-Kutta method, and

are shown in figure 5.12. The energy calculated from the equations is several eV. Although the exact initial value of n_e is not known, the trend for the ionization rate versus pressure is independent of the initial value. The crater depth behavior data shown in figure 5.4 is included in figure 5.12 for comparison to the model. The change in electron density with pressure for the He and Ar atmospheres shows a similar behavior as the crater depth measurement. That is, as the pressure increases the electron density increases in the Ar atmosphere more quickly than in He.

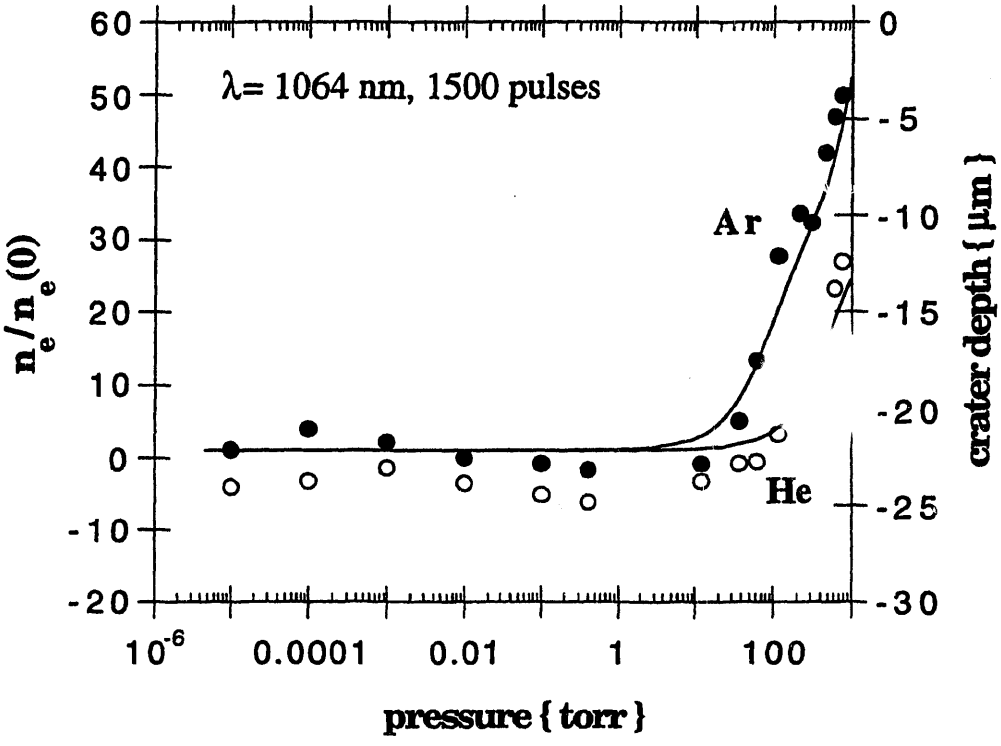

Figure 5.12 Plot of crater depth and electron density ratio versus gas pressure for ps-Nd:YAG laser with λ = 1064 nm. Solid curves correspond to the simulation of the change in ionization versus Ar and He gas pressure based on fast electron emission and inverse Bremsstrahlung, assuming initial electron temperature $T_e(0) = 5\ (10^6)$ K, and initial electron density $n_e(0) = 10^{17}$ cm^{-3}.

5.4 Discussion

5.4.1 Detection Methods

The three different physical detection methods, (i) ICP-AES emission, (ii) crater depth, and (iii) stress and shock power used in the experimental work all showed significant differences in the ablation response of copper in He versus Ar for the pico-second laser. However, similar changes were not seen for the nano-second laser using the first (i) and third (iii) methods. Each detection method will be discussed in above order, with the data complementing each other to show the effect of plasma shielding in the pico-second time regime.

The ICP-AES data shows a clear effect of the gas medium for the pico-second laser sampling of copper. The intensity ratio was approximately 3.3 times larger in He versus Ar at 266 nm, compared with the intensity ratio using 1064 nm wavelength which was 16.4 times larger. The first concern was to determine if the increase was an artifact of the ICP-AES response. By ensuring that the gases entering the ICP were a constant mixture, fluctuations in the data due to gas composition were avoided. As shown in the data using pure Ar versus Ar plus He as the carrier gas, little fluctuations were observed. When Ar and He were mixed in the sampling chamber, the results varied very little from Ar alone. The Ar, therefore, dominates the laser sampling, indicating that the phenomenon observed is related to the gas composition during the laser material interaction.

Since large particles and sputtered droplets are transported less efficiently in ICP sampling than particles smaller than 5 microns [22,23], a shift in particle size distribution can lead to a change in the emission intensity ratio. It is also possible that the particles/vapor is transported more efficiently through a less dense He plasma. In order to confirm that the increased ICP-AES signal intensity from laser sampling in the He medium at one atmosphere pressure is not due to particle-size distribution, the crater's spatial profile is measured. The data verify that more material was ablated from the crater in He versus Ar, and that the enhanced ICP-AES intensity is not due to transport phenomena.

For the nano-second excimer laser pulses, the stress power measurements shown in figure 5.5 showed little change from Ar to He. At the higher 9 and 12 mJ energy levels, the stress power in the target decreased as the shock wave developed above 10 torr in pressure. In He, a similar decrease was not observed, though it could have been obscured by the scatter in the data. The decrease in stress power in the target, however, corresponds to the generation of the shock wave seen in figure 5.6. The shock waves start sooner and at a lower energy level in Ar versus He, suggesting that even in the nano-second scale there is an increased interaction of Ar with the laser beam, particularly at the higher intensities. This small change was also observed with the ICP-AES data given in Table 5.1 which showed a 1.3 to 1 ratio in the Cu I normalized intensity for He to Ar indicating greater material was removed as vapor in He than in Ar.

For the pico-second Nd:YAG laser, the stress power data in figure 5.7 showed large differences between the Ar and He atmospheres

for both UV and IR wavelengths. With a He atmosphere, the response followed a similar pattern for both 266 and 1064 nm wavelengths, with less scatter in the data than for Ar. The stress powers at low pressures were basically the same between the gases, but were about half as large at 1064 versus 266 nm wavelengths. This decrease is to be expected, since copper is a good reflector in IR, but is relatively black in UV. In both gases, though, the ratio of the power between He and Ar dropped as pressure increase as shown in figure 5.8, indicating that more power is coupled mechanically to the target in Ar versus He as pressure increases. When comparing the stress power between the nano and pico-second time regimes, figure 5.9 shows that more of the incident power is present as stress power for the 266 nm ps laser ablation in Ar, with the other cases being approximately the same.

To determine the source of the increased stress power in the target for the Ar versus He atmosphere, the magnitude of the shock power is considered. As discussed in chapter 4, the strength of the shock wave is affected by the mass flux leaving the surface and the temperature of the ablation products. The same pressure behind the shock front can be reached by an increased mass flux and lower temperature, or vice versa. Without the radiatively participating medium which occurs during plasma shielding, the mass flux and temperature are directly linked and vary together. With plasma shielding, the mass flux can be reduced at the same time the temperature of the plasma increases. Figure 5.10 shows that the overall power in the shock waves converge to the same value by 1 atm for both gases. Yet, figure 5.11 shows that the shock/target power increases greatly in the He versus Ar atmosphere. Combining the data

from the ICP-AES that there is a greater mass of Cu ablated in a He versus Ar atmosphere with the increase shock over target power suggests that there is a greater mass flux leaving the surface in He, and there is a higher temperature in the plasma in Ar. Future work to determine the temperatures in the expanding plumes can verify this hypothesis.

5.4.2 Mechanisms

To explain the increased material ablated in He versus Ar as a function of pressure, three possible mechanisms are considered: the presence of shock waves, multiphoton ionization, and plasma-shielding.

When a shock wave in the gas is set up by laser ablation at the surface of the target, melt produced by heating can be ejected from the crater with a large range in particle sizes [24-26]. If shock is a major mechanism for material removal in the experiments, then shock waves should correlate with the crater depths that were observed. But the data in figure 5.10 shows that the shock wave magnitudes are approximately the same at 1 atm and are two times larger in Ar versus He at 10 torr. However, the ICP-AES emission increases during the pico-second laser sampling in He versus Ar and the crater depth in He is twice that of Ar at one atmosphere and are the same at 10 torr. These inconsistencies show that shock effects can not be the dominant mechanism for material removal in these experiments.

If significant multiphoton ionization of the gases occurs, then a preferential change in transmitted energy to the target may occur depending on the composition of the atmosphere. The cross section for multiphoton ionization, as well as the energy required for excitation,

differ between He and Ar, with Ar being more easily ionized. Multiphoton ionization is also dependent on wavelength. At the shorter wavelength of 266 nm, the rate of multiphoton ionization is greater than at 1064 nm, since fewer number of photons n are required for ionization. Yet the intensity ratio was approximately 3.3 times larger in He versus Ar at 266 nm, compared with the intensity ratio using 1064 nm wavelength which was 16.4 times larger. If multiphoton ionization dominates, the electron density is linearly proportional to the intensity, I, and pulse width, t_p, given by $N\sigma_x I^n t_p$ [27]. Here, N is gas density and σ_x is the generalized cross section for multiphoton ionization. The most easily ionized case by multiphoton absorption would be Ar at one atmosphere with the excitation laser wavelength at 266 nm. For this case $n = 4$ and $\sigma_x = 3.7\ (10^{-38})\ cm^8/(W^4s)$ [28]. Using the intensity in the experiments of $I = 5\ (10^{10})\ W/cm^2$, this gives an electron density of $8\ (10^{-6})N$. Therefore, the multiphoton ionization rate is very small, even using the UV wavelength in Ar for the sampling conditions. Using results from Dewhurst [29] for multiphoton ionization, the threshold for gas breakdown at 1 atm is $2\ (10^{14})\ W/cm^2$ and $10^{14}\ W/cm^2$ for He and Ar, respectively. The laser intensity in the experiments is only $5\ (10^{10})\ W/cm^2$. Therefore, multiphoton ionization effects are negligibly small in the pico-second regime of the experiments.

Multiphoton ionization can play a role during the nano-second pulse experiments. It appears that the insensitivity of the excimer stress power data and the ICP-AES signal to the gas atmosphere using the 248 nm excimer laser compared to the 266 nm ps-laser data is due to the laser pulse duration. In the nanosecond time regime, the ejected copper atoms

and ions from the target have traveled about 100 microns from the surface [30,31]. These atoms and ions can also form a plasma over the surface, shielding the latter part of the ns-laser pulse. This vapor is mainly composed of copper ions instead of Ar or He ions because the ionization potential of copper (7.724 eV) is significantly less than that of Ar and He. The photon energy of the excimer laser is 5.0 eV. Only two photons are needed for multiphoton ionization of the Cu atoms, compared to 4 and 5 for Ar and He, respectively. The nano-second laser induced plasma above the target is mainly produced by multiphoton ionization and inverse Bremsstrahlung absorption process between thermal electrons and Cu [32]. There should be very few initial high-energy electrons using the nano-second laser versus the pico-second laser. Therefore, gas atmosphere effects are small with the longer nanosecond laser pulse duration, as confirmed by the stress power and ICP-AES data.

From the stress power, ICP-AES, and crater profile data, plasma-shielding appears to be the dominant mechanism for the observed changes between Ar and He atmospheres. Because the laser beam must pass through the gas atmosphere before reaching the sample surface, the properties of the gas can influence the laser-material interaction at the surface. The ionization potential is 24.6 eV and 15.8 eV for He and Ar, respectively. Ar is easier to ionize than He because of its higher ionization cross-section [19], and lower ionization potential. Plasma formation is also a function of pressure. As the gas pressure is increased from 10^{-5} torr to 1 atm a plasma forms more readily because of increased collisions. Thus plasma-shielding is expected to be more significant at higher pressure [33].

In the observations of the craters, as the ambient pressure increased, the rim around the crater became higher and the crater depth shallower. From figures 5.6 and 5.10, as well as reports in the literature [34], the peak shock pressure increases as the ambient pressure increased. This high pressure can push melt out of a crater and form a rim. In addition, scatter of particulates back from the plasma to the surface can occur, as well as vapor condensation [35]. Each of these mechanisms are enhanced by increased ambient pressure. Thus, higher pressures enhance rim growth around the crater. This is consistent with the crater rim results; at higher pressures, the rim height grew. If plasma-shielding does not occur, all the laser energy which is not reflected will be deposited into the solid target, increasing melting and vaporization. The energy absorbed by target would then be the same for different gas pressures. Thus, as the pressure increases more material should be removed from the crater. Yet this is not consistent with the crater depth results. For both He and Ar, the crater depth decreased as pressure increased.

If a plasma is formed in the gas above the target, part of laser energy can be absorbed by the plasma. The energy now contained in the plasma is radiating and convecting away from the target, and less energy is coupled into the solid. Moreover, as the pressure of gas medium increases, a plasma will form more easily and absorb more laser energy. Thus, the energy that reaches the target should decrease as the gas pressure increases, and the amount of material removed from the crater should be smaller. This behavior is consistent with the crater depth results. Similar results in crater depth have recently been reported using

a pump-probe technique to determine plasma shielding during ps-laser ablation [36]. Plasma-shielding appears to be the mechanism most responsible for the observed stress power, ICP-AES, and crater depth results.

For inverse Bremsstrahlung absorption to be the major factor in plasma-shielding in the pico-second time scale, it is postulated that high-energy electrons are generated early in the laser pulse. During the pico-second laser pulse, ejected atoms and ions travel at most a few hundred Angstroms from the surface, assuming velocities of atoms on order of 10^6 cm/s [30,31]. Unlike for the nano-second laser pulse, a substantial collision zone has not formed. Therefore, no appreciable inverse Bremsstrahlung absorption can occur due to collisions of thermal atoms, ions, and slow electrons with gas atoms on the pico-second time scale. The absorption of the laser photons by the emitted atoms/ions to increase the ionized fraction in the plume can be ignored. However, photoelectrons with energies of 100 eV and higher can travel about 100 μm in the same period of time. Many more collisions with the gas atoms can occur, compared to the ejected atoms. Therefore, fast electrons would play a much greater role in forming a plasma in pico-second time scale compared to Cu atoms/ions and slow thermal electrons.

Initial, high-energy electrons may arise when the attenuation of a high electric field occurs over a small distance, and the gradient in the electric field accelerates the electrons to high energies. In experiments with high extraction fields, photoelectrons were measured with energies of 600 eV [18]. With the pico-second laser used in the experiments, the intensity incident on the target is on about 10^{10} W/cm^2. The high

intensity and short pulse width of the pico-second laser make the attenuation of the electric field occur over less than a micron in distance. The attenuation distance would be much longer in the nano-second time regime, so the gradient is much lower. When a high-intensity laser beam interacts with an inhomogeneous plasma, the electrons and ions can be separated by a distance much larger than the Debye length [37], even if there is no extraction electric field. Therefore, high-energy electrons may be present early in the pico-second pulse. Experimental work needs to be conducted to determine the existence of these fast electrons leaving a target in a gas medium. In order to fully characterize plasma-shielding in the pico-second time scale, the velocity distribution and number density must also be measured.

The simple fast-electron generation model shows that it is possible that a plasma can be established above the target early in a pico-second laser pulse. The fast electrons absorb the laser photons during these collisions through an inverse Bremsstrahlung process, developing an ionized plasma of the gas species over the target surface. The extent of plasma development through a change in ionization fraction depends on the properties of the gas. As the gas pressure increases, the ionization of the gas increases. Once developed, the plasma shields the latter part of the laser pulse, thereby reducing the amount of laser energy coupled to the sample and thus lowering the mass removal rate.[14] At low ambient pressure, both Ar and He are not ionized significantly by the inverse Bremsstrahlung mechanism as seen in figure 5.12. Ionization occurs and increases drastically at about 20 torr and 150 torr for Ar and He, respectively. Although the data and model do not agree exactly with

pressure, the behavior between the stress power and crater depth data, and the ionization of the gas medium are similar.

It must be pointed out that the model can not predict the wavelength dependence of the mass remove rate. When there is plasma-shielding, the material removal rate depends on the energy pas ing through the plasma. To determine the amount of energy absorbed, how the absorption coefficient changes with respect to frequency must be known. When the plasma density and temperature are constant, the absorption coefficient reduces as laser frequency increases [38]. The laser beam, then, can more easily penetrate through a plasma which is formed above the target for UV versus IR wavelength. However, as the energy absorbed decreases, the plasma temperature will decrease. Also, the electron density will change depending on the laser intensity at the surface. This temperature decrease will in turn act to increase the absorption coefficient. Any change in election density will also change the coefficient. Therefore, to understand the wavelength dependence for material removal, the complete evolution of the plasma and its dynamics must be considered.

5.5 Conclusion

The stress and shock power, ICP-AES, and crater-volume data demonstrate that there is a different effect of gas medium on the laser material interaction in the pico-second versus the nano-second time domain. In the nano-second regime, the stress and shock power varied little between He and Ar atmospheres during UV irradiation. But during pico-second UV and IR irradiation, the stress power as well as the shock over target power increased markedly in Ar over He. Combined with the

increase mass flux data found by the ICP-AES study, the shock and target power data suggests that plasma shielding is occurring during the pico-second laser ablation of copper in an Ar atmosphere. The depth of ablation craters formed at different gas pressure were measured and the data correlate with the model of gas ionization caused by inverse-Bremsstrahlung absorption between fast photoelectrons and gas atoms. Plasma formation reduces the mass ablation rate and modifies the crater shape. Judicious selection of the gas medium and laser wavelength can improve the performance of material removal for chemical analysis and other applications such as microfabrication. In turn, minimizing the plasma and laser-plasma interaction is likely to reduce the longer time frame thermal component due to plasma radiation. By reducing the slower thermal component, preferential vaporization of highly volatile elements in compound samples should also be minimized, thereby providing improved accuracy in chemical analysis and stoichiometric conditions for fabricating thin-films using laser ablation deposition. Further work must be conducted to determine the temperatures in the plasma with respect to gas medium, and the extent that high-energy electrons are present early in the pico-second pulse.

References

[1] S.A. Darke, S.E. Long, C.J. Pickford, and J.F. Tyson, J. Analyt. Atom. Spectrom. **4**, 715 (1989).

[2] E.R. Denoyer, K.J. Fredeen, and J.W. Hager, Anal. Chem. **63**, 445A (1991).

[3] M. Thompson, J.E. Goulter, and F. Sieper, Analyst **106**, 32 (1981)

[4] K. Dittrich and R. Wennrich, Prog. Analyt. Atom. Spectrosc. 7, 1939 (1984).

[5] A. Inam, M.S. Hedge, X.D. Wu, T. Venkatesan, P. England, P.F. Miceli, E.W. Chase, C.C. Chang, J.M. Tarascon, and J.B. Wachtman, Appl. Phys. Lett. **53**, 908 (1988).

[6] S. Witanachchi, S. Patel, D.T. Show, H.S. Kwok, Appl. Phys. Lett. **55**, 295 (1989).

[7] X.L. Mao, R.E. Russo, H.B. Liu, J.C. Ho, Appl. Phys. Lett. **57**, 2591 (1990).

[8] K. Sugioka and K. Toyoda, Jap. J. Appl. Phys. I **29**, 2255 (1990).

[9] K.D. Sternitzke and R.L. McCreery, Anal. Chem. **62**, 1339 (1990).

[10] R.R. Anderson and J.A. Parrish, Science **220**, 524 (1983).

[11] Yasuo Iida, Spectrochim. Acta **45B**, 1353 (1990).

[12] W.T. Chan, X.L. Mao, and R.E. Russo, Appl. Spectrosc. **46**, 1025 (1992).

[13] Z. Toth and T. Szorenyi, Appl. Phys. A **52**, 273 (1991).

[14] J.F. Ready, in *Effects of High-Power Laser Radiation*, (Academic Press, Inc., New York, 1971), p. 187.

[15] J.N. Bradley, in *Shock Waves in Chemistry and Physics* (John Wiley and Sons, New York 1962).

[16] W.T. Chan and R.E. Russo, Spectrochim. Acta **46B**, 1471 (1991).

[17] W.T. Chan and R.E. Russo, "Characteristics of Laser-Material Interactions Monitored by Inductively Coupled Plasma-Atomic Emission Spectroscopy" in *Laser Ablation Mechanisms and Applications Proceeding,* Oak Ridge, Tennessee, USA, 91, J.C. Miller and R.F. Haglund, Jr., Eds., (Springer-Verlag 1991), pp 53-59.

[18] R.J. Harrach, "Theory for Laser-Induced Breakdown Over a Vaporizing Target Surface", Report No. UCRL-52389, Lawrence Livermore Laboratory, University of California, 1987.

[19] L.J. Kieffer, "A compilation of electron collision cross section data for modeling gas discharge lasers", Boulder, Colo. : Univ. of Colorado, 1973 Report - Joint Institute for Laboratory Astrophysics, Information Center ; no. 13.

[20] S.D. Moustaizis, M. Tatarakis, C. Kalpouzos, and C. Fotakis, Appl. Phys. Lett. **60**, 1939 (1992).

[21] G. Farkas and C. Toth, Phys. Rev. A **41**, 4123 (1990).

[22] M. Thompson, S. Chenery, L. Brett, J. Analyt. Atom. Spectrom. **5**, 49 (1990).

[23] P. Arrowsmith and S.K. Hughes, Appl. Spectrosc. **42**, 1231 (1988).

[24] R. Kelly, J.J. Cuomo, P.A. Leary, J.E. Rothenberg, B.E. Braren, and C.F. Aliotta, Nucl. Instr. and Meth. in Phys. Res. **B9**, 329 (1985).

[25] J.E. Rothenberg and R. Kelly, Nucl. Instr. and Meth. in Phys. Res. **B1**, 291 (1984).

[26] R. Kelly and J.E. Rothenberg, Nucl. Instr. and Meth. in Phys. Res. **B7/8**, 755 (1985).

[27] D.I. Rosen and G. Weyl, J. Phys. D: Appl. Phys. **20**, 1264 (1987)

[28] G. Morgan, Rep. Prog. Phys. **38**, 624 (1975).

[29] R.J. Dewhurst, J. Phys. D: Appl. Phys. **10**, 283 (1977).

[30] W. Marine, J.M. Scotto d'Aniello and M. Gerri, Materials Science and Engineering **B13**, 57 (1992).

[31] O.L. Landen and W.E. Alley, Phys. Rev. A **46**, 5089 (1992).

[32] R.W. Dreyfus, J. Appl. Phys. **69**, 1721 (1991)

[33] T. Auguste, P. Monot, L.A. Lompre, G. Mainfray, and C. Manus, Optics Commun., **89**, 145 (1992).

[34] R.E. Beverly III and C.T. Walters, J. Appl. Phys. **47**, 3485 (1976).

[35] R. Kelly, J. Chem. Phys. **92**, 5047 (1990).

[36] S. Preuss, M. Späth, Y. Ahang, and M. Stuke, Appl. Phys. Lett. **62** (23), 3049 (1993).

[37] H. Hora, in *Plasmas at High Temperature and Density*, (Springer-Verlag, New York, 1991), p. 170.

[38] M. von Allmen, in *Laser-Beam Interactions with Materials - Physical Principles and Applications* (Springer-Verlag, New York 1987), pp 156.

Appendix I

Fortran Program for Calculating Temperatures, Gradients, and Probe Beam Deflections In Air Over a Surface Undergoing Melt

The following are Fortran programs to calculate the temperatures, gradients, and deflections of a light rays in a medium heated by a surface at one boundary. The domain is axi-symmetric and is considered semi-infinite above the surface in the z direction and in the radial direction. The outer boundary temperatures are set to the initial conditions, with the z boundary set to 3 thermal diffusion lengths and the r direction set to 3 thermal diffusion lengths or 1 thermal diffusion length from the outer most edge from the maximum melt front propagation distance. The calculations are in non-dimensional form as given in sections 3.3.4 and 3.3.5.

Program Listing

```
c  AXI-SYMMETRIC HEAT TRANSFER PROGRAM

c  Written by
c  Mark A. Shannon
c  U.C. Berkeley, Mechanical Engineering Dept. and
c  Lawrence Berkeley Laboratory.

c  An EXPLICIT FINITE-DIFFERENCE scheme is used
c  to calculate the heat transfer due to laser heating
```

```
c  of a solid target in air for short time durations.  Therefore,
c  the energy transfer is assumed to be by diffusion and radiant
c  transfer only, with convection into the air assumed negligibly
c  small due to the short times involved.  If this program is to
c  be used for long enough time periods that convection becomes
c  important, then the boundary conditions will need to be modified.

c  The main program requires an input file be supplied with name "in".
c  the file reads in various different parameters of the problem to
c  be solved.  "in" uses a general number input format, but reads
c  the numbers starting 10 spaces in with a field of 12 characters.
c  Example of input file in order that parameters are read.

c  w(radius)=8.0e-5
c  Power =  40.0
c  tpulse =  2.0e-3
c  Tint =  300.0
c  Tamb =  300.0
c  Tmelt =  429.76
c  Tboil =  2440.0
c  L =  28254.
c  aspect =  1.0 (min of 1.)
c  divideR = 1.0 (min of 1.)
c  surf =  1.0 (min of 1.)
c  step =  1.0 (min of 1.)
c  zray =  1.0
c  cycle =  1 (min of 1)
c  outstep = 1 (min of 1)
c  numrays = 1 (min of 1,max of num-1)

c  The explanations of parameters are given below before the read
c  statement.

c  Declare the size of the arrays by the maximum expected number of
c  nodes with num, and number of pts to calculate gradient with.
```

```
      Integer  num
      Parameter (num=200)

c     Declare the external functions called by the main program and
c     some of its subroutines.
      Double precision   spheat,cond,rho
      External  spheat,cond,rho

c     Declare the global and internal variables used by the main
c     program and its subroutines.
      Double precision  newT(num,num),T(num,num),z(num),r(num),
     &                  Ksp,Knp,Kwp,Kep,km(2),theta(num),ztheta(num),
     &                 S(2),divideR,diff(2),del,Sm,To,Tstar,aspect,
     &                  dt,mn,dz,dz0,w,dr,rp,tpc,tc,tbar,delta,
     &                  Tint,Tamb,Tmelt,Tboil,Te,Tw,Ts,Tn,Tp,Ti,Tb,
     &                 Ae,Aw,As,An,Ap,App,L,Ste,diffRatio,pi,
     &                 Tm,Tba,Ta,Power,surf,step,tpcSteRatio,
     &                 Itime,time,tpulse,Rsing,zray,gradZ,SteRatio

      Integer   fn,i,j,k,ki,ip,m,n,p,cycle,outstep,numrays

      Open(23,file = 'case')
      Open(24,file = 'in')
c     Open(25,file = 'tsurf')
c     Open(26,file = 'temp')
c     Open(27,file = 'grad',recl=4212)
c     Open(27,file = 'grad',recl=1000)
c     Open(28,file = 'gradT')
c     Open(29,file = 'theta',recl=1000)
c     Open(30,file = 'S',recl=1000)
      Open(25,file = 'theta1',recl=2000)
      Open(26,file = 'theta2',recl=2000)
      Open(27,file = 'theta3',recl=2000)
      Open(28,file = 'theta4',recl=2000)
      Open(29,file = 'theta5',recl=2000)
```

```
      Open(30,file = 'theta6',recl=2000)
      Open(31,file = 'theta7',recl=2000)

c   Call C preprocessor for defining variables to arrays.
#include "main.h"

c   Set time step for data output to get 100 data points.
      delta = 0.01

c   Read in data for beam radius (w), Power, pulse length (tpulse),
c   initial and ambient temperatures (Tint & Tamb), melting & boiling
c   temperatures (Tmelt & Tboil),  overall grid size divisor (divide),
c   surface grid divisor (surf), time step divisor (step),
c   tolerance (tol),
c   the number of cycles of on & off time
c   (cycle), number of steps between output (outstep).
c   Units: w{m}; Power{W}; tpulse{s}; Tint, Tamb, Tmelt, &
c   Tboil{deg. K};
c   divide, surf, step, cycle, outstep, & tol {unitless}.
      Read(24,12)  w,Power,tpulse,Tint,Tamb,Tmelt,Tboil,L,
     &             aspect,divideR,surf,step,zray,
     &             cycle,outstep,numrays

 12    Format (13(10x,g12.5/),3(10x,I3/))
 13    Format(4(10x,g12.5/))
 14    Format(7(F12.5,2x))
 15    Format(5(I4,2x))
 16    Format(I4,2x,F12.5,2x,F12.5,2x,F12.5)
      Close(24)

c      Write(6,*) 'w, Power, tpulse, Tint, Tamb, Tmelt, & Tboil ='
c      Write(6,14)  w,Power,tpulse,Tint,Tamb,Tmelt,Tboil
       Write(6,*)'aspect, divideR, surf, step, & zray ='
       Write(6,14) aspect,divideR,surf,step,zray
       Write(6,*) 'cycle, outstep & numrays ='
```

```
      Write(6,15) cycle,outstep,numrays

c  Set pi.
      pi = 3.141592654

c  Calculate non-dimensional temperatures
      Tba = Tboil - Tamb
      Tb = (Tboil - Tamb)/Tba
      Tm = (Tmelt - Tamb)/Tba
      Ti = (Tint - Tamb)/Tba
      Ta = 0.
      To = (273.15 - Tamb)/Tba
      Tstar = Tamb/Tba
c      Write(6,*) 'Tba, Tb, Tm, Ti, Ta ='
c      Write(6,14) Tba,Tb,Tm,Ti,Ta

c  Calculate property data for starting and spatial and temporal
c  step sizes.
      Call Grid(num,Tmelt,Tint,Tboil,km,diff,Sm,Ste,L,pi,tc,
     &          dt,dz0,dr,surf,divideR,aspect,m,n,Power,tpulse)

c  Calculate the diffusivity ratio for the materials being considered.
      diffRatio = alphaLIQ/alphaAIR

c  Give the calculated Stephan number and diffusivity ratio.
      Write(6,*) 'The calculated Stephan number is ', Ste
      Write(6,*) 'The calculated diffusivity ratio is ', diffRatio

c      Write(6,*) 'Enter the Stephan number desired for calculating the
c     & temperature field.'
c      Write(6,*) 'Enter the ratio desired between the boundary
c     & material '
c      Write(6,*) 'and deflecting medium above melting temperature.'
      Read(23,13) Ste,diffRatio,SteRatio,Rsing
      Write(6,*) 'The values for Ste, diffRatio, SteRatio, Rsing ='
```

```
      Write(6,*)  Ste,diffRatio,SteRatio,Rsing

c  Calculate the thermal diffusion length in the medium, and give the
c  melt front distance at time = tpulse.
      del = SQRT( alphaAIR * tpulse )
       Write(6,*) 'The value of del & Sm for this material is', del, Sm

c   Start looping for different cases of SteRatio.
       Do 700  p = 1, 1
       fn = 24 + p
        Open(24,file = 'in')
        Read(24,12)  w,Power,tpulse,Tint,Tamb,Tmelt,Tboil,L,
     &              aspect,divideR,surf,step,zray,
     &              cycle,outstep,numrays
        Close(24)
        Write(6,*)
        Write(6,*) 'Starting run p with SteRatio =' , p,SteRatio

c   Assign characteristic time, tc.
        If (del .LE. Sm)  then
        tc = tpulse/(3. * SteRatio)
         Write(6,*) 'tc independent of material & tc =',tc
        Else
        tc = Sm**2 * tpulse/(3. * SteRatio * del**2)
         Write(6,*) 'tc depends on material & tc =',p,tc
        Endif

c   Assign the constants used in the calculations.
       tpc = tpulse/tc
      tpcSteRatio = tpc/SteRatio

c   Set the maximum diameter of the singularity, Rsing = Sboil(max).
c   Adjust Rsing in the input file case to calculate the deflection
c   further away (Rsing > 1) or closer to (Rsing < 1) to r = 0.
       Rsing = tpc**(1./3.)/(1. + tpc**(1./3.))
```

```
      If (Rsing .GT. tpc**(1./3.)/2.)  Rsing = tpc**(1./3.)/2.
      Write(6,*) 'Rsing, Sbmax, & Sm/Sb max ='
      Write(6,*) Rsing,tpc**(1./3.)/(1.+tpc**(1./3.)),1.+tpc**(1./3.)

c  Assign the grid spacings based on the difference between the
c  maximum phase front location and the presumed singular point.
 40    dr = (tpc**(1./3.) - Rsing)/divideR
       dz0 = dr * aspect
       Write(6,*) 'dr & dz =', dr, dz0

c  Assign the time step, dt.
       dt = 1.5 * (dz0/surf * dr)**2
     &       /( ((dz0/surf)**2 + dr**2) * tpcSteRatio * step)

c  Make sure that the time step at output is the same for all
c  runs.  dt may be adjusted slightly to ensure this.
       outstep = Int( delta/dt )
       Write(6,*) 'Calculated and final time step =', dt,
     &              delta/Dble( outstep )
       dt = delta/Dble( outstep )

c  Set number of time steps in one time pulse.
       mn =  1./dt
       Write(6,*) 'tpc and mn = ', tpc,mn
       If (2.*mn .GT. 2.d09)  then
        Write(6,*) 'dt is too small for full cycle to run.'
       Endif

c  Set the domain size so it behaves as if it is thermally infinite.
       Write(6,*) 'Sm(tc) & del/Sm(tc) are', Sm/tpc**(1./3.),
     &                                  del/(Sm/tpc**(1./3.))
       m = INT( 2.5 * tpc**(1./3.) * del/(Sm * dz0) )
       If (m .GE. num)  then
       aspect = aspect + 1.0
       If (aspect .GT. 10.0)  then
```

```
        Write(6,*) 'Ending run, aspect >10 at p = ', p
       Go to 800
      Endif
      Go to 40
     Endif
     n = INT( tpc**(1./3.) * (1. + 1.5 * del/Sm)/dr )
     If (n .GE. num)  then
      divideR = divideR - 1.0
      If (divideR .LE. 1.0)  then
       Write(6,*) 'Ending run, divideR < 1 at p =', p
       Go to 800
      Endif
      Go to 40
     Endif

     Write(6,*) 'Final divideR & aspect are ', divideR, aspect
     Write(6,*) 'Final m & n  are ',m,n

c    Set the maximum diameter of the singularity, Rsing = Sboil(max).
c    Adjust Rsing in the input file case to calculate the deflection
c    further away (Rsing > 1) or closer to (Rsing < 1) to r = 0.
       Rsing = tpc**(1./3.)/(1. + tpc**(1./3.))
       If (Rsing .GT. tpc**(1./3.)/2.)  Rsing = tpc**(1./3.)/2.
       Write(6,*) 'Rsing, Sbmax, & Sm/Sb max ='
       Write(6,*) Rsing,tpc**(1./3.)/(1.+tpc**(1./3.)),1.+tpc**(1./3.)

c    Initialize temps, quality, heat, & phase-front position.
c    Also assign location of nodal points in region 2.
c    Initialize temps, quality, heat, & phase-front position.
c    Also assign location of nodal points in region 2.
       Smelt = 0.
       Sboil = 0.

c    Initialize temps for each grid point.
       Do 50  i = 1,m+1
```

```
      Do 50  j = 1,n+1
       newT(i,j) = Ti
 50    T(i,j) = Ti

c  For constant properties, the non-dimensionalized conductivities
c  all equal 1 and do not have to be calculated in the loop.  If
c  temperature dependent properties are desired, un-comment the
c  call to Conduct.
       Kep = 1.
       Kwp = 1.
       Ksp = 1.
       Knp = 1.

c  Set the z and r dimensions of the grid.
      Do 60  i = 1,m+1
       If (i .EQ. 1)  then
        z(i) = 0.
       Elseif (i .EQ. 2)  then
       z(i) = dz0/surf
      Else
        z(i) = ( DBLE( i-3 ) + .5*(1. + 3./surf) ) * dz0
       Endif
 60    Continue
      Do 70  j = 1,n+1
 70     r(j) = Dble( j - 1 ) * dr

c  Initialize time and beam deflections.
      time = 0.
      tbar = 0.
      Do 80  i = 1, numrays+1
       theta(i) = 0.0
 80     ztheta(i) = z(i)/zray
      ztheta(numrays+2) = z(2)

c  Start overall loop for number of cycles to be calculated, and
```

```
c  initialize time counter.
     Do 600  ip = 1, cycle
      k =  Int( mn )
      ki = 1

c  Loop for time steps up to time = 2*tpulse for 1 cycle.
 100    If (k .GT. 0)  then

c  Write data desired to output files.  Output also calculates desired
c  derivates of temps or phase-front positions.
        If (ki .EQ. 1)  Call Output(num,n,m,theta,T,S,dz0,dr,surf,time,
     &                          numrays,ztheta,r,fn)

c  Calculate time dependence of input power. This is where
c  recalulations begin when time step is adjusted smaller.
        Call PulseShape(ip,Itime,Power,time)

c  Calculate the boiling position S(boil) and S(melt) as a function
c  of the time.
        Smelt = (tbar * tpc)**(1./3.)
        Sboil = Smelt/(1. + Smelt)

c  Assign values for the temperature of the boundary.
        Do 300  j = 1, n
         If ( (Itime .GT. 0.) .AND. (tbar .GT. 0.) )  then
          If (r(j) .LE. Sboil)  then
           T(1,j) = Tb
          Elseif ( (r(j) .GT. Sboil) .AND. (r(j) .LE. Smelt) )  then
           T(1,j) = 1./r(j) - 1./((tpc * tbar)**(1./3.))
          Else
           T(1,j) = Tm
          Endif
         Else
          T(1,j) = Tm
         Endif
```

```
300   Continue

c  Start the temperatures calculations. Note: temps for i = 1 are not
c  found since the temperature boundary is given as a result of an
c  approximate temperature solution of a melting surface.
      theta(numrays+2) = 0.
      ztheta(numrays+2) = z(2)
       Do 400  i = 2, m
       Do 400  j = 1, n

c  Assign temperatures to node and its neighbors.
        Tp = T(i,j)
        Te = T(i,j+1)
        Tn = T(i+1,j)
        Ts = T(i-1,j)

c  Set nodal temps for cases where r = 0 for Tw.
        If (j .EQ. 1)  then
         Tw = Te
        Else
         Tw = T(i,j-1)
        Endif

c  Assign dimensions needed.
        rp = r(j)
       dz = dz0

c  Calculate conductivites at nodal points in the gas of region 1.
c  For constant properties K all equal 1 so call is commented out.
c       Call Conduct(i,j,num,T,Kep,Kwp,Ksp,Knp)

c  Assign coefficients used in eqn.
        Call Coeff(i,j,Ae,Aw,As,An,Ap,App,dz,dr,rp,
     &             Kep,Kwp,Ksp,Knp,Tp,dt,tpcSteRatio)
```

```
c  Calculate new temperature directly from temperature eqn.
       newT(i,j) = ((Ap+App)*Tp + As*Ts + An*Tn + Aw*Tw +
     &                 Ae*Te)/App

c  Apply constant temperature boundary conditions at edges of region.
       If (j .EQ. n)  newT(i,n) = Ta
       If (i .EQ. m)  newT(m,j) = Ta

 400   Continue

c  Find the deflection from the last calculated temperature field.
c  Do this only when output of data is needed.
       If (ki .EQ. 2)  then
        Call Deflection (num,m,n,theta,dr,z,r,Rsing,T,numrays,
     &                   zray,ztheta,To,Tstar)
       Endif

c   Reset the counter for the next data output.
       If (ki .EQ. 1)  ki = outstep + 1

c  Update the counter.
       ki = ki - 1

c  Update the new temperatures.
       Do 500  i = 2, m
       Do 500  j = 1, n
 500    T(i,j) = newT(i,j)

c  Update time & time step, and return to beginning of time loop.
       tbar = tbar + dt
       time = tbar
       k = k - 1
       Go to 100
      Endif
```

```
600  Continue

c    Set the stephan number and diffusivity ratio for the next run.
     SteRatio = 2. * SteRatio
     If (p .GE. 5)  SteRatio =  Dble( 2 * p )

700  Continue

800  Close(23)
     Close(25)
     Close(26)
     Close(27)
     Close(28)
     Close(29)
     Close(30)
     Close(31)

     Stop
     End
```

```
c This subprogram contains the following subroutines which are
c called by melt.main.f:
c Grid, PulseShape, Conduct, Coeff, Output, Deflections & Element.

c  Pass subroutines through C preprocessor.
#include "main.h"

c ***************************************************************

      Subroutine  Grid(num,Tmelt,Tint,Tboil,km,diff,Sm,Ste,L,pi,tc,
     &                 dt,dz0,dr,surf,divideR,aspect,m,n,Power,tpulse)

c This subroutine calculates property data needed for non-
c dimensionalizing the equations and for determining the
c spatial and temporal step sizes.

      Double precision  km(2),rhom(2),Cp(2),diff(2),divideR,Ste,L,
     &                  Tmelt,Tint,Tboil,dt,dz0,dr,surf,pi,tpulse,
     &                  rho,cond,spheat,Power,tc,Sm,aspect
      Integer  R,m,n,num

c Calculate the conductivity, density, specific heat, and diffusivity
c above phase change in regions 1 & 2 (medium and boundary).
      Do 100  R = 1, 2
       rhom(R) = rho( R, Tmelt + 1. )
       Cp(R) = spheat( R, Tmelt + 1. )
       km(R) = cond( R, Tmelt + 1. )
100    diff(R) = km(R)/(rhom(R) * Cp(R))

c Calculate the Stephan number for the material being considered.
      Ste = (spheat( 2, Tmelt + 1. ) * (Tboil - Tmelt))/L

c Determine grid sizes dz and dr,
c and max time step, dt, for z direction for the region.
      tc = Power**2 *rhom(2)*L/(12.*pi**2 *(kLIQ*(Tboil-Tmelt))**3)
```

```
      Sm = (1.5 * Power * tpulse/(pi * rhom(2) * L))**(1./3.)
      dr =  1./divideR
      dz0 = dr * aspect
      n =  Int( 4. * divideR )
      m = n/Int( aspect )

      If (m .GE. num)  then
       m = num-1
      Endif
      If (n .GE. num)  then
       n = num-1
      Endif

      dt = 1.5*(dz0/surf * dr)**2 * alphaLIQ * Ste
     &    /( ((dz0/surf)**2 + dr**2) * alphaAIR * tpulse/tc)

      Write(6,*) 'The calculated values for dt, tc, & Sm(tc) ='
      Write(6,*) dt,tc,Sm
      Write(6,*) 'dz0, dr, m, & n =', dz0,dr,m,n

      Return
      End

c ***********************************************************
c ***********************************************************

      Subroutine PulseShape(ip,Itime,Power,time)

c  This subroutine specifies h(t), shape of pulse--rectangular.
c  Must be modified if other time dependence of the power is desired.

      Double precision  Itime,Power,time
      Integer  ip

      If ( (time .GE. Dble( 2*(ip - 1) )) .AND.
```

```
     &       (time .LT. Dble( 2*ip - 1 )) ) then
             Itime = Power
             Else if ( (time .GE. Dble( ip - 1 )) .AND.
     &            (time .LT. Dble( ip )) ) then
             Itime = 0.
             Endif

             Return
             End

c ************************************************************
c ************************************************************

             Subroutine Conduct(i,j,num,T,Kep,Kwp,Ksp,Knp)

c  This subroutine calculates the conductivities between neighboring
c  nodal points and the central node of the grid elements being
c  considered (eg. Kep, which is the geometric average between points).
c  It uses functions cond()  to calculate the temperature dependent
c  conductivities of a node.  The values of Kep, etc. are non-
c  dimensionalized by dividing each term by kp.  The resulting terms
c  reflect the variation in conductivity in each direction with
c  changes in temperature.

             Integer  i,j,num
             Double precision  T(num,num),Kep,Kwp,Ksp,Knp,
     &                  ke,kw,ks,kn,kp,cond

c  Assign the conductivities of the nodal points.

             ke = cond( 1, T(i,j+1) )
             kn = cond( 1, T(i+1,j) )
             kp = cond( 1, T(i,j) )
             ks = cond( 1, T(i-1,j) )
             If (j .GT. 1)        kw = cond( 1, T(i,j-1) )
```

```
      If (j .EQ. 1)  kw = ke

c  Assign geometric conductivity averages between nodes.
      Knp = 2. * kn/(kn + kp)
      Kwp = 2. * kw/(kw + kp)
      Kep = 2. * ke/(ke + kp)
      Ksp = 2. * ks/(ks + kp)

      Return
      End

c ***********************************************************
c ***********************************************************

      Subroutine Coeff(i,j,Ae,Aw,As,An,Ap,App,dz,dr,rp,
     &                 Kep,Kwp,Ksp,Knp,Tp,dt,tpcSteRatio)

c  This subroutine calculates the coefficients used for the
c  main equation.  The values returned depend on whether it is an
c  internal or central axis node.
c  This subroutine calls function rho to
c  calculate temperature dependent densities.

      Double precision  Kep,Kwp,Ksp,Knp,dz,dr,rp,tpcSteRatio,
     &                  Ae,Aw,As,An,Ap,App,Tp,dt
      Integer  i,j

c  Assign values for where r equals 0 or not.
      If (j .EQ. 1)  then
       Ae = 4. * Kep * dz/dr**2
       Aw = Ae
      Else
       Ae = Kep * dz * (1. + .5 * dr/rp)/dr**2
       Aw = Kwp * dz * (1. - .5 * dr/rp)/dr**2
      Endif
```

```
      As = Ksp/dz
      An = Knp/dz
      Ap = -(Ae + Aw + As + An)
      App = 3./tpcSteRatio * dz/dt

      Return
      End

c ********************************************************
c ********************************************************

      Subroutine Output(num,n,m,theta,T,S,dz0,dr,surf,time,
     &                  numrays,ztheta,r,fn)

c  This subroutine calculates derivatives desired and writes them to file.
c  Uncomment out calculations desired, making sure that appropriate
c  files have been opened in the main program.

      Integer  num,n,m,i,j,numrays,fn
      Double precision  T(num,num),S(2),dTdz(10),theta(num),r(num),
     &                  dz0,dr,surf,time,ztheta(num)

c     dTdz(1) = (T(1,1) - T(2,1))/( .5*(dz0/surf + dz0) )
c     dTdz(2) = .5/dz0 * ( (T(1,1) - T(2,1))/(.5/surf + .5)
c    &                   + (T(2,1) - T(3,1)) )
c     dTdz(3) = .5*(T(2,1) - T(4,1))/dz0
c     dTdz(4) = .5*(T(4,1) - T(6,1))/dz0
c     dTdz(5) = .5*(T(6,1) - T(8,1))/dz0

c     dTdz(6) = -.5/dz0 * ( (T(1,1) - T(2,1))/(.5/surf + .5)
c    &                   + (T(2,1) - T(3,1)) )
c     dTdz(7) = -.5/dz0 * ( (T(1,4) - T(2,4))/(.5/surf + .5)
c    &                   + (T(2,4) - T(3,4)) )
c     dTdz(8) = -.5/dz0 * ( (T(1,7) - T(2,7))/(.5/surf + .5)
```

```
c   &                + (T(2,7) - T(3,7)) )
c      dTdz(9) = -.5/dz0 * ( (T(1,10) - T(2,10))/(.5/surf + .5)
c   &                + (T(2,10) - T(3,10)) )
c      dTdz(10) = -.5/dz0 * ( (T(1,13) - T(2,13))/(.5/surf + .5)
c   &                + (T(2,13) - T(3,13)) )

c  Write the gradients to a file.
c      Do 100  j = 1, n/2, 2
c       Write(27,12) time,r(j),(0.5*(T(i+1,j)-T(i-1,j))/dz0,i=2,m/2,2)
c100    Continue

c  Write the gradients to a file.
c      Do 100  j = 2, n/2+2
c       Write(27,12) time,r(j),(0.5*(T(i,j+1)-T(i,j-1))/dr,i=1,3)
c100    Continue

c      Write(23,11) time,T(1,1),T(1,3),T(1,5),T(1,7),T(3,n-3)
c      Write(26,11) time,T(2,1),T(2,5),T(2,10),T(2,15),T(m-3,3)
c      Write(27,11) time,dTdz(1),dTdz(2),dTdz(3),dTdz(4),dTdz(5)
c      Write(28,11) time,dTdz(6),dTdz(7),dTdz(8),dTdz(9),dTdz(10)
c      Write(29,11) time,theta(2),theta(3),theta(4),theta(5),theta(6)
       Write(fn,11) time,(theta(i),i = 1,numrays)
c       Write(30,11) time,Smelt,Sboil,Smelt/Sboil
c       Write(30,11) time,(ztheta(i),i = 1,numrays)

 11    Format(100(1pe12.5,1x))
 12    Format(1pe12.5,350(',',1pe10.3))
      Return
       End

c ***********************************************************
c ***********************************************************

      Subroutine Deflection(num,m,n,theta,dr,z,r,Rsing,T,numrays,
     &                zray,ztheta,To,Tstar)
```

```
c  This subroutine finds the deflection of a single ray of light
c  near the boundary surface of the domain. It calls the routine
c  Element which finds the coefficients for calculating the
c  temperature gradient near the surface.

      Integer  i,j,k,kk,m,n,num,numrays
      Double precision  T(num,num),z(num),theta(num),ztheta(num),
     &          r(num),a(3),dtheta,Rsing,gradZ1,gradZ2,
     &          zray,dr,thetasum,dndT,To,Tstar

c  Start the integration loop for calculating the deflection.
c  First set theta to zero to start deflection calculations.
      Do 700  k = 1, numrays
       ztheta(k) = z(k+1)/zray
       theta(k) = 0.
       thetasum = 0.

c  Intergrate the beam on the path in towards the center.
      Do 300  j = n, 2, -1

c  Calculate the non-dimensional deflection of a ray passing
c  traverse to the melt boundary. First assign the first point
c  needed for interpolation.
       Do 100  i = 1, m-1
        If (ztheta(k) .LE. (z(i+1)+z(i+2))/2.)  then
         Go to 200
        Endif
100    Continue

200    If (r(j) .GE. Rsing + dr) then

c  Set the deflection coefficient 1/n dn/dT used for calculating
c  the angle the beam bends. Here it is assumed that n = 1 and dn/dT
c  is from the ideal gas approximation and the ratio from 0deg C of
```

```
c  (n-1)o/(n-1) = (rho)o/(rho) where for air (n-1)o = 2910(e-07).
c        dndT = 2.91d-04 * (To + Tstar)/(T(i+1,j) + Tstar)**2

c  This approximation for dn/dT neglects the changes in n with T.
        dndT = 1.50d-04/((T(i+1,j+1)+T(i+1,j)+T(i+1,j-1))/3. + Tstar)

c  Find the temperature gradient normal to the boundary.
        If (j .EQ. n)  then
         gradZ2 = 0.
        Endif
        gradZ1 = gradZ2
        Call  Profile(num,i,j-1,a,z,T)
        gradZ2 = a(2) + 2.*a(3)*(ztheta(k) - dndT*gradZ1*dr**2)

c  Update the position of theta, ztheta and counter.
        dtheta = -dndT * (gradZ1 + gradZ2) * dr/2.
        thetasum = thetasum + dtheta
        ztheta(k) = ztheta(k) + thetasum * dr
       Endif
 300   Continue

c  Next integrate over the path from the center out.
      kk = 1
       Do 600  j = 2, n-1
      Do 400  i = 1, m-1
       If (ztheta(k) .LE. (z(i+1)+z(i+2))/2.)  then
        Goto 500
       Endif
 400    Continue

c  Find the temperature gradient normal to the boundary.
 500    If (r(j) .GE. Rsing) then
       dndT = 1.50d-04/((T(i+1,j-1)+T(i+1,j)+T(i+1,j+1))/3. + Tstar)
       If (kk .EQ. 1)  then
        Call  Profile(num,i,j,a,z,T)
```

```
        gradZ2 = a(2) + 2.*a(3)*ztheta(k)
       Endif
       gradZ1 = gradZ2
       Call  Profile(num,i,j+1,a,z,T)
       gradZ2 = a(2) + 2.*a(3)*(ztheta(k) - dndT*gradZ1*dr**2)

c  Update the position of theta, ztheta and counter.
         dtheta = -dndT*(gradZ1 + gradZ2) * dr/2.
       thetasum = thetasum + dtheta
       ztheta(k) = ztheta(k) + thetasum * dr
       kk = kk + 1
      Endif
600    Continue
      theta(k) = thetasum
700   Continue

      Return
      End

c ***********************************************************
c ***********************************************************

      Subroutine  Profile(num,i,j,a,z,T)

      Integer  num,i,j
       Double precision   T(num,num),z(num),a(3),det

c  Assign the determinate of the "a" matrix, det.
       det = z(i+1)*z(i+2)**2 - z(i+2)*z(i+1)**2 - z(i) *
     &       (z(i+2)**2 - z(i+1)**2) + z(i)**2 *(z(i+2) - z(i+1))

       a(1) = ( T(i,j) *(z(i+1)*z(i+2)**2 - z(i+2)*z(i+1)**2) -
     &          z(i) *(T(i+1,j)*z(i+2)**2 - T(i+2,j)*z(i+1)**2) +
     &          z(i)**2 *(T(i+1,j)*z(i+2) - T(i+2,j)*z(i+1)) )/det
```

```
      a(2) = ( T(i+1,j)*z(i+2)**2 - T(i+2,j)*z(i+1)**2 -
     &         T(i,j) *(z(i+2)**2 - z(i+1)**2) +
     &         z(i)**2 *(T(i+2,j) - T(i+1,j)) )/det

      a(3) = ( T(i+2,j)*z(i+1) - T(i+1,j)*z(i+2) -
     &         z(i) *(T(i+2,j) - T(i+1,j)) +
     &         T(i,j) *(z(i+2) - z(i+1)) )/det

      Return
      End

c *****************************************************************
```

```
c This subprogram contains the subroutines which are specifically called
c for the materials air, Indium, and Tin, for regions 1 & 2 by the main
c program melt.main.f.

c ***********************************************************

      Double precision Function spheat( R, Tp )

c This function returns the temp dependent specific heat of air, and
c calculates the specific heat of Indium {J/(kg C)},
c depending on temperature and phase.

      Double precision  Tp
      Integer  R

      If (R .EQ. 1)  then

c The specific heat of air is calculated from those of N2 and O2 found
c from data in CRC.
        If (Tp .LE. 650.)  then
          spheat = 1.04270918415 - 3.1186402486404d-04*Tp
     &       + 7.087645687646d-07*Tp**2 - 2.71639471639496d-10*Tp**3
        Else if (Tp .GT. 650.)  then
          spheat = 0.610610221283 + 1.097392587603d-03*Tp
     &          - 7.501701557086d-07*Tp**2 + 1.923219044211d-10*Tp**3
        Endif

      Else

c Calculate the specific heat of Indium {J/(kg C)} from data in
.....Thermophysical Properties of Matter.
        If (Tp .LT. 429.76) then
         spheat = 337.11 - .7778*Tp + 1.41e-3*Tp**2
        Else
         spheat = 4.186*61.
```

```
      Endif
     Endif

     Return
     End

c ************************************************************
c ************************************************************

     Double precision Function cond( R, Tp )

c  This function calculates the conductivity of Air{W/(m C)}, and
c  of Indium {W/(m C)}, depending on temp and phase.

     Double Precision  Tp
     Integer  R

     If (R .EQ. 1)  then

c  Calculate for Air.
      cond = 0.02624 * (Tp/300.)**.85

     Else

c  Calculate for Indium.
      If (Tp .LT. 429.76) then
       cond = 103.52 - .0725*Tp
      Else if (Tp .LT. 2440.) then
       cond = 35.967 - 1.207e-2*Tp + 2.82e-5*Tp**2
     Else
      cond = 174.41
      Endif
     Endif

      Return
```

```
      End

c ***********************************************************
c ***********************************************************

      Double precision Function rho( R, Tp )

c  This subroutine calculates the temperature dependent density of the
c  material in regions 1 & 2.  This subroutine must be altered when
c  different materials are used.  Here region 1 is air and region 2
c  is Indium.

       Double precision  Tp
      Integer  R

       If (R .EQ. 1) then

c  Assign density of air {kg/m^3}.
        rho = 101.3/(.287*Tp)

c  Assign density of Indium {kg/m^3}.  Density is now also dependent
c  on phase.
      Else
        If (Tp .LT. 429.76) then
         rho = 7560. - .8*Tp
        Else if (Tp .LT. 2440.) then
         rho = 7830. - 1.7*Tp
       Else
        rho = 3750.
        Endif
      Endif

       Return
       End
```

```
c ***********************************************************
c ***********************************************************

      Double precision Function spheat( R, Tp )

c  This function returns the temp dependent specific heat of air, and
c  calculates the specific heat of Tin {J/(kg C)},
c  depending on temperature and phase.

      Double precision  Tp
      Integer  R

      If (R .EQ. 1)  then

c  The specific heat of air is calculated from those of N2 and O2 found
c  from data in CRC.
        If (Tp .LE. 650.)  then
          spheat = 1.04270918415 - 3.1186402486404d-04*Tp
     &       + 7.087645687646d-07*Tp**2 - 2.71639471639496d-10*Tp**3
        Else if (Tp .GT. 650.)  then
          spheat = 0.610610221283 + 1.097392587603d-03*Tp
     &         - 7.501701557086d-07*Tp**2 + 1.923219044211d-10*Tp**3
        Endif

      Else

c  Calculate the specific heat of Tin {J/(kg C)} from data in
.....Thermophysical Properties of Matter.
        If (Tp .LT. 505.03) then
         spheat = 1.1484d-03*Tp**2 - 0.56448*Tp + 293.28
        Else if (Tp .LT. 1030.) then
         spheat = -2.8443d-06*Tp**3 + 5.7824d-03*Tp**2 - 3.9539*Tp
     &           + 1148.7
        Else
         spheat = 100.
```

```
      Endif
     Endif

     Return
     End

c ***********************************************************
c ***********************************************************

     Double precision Function cond( R, Tp )

c  This function calculates the conductivity of Air{W/(m C)}, and
c  of Tin {W/(m C)}, depending on temp and phase.

     Double Precision  Tp
     Integer  R

     If (R .EQ. 1)  then

c  Calculate for Air.
      cond = 0.02624 * (Tp/300.)**.85

     Else

c  Calculate for Tin.
      If (Tp .LT. 505.03) then
       cond = -8.257d-08*Tp**3 + 1.881d-04*Tp**2 - .14505*Tp
&           + 95.436771
      Else
       cond = 3.381d-11*Tp**3 - 2.1077d-07*Tp**2 + 0.020796*Tp
&           + 19.8594
      Endif
     Endif

     Return
```

```
      End

c ***********************************************************
c ***********************************************************

      Double precision Function rho( R, Tp )

c  This subroutine calculates the temperature dependent density of the
c  material in regions 1 & 2. This subroutine must be altered when
c  different materials are used. Here region 1 is air and region 2
c  is Indium.

       Double precision  Tp
      Integer  R

       If (R .EQ. 1) then

c  Assign density of air {kg/m^3}.
        rho = 101.3/(.287*Tp)

c  Assign density of Tin {kg/m^3}. Density is now also dependent
c  on phase.
      Else
        If (Tp .LT. 505.03) then
         rho = 7280. - .51*(Tp - 298.)
         Else if (Tp .LT. 2533.) then
          rho = 7000. - .613*(Tp - 505.03)
        Else
         rho = 5757.
        Endif
       Endif

        Return
        End
```

```
c  This program integrates the deflection of a finite probe-beam.  It takes
c  the deflection data for each ray calculated from the main program, and
c  discretely integrates either for an increasing finite size beam starting at
c  the surface, or a fixed size beam moving away from the surface.

c ***************************************************************

      Integer  num
      Parameter (num=200)
      Double precision  theta(num),time,sum,ztheta(num),dzray,
     &                  radius,Kc,Kr
      Integer  i,j,k,numrays,length,k1,k2

      Open(28,file = 'insum')
      Open(30,file = 'S')
      Open(31,file = 'sum')

      Read(28,12) numrays,length,dzray,radius
      Write(6,*) 'numrays, length, dzray & radius ='
      Write(6,*)  numrays,length,dzray,radius
 11   Format(100(1pe12.5,1x))
 12   Format (2(10x,I4/),2(10x,g12.5/))
 13   Format(3(1pe12.5,','),I4)

c  Calculate the beam deflections for a probe beam of finite radius.
c....Choose top line if integrating beam starting at the surface, and
c  the next line is for changing beam size.
      Do 60  k = 1, 1
c     Do 60  k = 2, numrays

        k1 = (k-1)*Int( (numrays - 2.*radius/dzray)/20. )  + 1
        k2 = k1 + Int( radius/dzray )
        Kc = DBLE( (k1+k2) )/2.
        Kr = DBLE( (k1-k2) )/2.
        Open(29,file = 'tin',recl= 2000)
```

```
      Do 50  j = 1,length
       Read(29,11) time,(theta(i),i = 1,numrays)
       Read(30,11) time,(ztheta(i),i = 1,numrays+1)
       sum = 0.
       Do 40  i = k1, k2
c  If Gaussian fit is desired, uncomment top line and comment out
c  bottom line where the weight is one.
c         sum = sum + theta(i) * EXP( -2. * ABS( (Kc - Dble( i ))/Kr ) )
        sum = sum + theta(i)
 40     Continue
      Write(31,13) time, Dble(k1+k2)/2.*dzray, sum/Dble(k2-k1)
 50    Continue
     Write(31,*)
     Close(29)
 60   Continue

     Close(28)
     Close(30)
     Close(31)

     Stop
     End

c ***************************************************************
```

Here are representatives of the miscellaneous files used in the calculations for the main program and the finite deflection program. Included is Case, In, Insum, and the file main.h used by the C language preprocessor.

File Lists

Case

Ste = 0.431
diffuse = 0.286
SteRatio= 0.123
Rsing = 1.00

In

w(radius)=8.0e-5
Power = 4.3
tpulse = 1.0e-3
Tint = 505.03
Tamb = 505.03
Tmelt = 505.03
Tboil = 2543.1
L = 6.02784e4
aspect = 2.0
divideR = 30.0
surf = 1.0
step = 3.0
zray = 2.0
cycle = 1
outstep = 60
numrays = 80

Insum

numrays = 80
length = 100
dz0/zray= 1.4195e-02
radius* = 0.28390

main.h

```
#define Smelt  S(1)
#define Sboil S(2)
#define kAIR  km(1)
#define kLIQ  km(2)
#define alphaAIR  diff(1)
#define alphaLIQ  diff(2)
```

Appendix II
Signal Power Calculation Program

The following is a Mathematica program run on a main-frame computer to calculate the power in a time data sequence which correlates to the stress power found in chapters 4 and 5. The mathematics employed are presented in § 4.2.4. The operations in this program are on matrix and vector quantities, and the notation is standard for Mathematica *.

* Stephen Wolfram, *Mathematica A System for doing Mathematics by Computer* 2nd Ed., Addison-Wesly Publishing Co. New York (1991).

Program Listing

```
(* First set the directory to where the data files are. *)
SetDirectory["Data/Source/Dir"]
(* Read in file list for the power to be calculated. *)
files = FileNames["*data.files"]
Save["filelist",files]
(* Read in data to initial matrix and find size. *)
RawIn = Table[Flatten[Drop[Transpose[ReadList[files[[i]],
                    Number,RecordLists -> True]],1]],{i,1,Length[files]}];
num = Length[RawIn[[1]]]
```

```
(* Calculate the number of power levels used in this run *)
n = Length[files]
(* Enter in the time data of the signal *)
time = Flatten[Drop[Transpose[ReadList[files[[1]],
                                    Number,RecordLists -> True]],-1]];
(* Assemble the data with the time in pairs so that a fit can be done
   against time for each run. *)
assembled = Table[Transpose[Prepend[{RawIn[[i]]},time]],{i,n}];
(* Find the baseline offset for each run to make the data is ergodic.
   A third order polynomial is used for approximating the offset
   from the zero line to account for a low frequency oscillation.
   This information is saved in "base" so that the power contained in
   the baseline curve can be found and added in later as an
   approximate correction to the power lost by making the data
   ergodic *)
base = Table[Fit[assembled[[i]],{1,x,x^2,x^3},x],{i,n}]
Save["base",base]
Clear[assembled]
(* Calculate the time step between discrete data points. *)
dTime = time[[2]] - time[[1]]
(* Create a matrix of discrete values for the baseline curve. *)
TabBase = {};
Do[Block[{c},
  c = Table[base[[i]],{x,First[time],Last[time],dTime}];
AppendTo[TabBase,c]],{i,n}];
(* Subtract off the baseline to make data ergodic. *)
ergodic = Table[RawIn[[i]] - TabBase[[i]],{i,n}];
(* Find the power in the ergodic signal before discrete integration.
```

```
   Take the FFT for each signal.  Auto-correlate for the raw power. *)
ergpower = Table[Partition[Abs[Fourier[ergodic[[i]]]]^2,1],{i,n}];
(* Find the time period of a sampled data and the corresponding
   frequencies up to the Nyquist limit. *)
Period = Last[time] - First[time];
freq = Table[ i/(2 Period), {i,0,num - 1}];
(* Create the symmetric frequency vector corresponding to the
   symmetric Fourier transform. *)
freqSym = Flatten[Prepend[Take[freq,{2,num/2}],
                                        Sort[-Take[freq,num/2]]]];
(* Discretely integrate in the frequency domain. *)
totalErg = Table[Sum[Abs[freqSym[[j]]] ergpower[[i,j]],{j,1,num}],{i,n}];
(* Integrate in time to find the power in the baseline curve. *)
totalBase =
      Table[NIntegrate[D[base[[i]]^2],{x,First[time],Last[time]}],{i,n}];
(* Add sum of integrals  to get estimate of total power. *)
total = totalErg + totalBase;
(* Save the data  power vector. *)
Save["filename",total]
Quit[]
```